2020

Carbon Oxidation at the Atomic Level: A Computational Study on Oxidative Graphene Etching and Pitting of Graphitic Carbon Surfaces

Simon Schmitt

University of Kentucky, schmitt.simon94@gmail.com
Author ORCID Identifier:
 https://orcid.org/0000-0002-9447-3591
Digital Object Identifier: https://doi.org/10.13023/etd.2020.450

STUDENT AGREEMENT:

I represent that my thesis or dissertation and abstract are my original work. Proper attribution has been given to all outside sources. I understand that I am solely responsible for obtaining any needed copyright permissions. I have obtained needed written permission statement(s) from the owner(s) of each third-party copyrighted matter to be included in my work, allowing electronic distribution (if such use is not permitted by the fair use doctrine) which will be submitted to UKnowledge as Additional File.

I hereby grant to The University of Kentucky and its agents the irrevocable, non-exclusive, and royalty-free license to archive and make accessible my work in whole or in part in all forms of media, now or hereafter known. I agree that the document mentioned above may be made available immediately for worldwide access unless an embargo applies.

I retain all other ownership rights to the copyright of my work. I also retain the right to use in future works (such as articles or books) all or part of my work. I understand that I am free to register the copyright to my work.

REVIEW, APPROVAL AND ACCEPTANCE

The document mentioned above has been reviewed and accepted by the student's advisor, on behalf of the advisory committee, and by the Director of Graduate Studies (DGS), on behalf of the program; we verify that this is the final, approved version of the student's thesis including all changes required by the advisory committee. The undersigned agree to abide by the statements above.

<div align="right">

Simon Schmitt, Student

Dr. José Graña-Otero, Major Professor

Dr. Alexandre Martin, Director of Graduate Studies

</div>

CARBON OXIDATION AT THE ATOMIC LEVEL: A COMPUTATIONAL
STUDY ON OXIDATIVE GRAPHENE ETCHING AND PITTING OF
GRAPHITIC CARBON SURFACES

——————————————

DISSERTATION

——————————————

A dissertation submitted in partial
fulfillment of the requirements for
the degree of Doctor of Philosophy
in the College of Engineering at the
University of Kentucky

By
Simon Schmitt
Lexington, Kentucky

Co-Directors: Dr. José Graña-Otero, Assistant Professor of Mechanical
                Engineering
and   Dr. Michael Renfro, Professor of Mechanical Engineering

Lexington, Kentucky

2020

ABSTRACT OF DISSERTATION

CARBON OXIDATION AT THE ATOMIC LEVEL: A COMPUTATIONAL
STUDY ON OXIDATIVE GRAPHENE ETCHING AND PITTING OF
GRAPHITIC CARBON SURFACES

In order to understand the oxidation of solid carbon materials by oxygen-containing gases, carbon oxidation has to be studied on the atomic level where the surface reactions occur. Graphene and graphite are etched by oxygen to form characteristic pits that are scattered across the material surface, and pitting in turn leads to microstructural changes that determine the macroscopic oxidation behavior. While this is a well-documented phenomenon, it is heretofore poorly understood due to the notorious difficulty of experiments and a lack of comprehensive computational studies. The main objective of the present work is the development of a computational framework from first principles to study carbon oxidation at the atomic level.

First, the large body of literature on carbon oxidation is examined with regards to experimental observations of the pitting phenomenon as well as relevant theoretical studies on different aspects of the mechanistic details of carbon oxidation. Next, a comprehensive, atomic-scale kinetic mechanism for carbon oxidation is developed, which comprises only elementary surface reactions with reaction rates derived from first principles. The mechanism is then implemented using the Kinetic Monte Carlo (KMC) method. This framework for the first time allows the simulation of oxidative graphene etching at the atomic scale to relevant time- and lengthscales (up to seconds and hundreds of nanometers), and in a wide range of conditions (temperatures up to 2000 Kelvin, pressures ranging from vacuum to atmospheric pressure).

The numerical results reveal information about the pitting process in heretofore unattained detail: Pit growth rates (and therefore intrinsic oxidation rates) are calculated and validated against a set of different experimental data at a wide range of conditions. Such information is crucial for modelling of material behavior on meso- and macroscales. The dependence of the pit geometry (hexagonal vs. circular) on temperature and gas pressure is assessed. This is important for utilizing oxidative etching as a manufacturing technique for graphene-based nanodevices. More subtle phenomena like pit inhibition at low pressures and temperatures are also discussed. Moreover, all these findings are examined with respect to the underlying reaction mechanism. This unveils the fundamental reasons for the observed reaction behav-

ior, in particular different activation energies and reaction orders at low and high temperatures, as well as the transition of the pit geometry.

The present work is a first step in an ongoing effort to develop predictive models for carbon oxidation in Thermal Protection Systems (TPS), with the ultimate goal of improved safety for hypersonic flight vehicles.

KEYWORDS: carbon, graphene, oxidation, etching, pitting, kinetic monte carlo

Author's signature:_____Simon Schmitt_____

Date:_____November 26, 2020_____

CARBON OXIDATION AT THE ATOMIC LEVEL: A COMPUTATIONAL
STUDY ON OXIDATIVE GRAPHENE ETCHING AND PITTING OF
GRAPHITIC CARBON SURFACES

By
Simon Schmitt

Co-Director of Dissertation: José Graña-Otero

Co-Director of Dissertation: Michael Renfro

Director of Graduate Studies: Alexandre Martin

Date: November 26, 2020

ACKNOWLEDGMENTS

First and foremost, I would like to express my deepest gratitude to my supervisor Dr. José Graña-Otero, who saw potential in me when I first came to the University of Kentucky as an undergraduate research intern from Germany, and convinced me to pursue my graduate studies under his guidance. He has introduced me into the fascinating world of combustion science, from which ultimately this doctoral work arose. His natural instinct to ask the most fundamental and challenging research questions and relentless effort to answer them has been and continues to be a great inspiration. I would not be typing this document without his generous help and financial support.

I would like to sincerely thank Dr. Michael Renfro and Dr. Alexandre Martin for their guidance and support throughout my time at UK, and in particular during the last year. Thanks also to my remaining committee member Dr. Chad Risko for lending me his time and expertise.

I want to express gratitude to all my coworkers and fellow graduate students that I had the pleasure to work, learn and study with during this journey. Special thanks to Siamak Mahmoudi, whose friendship has made the time in the lab much more enjoyable.

Finally, it is time for me to express profound appreciation to my parents and siblings. Your unconditional love, support and care kept me going throughout the years, and I am forever indebted to you for that.

TABLE OF CONTENTS

<h1>LIST OF TABLES</h1>

LIST OF FIGURES

LIST OF ADDITIONAL FILES

KMC Simulation Files: Zacros KMC simulation files for example simulation at temperature $T = 1000\,\mathrm{K}$ and pressure $P = 1\,\mathrm{mbar}$:

– Zacros energetics input file (filename: energetics_input.dat, filesize: 327 Bytes),

– Zacros lattice input file (filename: lattice_input.dat, filesize: 1 KB),

– Zacros mechanism input file (filename: mechanism_input.dat, filesize: 31 KB),

– Zacros simulation input file (filename: simulation_input.dat, filesize: 1 KB),

– Zacros state input file (filename: state_input.dat, filesize: 355 Bytes).

Note: These KMC simulation files are best viewed in a standard text editor software.

Video Files:

– Supporting Video SV1: Video of simulated etch pit at temperature $T = 1000\,\mathrm{K}$ and pressure $P = 1\,\mathrm{mbar}$ (filename: sv1.mp4, filesize: 25 MB),

– Supporting Video SV2: Video of simulated etch pit at temperature $T = 850\,\mathrm{K}$ and pressure $P = 0.01\,\mathrm{mbar}$ (filename: sv2.mp4, filesize: 23 MB),

– Supporting Video SV3: Video of simulated etch pit at temperature $T = 1500\,\mathrm{K}$ and pressure $P = 100\,\mathrm{mbar}$ (filename: sv3.mp4, filesize: 26 MB).

Chapter 1 Introduction

1.1 Motivation

One of the great challenges in hypersonic flight is the protection of air- and space-craft against extreme aerodynamic heating [1]. The surface of such flight vehicles is typically equipped with a heat shield, which is referred to as a thermal protection system (TPS). Its goal is to keep the structure of the vehicle intact and its payload safe. Many TPS use carbon as the base material due to its favorable material properties. At flight speeds much larger than the speed of sound, a compressive shock wave forms in front of the vehicle, leading to high gas temperatures and ionization of gas molecules into more reactive atoms, in particular oxygen. This gas impinges on the TPS, oxidizes the carbon, and thereby gradually burns off the heat shield. This burnoff process is one of the main contributors to the ablation phenomenon.

There are various different ablative carbon heat shields in use today, and they can be broadly divided into two classes: surface and charring ablators [2]. Examples for surface ablators are carbon-carbon (C/C) and carbon-fiber-reinforced silicon carbide (C/SiC) composite materials. A prominent charring ablator is PICA (Phenolic Impregnated Carbon Ablator), which consists of a three dimensional matrix of carbon fibers that is impregnated with phenolic resin. Figure 1.1 gives an overview of the length scales at which ablation takes place in PICA, ranging from the vehicle size all the way down to the atomic level. The physical and chemical processes in both the gas phase and the actual solid TPS material on all these length scales are coupled, making ablation a complex multiscale problem.

In the practical design of TPS, one needs to predict how fast the TPS is receding under flight conditions. While this recession rate differs between different types of carbon ablators, carbon oxidation at the atomic scale on the material surface plays
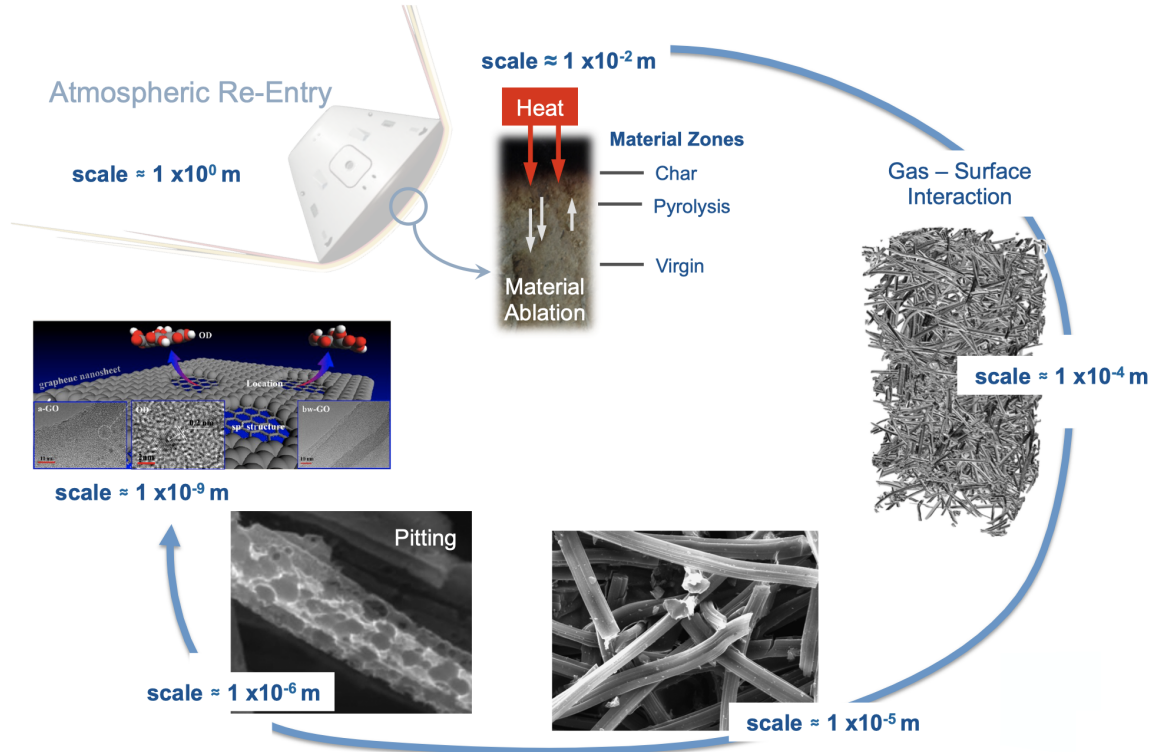
Figure 1.1: The multiple scales of oxidation of a porous TPS (PICA). Fiber SEM micrographs from [3], reprinted by permission of the American Institute of Aeronautics and Astronautics, Inc.; fiber matrix micro-CT rendering reprinted from [4], Copyright (2017), with permission from Elsevier; atomic-scale rendering reprinted with permission from [5], Copyright 2016, American Chemical Society.

a fundamental role, as pictured in Figure 1.1. At that level, the surface consists of graphene- and graphite-like structures, regardless of the type of carbon ablator. However, oxidation on such a surface does not proceed uniformly. In fact, one typically observes localized growth of cavities on the surface and into the bulk carbon material at the nano- to micrometer level. This phenomenon is called pitting. Pitting locally increases the oxidation rate by increasing the surface area and the reactivity per unit surface area, which ultimately affects the recession rate. Although it is well known that pitting is the characteristic mode through which graphitic carbon surfaces oxidize, current ablation models do not account for it directly [6]. Therefore, to overcome this limitation in ablation models and thereby improve their predictive capabilities, the carbon oxidation process and pitting in particular need to be
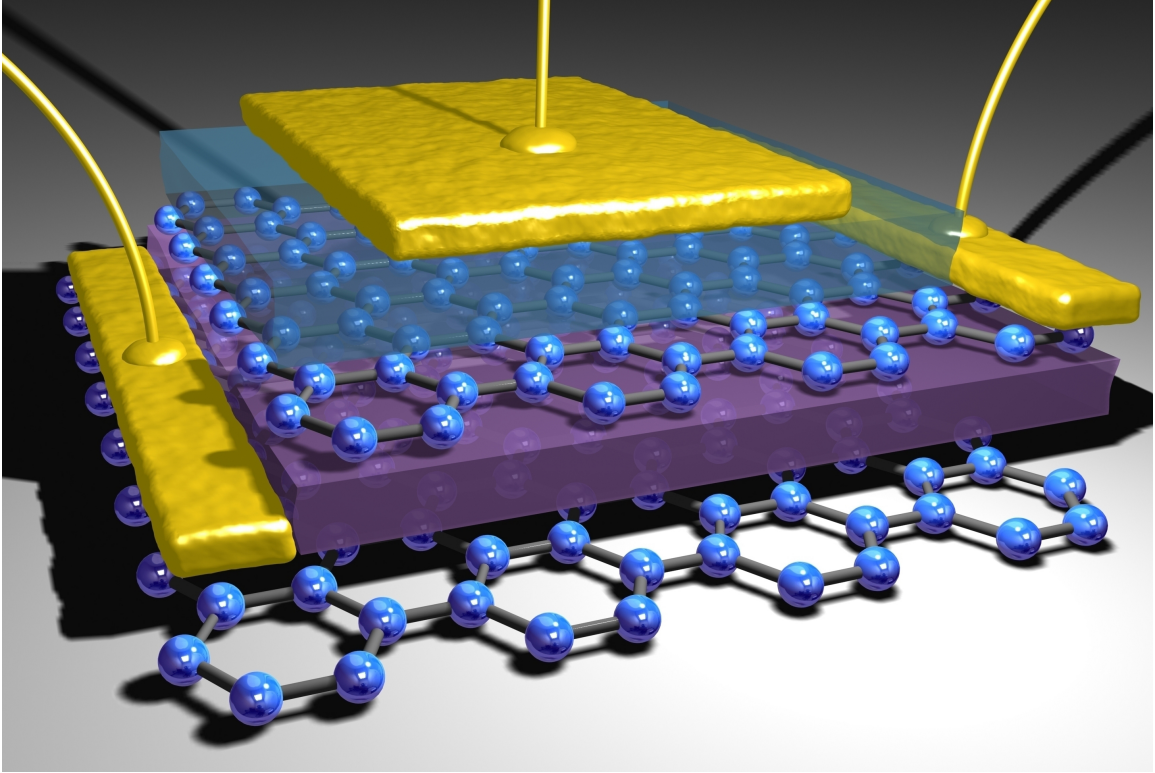
Figure 1.2: Artistic rendering of tunneling transistor based on graphene nanoribbons. Reprinted with permission from [7].

understood fundamentally at the atomic level.

Moreover, ever since its famed discovery in 2004 [8], graphene has been considered to potentially revolutionize electronic nanodevices due to its magnificent material properties [9, 10]. For instance, graphene has been utilized experimentally in laboratory environments in the form of nanoporous graphene membranes for water desalination [11] and DNA sequencing [12, 13], as well as in the form of graphene nanoribbons (GNR) with open bandgaps that can be utilized as transistors [14, 15]. The function of such devices depends critically on the material structure at the atomic level. For example, the electric conductivity of GNR is controlled by the structure of graphene edges, where roughness or irregularity reduces the conductivity and therefore diminishes the desired function [16]. Hence, there is a need for manufacturing techniques that produce atomically smooth edges, for instance as pictured in Fig-

ure 1.2. A promising technique that allows control over the edge structure at the atomic level is etching of graphene through oxidation in a gaseous environment at elevated temperatures [17]. However, the dynamics of oxidative graphene etching and its dependence on the reaction conditions are not well understood. For example, the resulting graphene edge structure can be both atomically smooth or rough based on temperature and pressure, which culminates in either hexagonal or circular etch figures [18, 19]. Again, a fundamental understanding of carbon oxidation at the atomic level is required in order to make reliable predictions that can boost the efficacy of this manufacturing technique.

1.2 Research Structure and Objectives

The present work seeks to contribute to the fundamental understanding of carbon oxidation at the atomic level in conditions relevant to the previously described applications through a first-principle based, comprehensive computational study with full atomic resolution, both spatial and temporal. For that purpose, Chapter 2 assesses the existing body of literature on carbon materials and their oxidation behavior. This is done to show that the oxidation of graphitic carbon surfaces and pitting can be understood from the basis of oxidative etching of a single graphene sheet. A review of the experimental and computational work in that respect develops a qualitative image of the phenomenology, and points out the need for a comprehensive computational study that this research provides. Based on this background knowledge, Chapter 3 first formulates in detail the problem setup, namely the oxidation of single-layer graphene with monovacancy defects in oxygen gas at thermodynamic equilibrium. Following this, the selection of the appropriate computational methods with respect to accuracy and feasibility is discussed. Specifically, this study uses the Kinetic Monte Carlo (KMC) method in conjunction with a kinetic reaction mechanism developed from first-principles. The rates of all reactions included in this novel

mechanism are calculated on the basis of Transition State Theory (TST), with parameters derived from quantum chemistry using Density Functional Theory (DFT). A particular focus is given to the underlying assumptions, both in the selection of the problem setup and the computational methods, with respect to accuracy, applicability and limitations of the present study. The first major contribution of this research, namely the development of a comprehensive atomic-scale kinetic reaction mechanism for carbon oxidation from first principles, is described in Chapter 4. Next, Chapter 5 discusses the implementation of the problem setup and kinetic reaction mechanism in the readily available KMC simulation code Zacros. Furthermore, the statistical nature of KMC simulation results is examined to justify the statistical analysis approach taken in this work. The simulation results are finally presented in Chapter 6. First, to demonstrate the capabilities that this novel comprehensive computational approach delivers, a complete analysis of a single representative simulation is performed. Next, all details about graphene etching and pitting across the whole range of simulated conditions are presented, validated, and discussed with respect to the underlying kinetic reaction mechanism. This is the second major contribution of this research, since experiments are limited to provide measurable metrics like the pit growth rate, and previous computational studies have not been able to deliver comprehensive results. Lastly, Chapter 7 concludes the outcome and added value of this research, and outlines future directions in which this work may be extended, in particular with respect to predictive modelling of carbon oxidation in TPS.

Chapter 2 Background

The purpose of this chapter is to provide a knowledge base on carbon oxidation in the context of pitting and etching of graphite/graphene, and in particular to assess the work that has been performed on the fundamental understanding of this process. This requires an introductory discussion in Section 2.1 of the material structure of graphitic carbon materials, and the possible defects that are essential for understanding their oxidation behavior. After that, the carbon oxidation process itself is assessed in Section 2.2.

2.1   Carbon Material Structure

Solid carbon materials occur in an almost unimaginable number of different forms, both naturally and synthetically, and new forms are regularly discovered and developed to this day [20]. This development is largely driven today from the perspective of graphene based nanomaterials on the one hand, and carbon fibers and their composites on the other hand [21]. In fact, there exist entire journals and conferences dedicated purely to communicate original research on carbon materials.

In an introductory discussion of the material structure of solid carbon, one typically begins by examining the crystal structures of the two most prominent allotropes: diamond and graphite. For reference, the crystal structure of diamond is called diamond cubic, and its carbon atoms are arranged in tetrahedrons such that each atom bonds with four neighboring atoms. The resulting chemical bonds are sp^3 hybridized, which lends diamond its outstanding hardness among other things. However, this work is concerned with carbon oxidation of graphene and graphitic carbon materials, so instead this section focuses on the graphite allotrope.
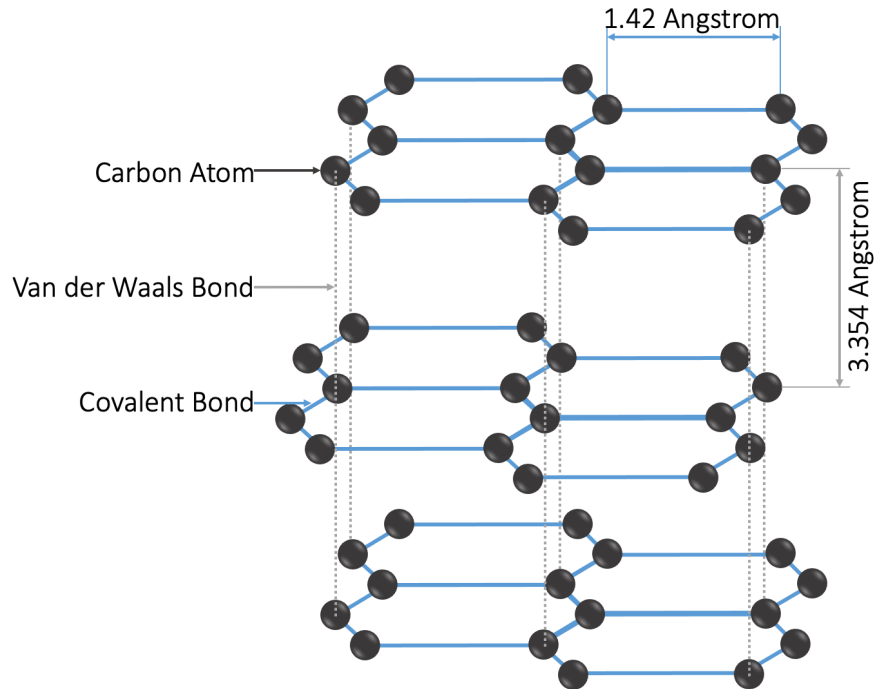
Figure 2.1: Material structure of graphite. The crystal is made up of individual layers of graphene, which are sheets of carbon atoms in a hexagonal arrangement.

2.1.1 Ideal Graphite Structure

Already in the year 1916, using powder diffraction, Debye and Scherrer [22] were able to identify the crystal structure of graphite, which is displayed in Figure 2.1. Graphite is composed of distinct layers of carbon in an hexagonal arrangement. A single of those layers is referred to as graphene. The distinct graphene layers are held together in a graphite crystal through Van der Waals forces. The interlayer distance at which the attractive Van der Waals forces balance out with electrostatic repulsion is around $3.354\,\text{Å}$ at standard conditions.

Graphene itself is a sheet of hexagonally arranged (honeycomb) carbon atoms that each have three neighboring atoms. These form strong covalent bonds with sp^2 hybridization. The average bond length of carbon atoms in graphene is around $1.42\,\text{Å}$, considerably shorter than the interlayer distance in graphite. Since the covalent bonds in each graphene sheet are much stronger than the Van der Waals forces acting between the sheets, graphite can sometimes behave as a stack of independent two-

dimensional graphene layers. One instance for such behavior is the oxidation of the graphite surface in oxygen gas, as it is examined in this work.

Both graphite and graphene have remarkable material properties due to their unique crystal structure. Theoretically, graphene is the material of superlatives, often regarded as the world's strongest and most conductive material [10]. Besides, graphite principally has very strong thermal and chemical resistance [23]. However, these attributes only directly apply to the ideal materials. In reality, structural defects can dictate the actual material properties to a large degree, and therefore require further discussion.

2.1.2   Structural Defects and Graphene Edge Structure

In a graphite crystal, defects can exist within a single sheet of graphene as well as across neighboring layers [24, 25]. Figure 2.2 provides an overview of some common defects, categorized by their topology [26]. Point defects are essentially zero-dimensional, since they only occur at a single point in the structure. Of particular importance for the present study are vacancy defects, since they act as the seeds for oxidation on the carbon surface. Furthermore, certain adatoms or impurities can act as catalysts for chemical reactions such as oxidation. Within a graphene sheet, there can be line defects such as grain boundaries, which are considered one-dimensional. Lastly, two-dimensional interlayer defects occur between neighboring graphene sheets. Sheets can be rotated relative to each other, causing stacking faults present in so-called turbostratic carbons, and single atoms can be trapped in between layers and create interstitial defects.

In the context of carbon oxidation, vacancy defects are among the most important types of defects. The removal of distinct carbon atoms from an otherwise pristine graphene sheet leaves behind carbon atoms with a smaller number of bonds that hold them in place, which in turn makes those atoms more susceptible to oxidation, as
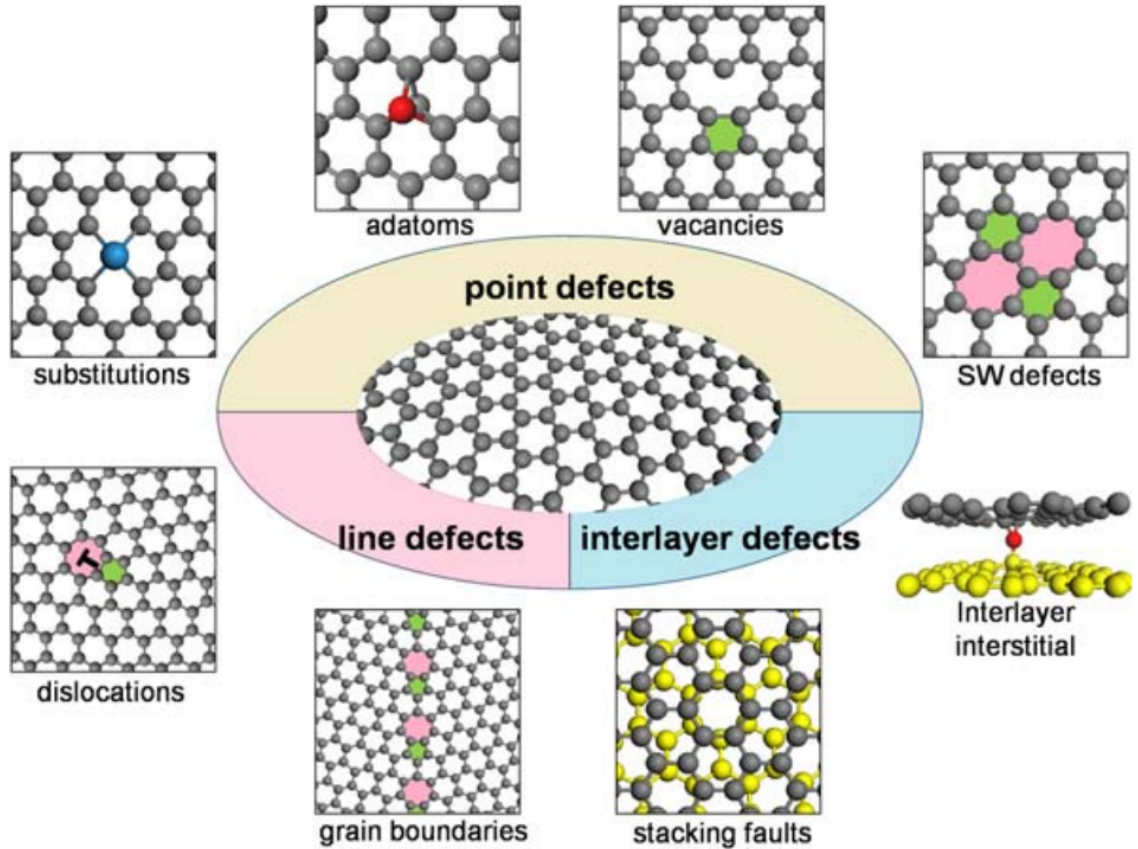
Figure 2.2: Common types of defects in graphite/graphene, characterized by their topology. Reprinted from [26], Copyright (2018), with permission from Elsevier.

will be seen later. Those carbon atoms are referred to as edge carbon atoms, and if they form extended lines, those line defects are simply referred to as a carbon edges.

It is useful to categorize the types of edges that exist in graphene. Figure 2.3 shows the most commonly used categorizations [27]. The most common types of carbon edges are armchair and zigzag edges. In armchair edges, there occur pairs of two (or more) edge carbon atoms, whereas zigzag edges are composed of a sequence of single carbon edge atoms. Both types of carbon edges align with the principal crystallographic directions in a graphene sheet. All other types of edges shown in Figure 2.3 are less frequently used, since they can also be regarded as compositions of zigzag and armchair edge sites. Hence, only armchair and zigzag are directly considered for this study.
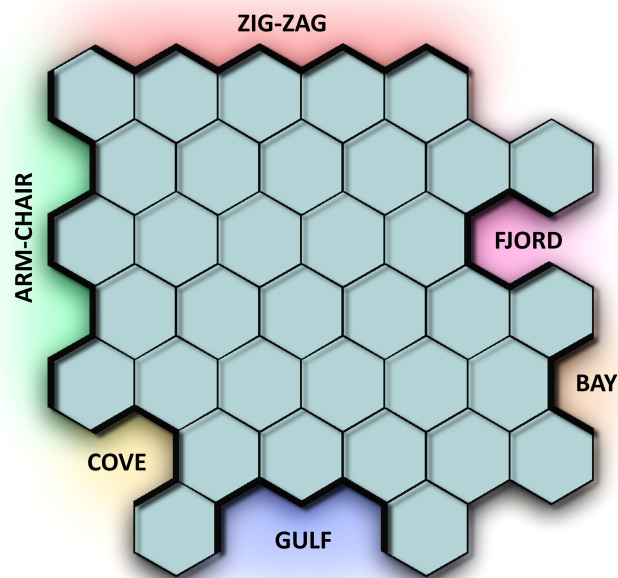
Figure 2.3: Graphene edge structure. The zigzag and armchair edges are of particular importance for carbon oxidation. Reproduced from [27] (adapted from [28]).

As it turns out, the number of carbon edge sites and their distribution along the carbon surface are critical for the oxidation behavior of real materials. That in turn depends on the exact structural composition at the mesoscopic level (tens on nanometers up to millimeters) of the carbon material. Therefore, while this is not going to be subject later in this study, it is still instructive to discuss the composition of realistic graphitic carbon materials at this point.

2.1.3 Real Graphitic Carbon Materials

The microstructure of carbon materials has been unraveled in the 1940's and 1950's to a great extent by the pioneering x-ray diffraction work of Franklin [29]. Today it is well understood that carbon materials are composed of crystals of graphite of different quality and orientation, connected by more or less amorphous regions of carbon. This leads to the distinction between non-graphitizing and graphitizing carbon, as shown in Figure 2.4. Graphitizing carbons tend to be composed of larger
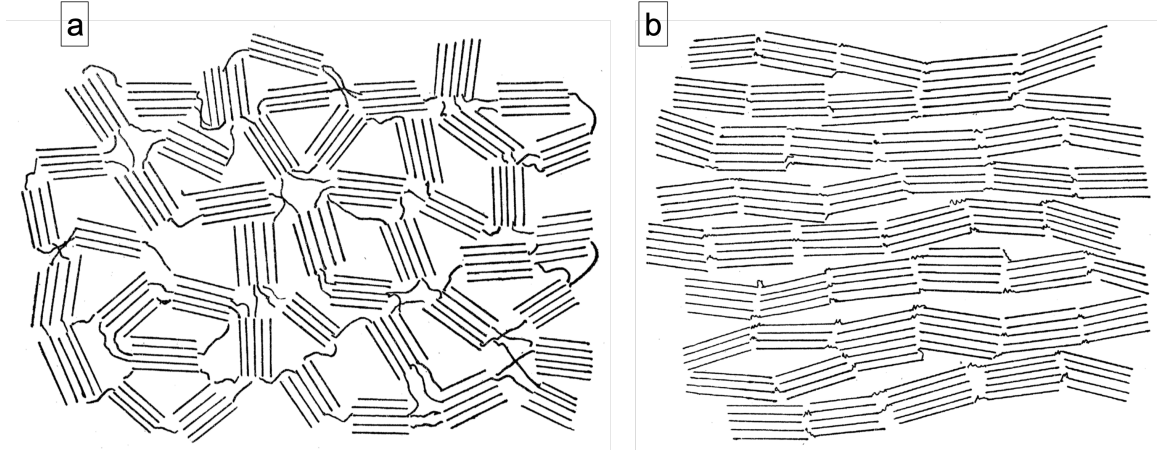
Figure 2.4: Schematic representations of (a) non-graphitizing and (b) graphitizing carbon. Republished with permission of Royal Society of London, from [29], Copyright (1951), permission conveyed through Copyright Clearance Center, Inc.

individual graphite crystals as compared to non graphitizing, and they have at least some degree of alignment relative to each other. In contrast, the graphite crystals in non-graphitizing carbons are mostly disordered. The actual term graphitizing comes from the process of graphitization, where graphite is annealed at high temperatures to reduce the number of structural defects by further aligning the distinct graphite crystals. There are modern models, especially for non-graphitizing carbon, taking into account more complicated "building blocks" such as fullerene-like structures (see e.g. [30] for a review). However the general idea remains the same: Graphitic carbon materials are composed of graphite crystals at nanometer length scales.

A material of great technological value are carbon fibers [24]. Figure 2.5 shows a structural model for a typical PAN-derived carbon fiber [31]. In the core of the fiber, there tends to be a lot of disorder with small graphitic areas, similar to non-graphitizing carbon. In contrast, on the outside surface of the fiber, large graphite layers are present that are furthermore oriented such that the carbon basal plane is facing outward of the fiber. In other words, the carbon fiber tends to be a graphitizing carbon on the outside. This must obviously have a large effect on its properties. For example, the thermal strength of carbon fibers can be explained from the basis of their
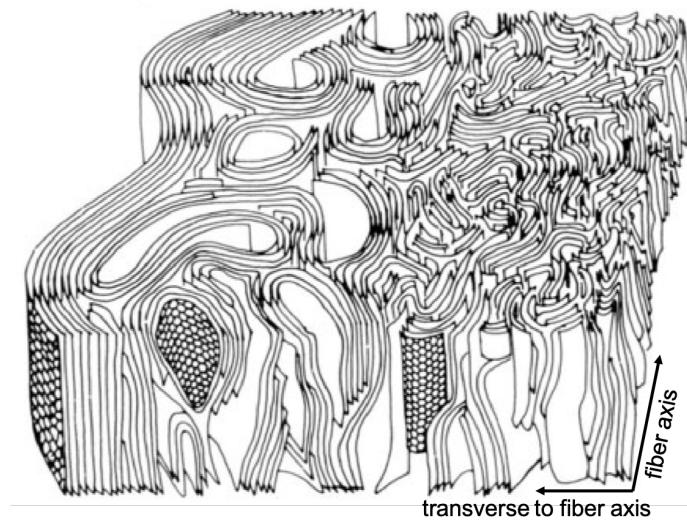
Figure 2.5: Carbon fiber structural model for a typical PAN-derived fiber. Republished with permission of IOP Publishing, from [31], Copyright (1987), permission conveyed through Copyright Clearance Center, Inc..

microstructure [24], which is particularly helpful in hypersonic related applications.

This is just a single example of a structural model for a particular carbon fiber, and many more such models for various types of carbon materials exist. However, it stresses two important ideas: First, all graphitic carbon materials are composed of nanoscopic or microscopic sized graphite crystals. Second, the composition of the bulk material from those small crystals is ultimately determining the material behavior. While this study only focuses on understanding carbon oxidation on a fundamental level, i.e. a single sheet of graphene and therefore an isolated graphite crystal, it is nevertheless important to appreciate these ideas when moving forward into building meso- and macroscopic models on carbon oxidation from first principles in the future.

2.2 Carbon Oxidation

The oxidation of solid carbon materials through gas-surface reactions has been studied for a long time since it is ubiquitous in modern technological applications [32–34]. In coal power generation, carbon is used directly as a fuel to generate energy through

12

combustion. In nuclear power reactors, neutrons can be moderated by graphite. An important safety concern is the scenario when the graphite moderator gets exposed to air as a result of a reactor leak, which can ultimately result in degradation of the graphite moderator through oxidation and subsequent release of radiation among other things [35]. As discussed in the introduction, carbon is also used as a base material for ablative thermal protection systems. What these and many other applications have in common is that a solid carbon material of some sort interacts with an oxygenic gas environment at high temperatures, which results in oxidation on the material surface.

From a practical standpoint, carbon oxidation is usually studied on a phenomenological basis. Due to the structural complexity of carbon materials, models have to rely on empirical parameters and relations which are specific to the carbon material and/or the conditions under which oxidation is performed. Such empirical data is often deduced from experiments via global analysis methods, for instance using gravimetric analysis [32]. Somewhat more meaningful structural parameters such as active surface area [36] are often included in those models, but then the evolution of those parameters itself with proceeding oxidation is described empirically.

On the other hand, from the fundamental perspective that this study is taking, carbon oxidation can be understood universally from first principles on the basis of oxidation of a sheet of graphene. The phenomenon that is always observed on the surface of oxidizing carbon materials is pitting [37], as introduced already in Chapter 1. In fact, pitting is the characteristic surface consumption mode on the atomic scale, and it has been observed experimentally not only in carbon oxidation [3, 18, 38–43], but also in corrosion of other materials like aluminum [44–47].

It is well known that the oxidation on the atomic level occurs at so-called active carbon sites on the material surface, where carbon atoms are missing neighboring atoms compared to atoms in the bulk of the surface graphene sheet [48, 49]. These

are exactly the edge carbon atoms that are discussed above, which exist at structural defects in the carbon material. Knowing the number and distribution of those active sites in principal allows to predict the oxidation rate of the material, provided the transport of oxygen towards those active sites is known. This is where carbon oxidation is coupled to the material structure, and this holds the key for scaling up from pitting on the micro- and nanoscale to macroscopic reaction behavior.

Pitting itself is the result of elementary surface processes on the graphene sheet constituting the material surface, namely oxygen adsorption and dissociation, surface diffusion, surface reactions and desorption of reaction products or other species. Understanding all these reactions in detail is a crucial part of this work and is the main subject of Chapter 4. One particular point to notice already is that oxidation of armchair and zigzag edge carbons have different reaction rates. This can lead to interesting behavior such as hexagonal pits with sides being purely zigzag edges, as was heuristically explained by Hughes, Williams, and Thomas [50].

Etch pits originate in point defects such as monovacancies. From there they start to grow in size as oxidation proceeds. Since defects are mostly distributed randomly across the material surface, distinct etch pits tend to be scattered randomly across the surface.

On this basis, pitting experiments can now be interpreted.

2.2.1 Experimental Studies

As it turns out, pitting holds the key for experimentally studying carbon oxidation on a fundamental level. Brunner and Hammerschmid [51] were the first to observe "Brandfiguren" (etch pits) in the year 1926 when they examined the remnants of burned graphite under an optical microscope. Interestingly, they were already making the link to the graphite structure as the underlying cause for this phenomenon. Figure 2.6 a) shows a photomicrograph of the observed etch pit of an observed Brand-

figur. Later in 1962, Hennig [52] also observed etch pits on oxidized graphite under an optical microscope, see Figure 2.6 b). In both cases, natural graphite crystals (from Ticonderoga (NY) and Madagascar) were used as the studied material. In order to remove as much as possible impurities and defects before oxidation, Hennig [52] applied a purification procedure which has more or less become the standard procedure, namely repeated washing of the sample in acid and annealing at high temperatures. This is extremely important to ensure that the pits actually result from the carbon oxidation reactions and are not caused for instance by catalyzed reactions through impurities [52, 53]. As a result, the observed pits can be expected to stem from actual graphite defects. The actual oxidation is carried out subsequently in a heated furnace oven, with a controlled level of oxygen gas. The diameters of the observed pits in those early experiments are on the order of tens of micrometers, and the pits clearly have a hexagonal shape. Notice that in both cases, the hexagons are terracing down into the bulk of the graphite crystal. This can be linked to the kind of defect on which pitting is initiated here, namely screw dislocations that protrude into the graphite crystal. In most early studies with optical microscopes, only pitting from screw dislocations is observable, because significant pit depth is required for contrast [54, 55]. Interestingly, notice that in Figure 2.6 a), the upper most layers are rotated relative to the lower layers, which indicates the presence of a stacking fault defect in the graphite crystal. While those early studies do not deliver useful quantitative data on the dynamics of pit growth and therefore the oxidation reaction, they were used heavily to understand and experimentally validate the existence of certain structural defects in graphite [56, 57].

A few years later, it was again Hennig [48] who introduced the so called gold decoration method into the study of the oxidation of graphite. After oxidation of the graphite sample, following the same sample preparation procedure as previously, gold atoms were condensed onto the carbon surface, which are able to diffuse across
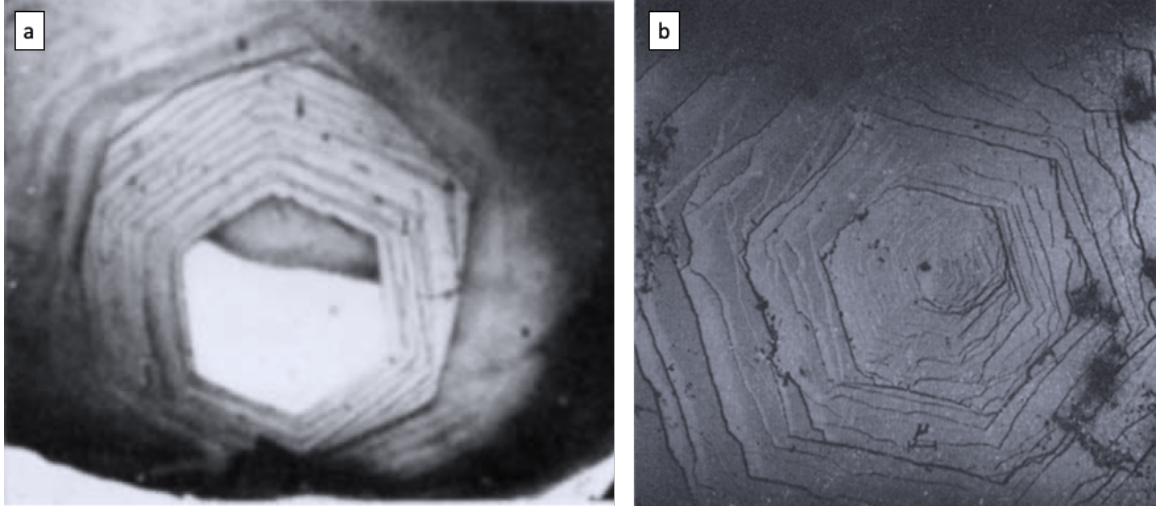
Figure 2.6: Early experimental observation of etch pits in graphite, captured with optical microscopy. (a) reprinted from [51] with permission from John Wiley & Sons; (b) reprinted from [52], Copyright (1962), with permission from Elsevier.

the basal plane surface and eventually stick to the carbon edges in the surface layers were the pits have grown. This conceptually simple idea allowed researchers to study the oxidation of just a few or even a single graphene layer on the surface of graphite crystals, since the pits are clearly visible under the transition electron microscope (TEM). Figure 2.7 shows two graphite surfaces where the etch pits have been decorated with gold. Observable pit sizes with this technique are smaller, on the order of micrometers. In contrast to the earlier studies, it can be said with certainty that these are pits that started to grow from vacancy defects in the surface layer of the graphite crystal. Interestingly, both circular (Figure 2.7 (a)) and hexagonal (Figure 2.7 (b)) pits have been observed that way.

Yet newer inventions on microscopic imaging eventually made the gold decoration technique unnecessary, namely the scanning electron microscope (SEM) and scanning tunneling microscope (STM). Figure 2.8 show etch pits recorded with SEM and STM respectively. In Figure 2.8 (a), the pits are on the order of a hundred nanometers in size, while Figure 2.8 (b) resolves down to just a few nanometers. Furthermore, SEM allows to measure the depth of the pits, which delivered the first experimental
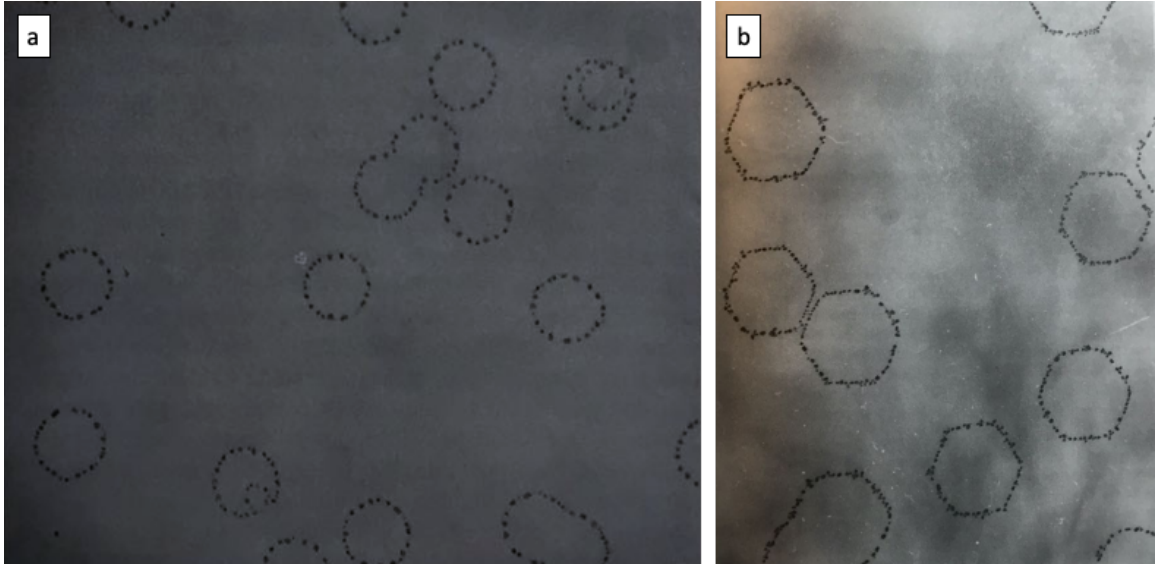
Figure 2.7: Gold decorated etch pits visualized by transition electron microscopy. Republished with permission of Taylor & Francis Group LLC, from [48] (a) and [58] (b), permission conveyed through Copyright Clearance Center, Inc..

confirmations that observed etch pits truly are growing only in the single outside graphene layer of the graphite crystal. In Figure 2.8 (a), it can be seen that pits start to grow on the outer most layer, which uncovers the second layer which itself has vacancy defects that eventually cause a pit to grow on that layer. This continues indefinitely through the graphite crystal. Figure 2.8 (b) is remarkable since it clearly shows from the alignment of the pit with respect to the graphite lattice vectors (see Figure inset), that the edges that comprise the pit circumference are zigzag edges.

It is furthermore now possible to observe the growth of pits in-situ with the use of environmental SEM at low pressures. While the constant exposure to the electron beam actually affects the oxidation rate, these studies give completely new details about the dynamics of pitting. Thomsen et al. [18] have studied the oxidation of a single suspended graphene sheet, and provide videos in their supplementary material. Figure 2.9 shows the transition of hexagonal pits to circular shape with somewhat irregular or rough edges. Lastly, Figure 2.10 shows yet another transition of the pit geometry, where pits become circular with increasing temperature.
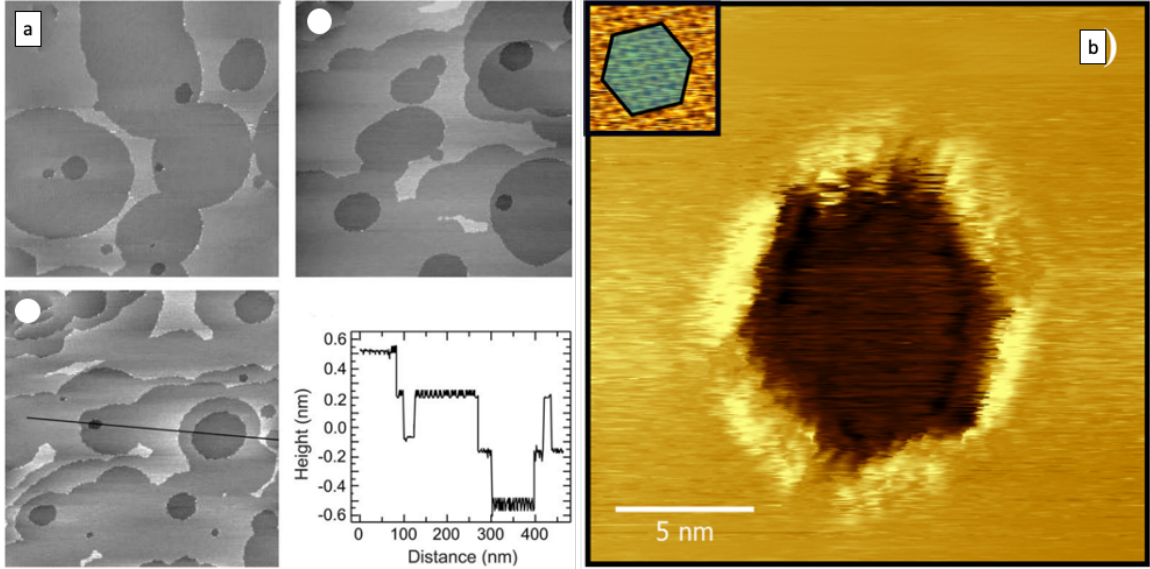
Figure 2.8: Etch pits observed with Scanning Electron Microscope (SEM) and Scanning Tunneling Microscope (STM). (a) reprinted from [43], Copyright (2005), with permission from Elsevier. (b) reprinted with permission from [59], Copyright 2018, American Chemical Society.
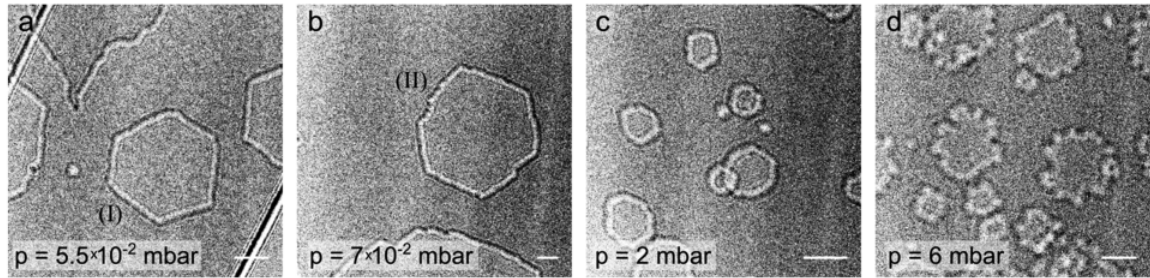
Figure 2.9: Pit geometry transition with pressure, from hexagonal (low P) to circular (high P). Reprinted with permission from [18], Copyright 2019, American Chemical Society.

From a dynamic perspective, pit radius growth rates measured in experiments have always been found to be constant in time. However, direct proof in form of a highly resolved signal in time was possible only through the recent introduction of in-situ methods [18]. It is interesting to notice that Hahn et al. [60] realized another dynamic behavior, namely the inhibition of pit growth early during oxidation when pits are small and are just starting out to grow from vacancy defects.
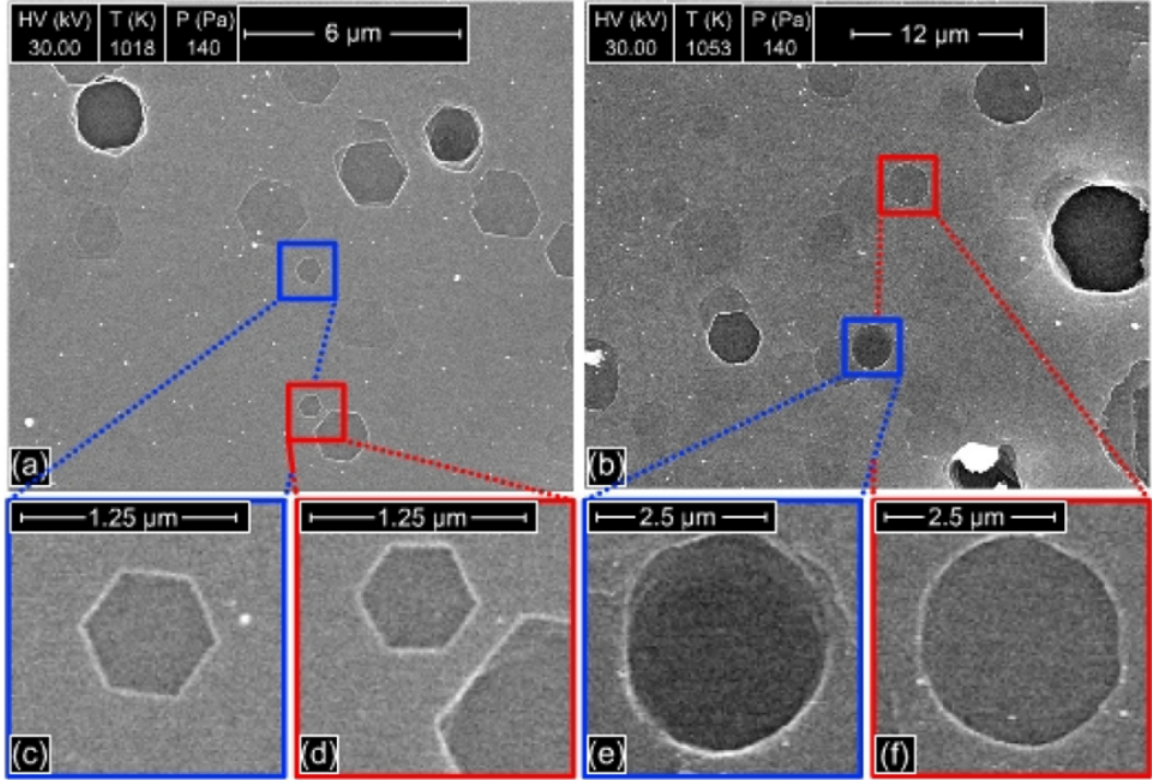
Figure 2.10: Pit geometry transition with temperature, from hexagonal (low T) to circular (high T). Reprinted from [19], with the permission of AIP Publishing.

2.2.2 Computational Studies

While there exists a relatively large number of experimental studies on pitting, fewer computational studies have been attempted to this day. In order to prove the heuristic argument made by Hughes, Williams, and Thomas [50] that armchair edge sites need to be oxidizing much faster than zigzag edge sites in order to produce hexagonal pits, Eklund [61] and later Brown [62] devised simple Monte Carlo computer simulations that would remove either zigzag or armchair carbon sites from a graphene sheet. The ratio between the rates of removal of either type of edge carbon was changed in order to demonstrate that this heuristic argument in fact holds true. Later on, Delehouzé et al. [19] picked up this same idea in order to explain temperature dependent shape transition of pits on that same basis. Since the underlying algorithm for these simulations is somewhat similar to the Kinetic Monte Carlo (KMC) method that is

used in this study, a reproduction of some of the results is provided in Appendix A.1. Interestingly, having zigzag edge atoms be removed much faster than armchair edge atoms does not lead to hexagonal pits with armchair edges. Instead, the pits become circular, with roughness along the perimeter of the pit. While this gives a good validation for the heuristic argument made by Hughes, Williams, and Thomas [50], no further information can be gained from these studies, due to the lack of actual chemistry that is simulated.

Using molecular dynamics, Poovathingal et al. [63] were able to simulate the oxidation of graphite by hyperthermal atomic oxygen, using the ReaxFF force field [64]. To the authors best knowledge, this is the first computational study where etch pits have been simulated truly from atomic processes. However, with their approach, only short total times can be simulated. In fact, they had to use a two-step process to accelerate the simulation such that around a thousand collisions could be simulated. While hyperthermal atomic oxygen may oxidize graphite fast enough to produce etch pits with such few collisions, that is not the case with regular oxygen gas at thermodynamic equilibrium even at temperatures up to $2000\,\mathrm{K}$. At lower temperatures, pitting can take seconds, which is far out of reach for any molecular dynamics approach. This is where this work seeks to add value: By providing a computational framework to simulate carbon oxidation at the atomic level to long timescales, graphene etching and pitting of graphite are studied from first principles in heretofore unattainable detail.

On an even more fundamental level, a number of studies have been performed in order to identify the elementary surface reactions during carbon oxidation and the corresponding reaction energies. The earliest studies used molecular orbital theory [65–68] to calculate the intrinsic oxidation rates of different kinds of carbon edge species occupied with oxygen adsorbates. More recently, the more accurate Density Functional Theory (DFT) method has been utilized for that same purpose [69–81].

These studies form the basis upon which the kinetic reaction mechanism for this study is built in Chapter 4.

It should be noted that the DFT studies are performed on different level of theory, with varying model geometries. For example, Sendt and Haynes [69–75] as well as Montoya et al. [78] and Montoya, Mondragón, and Truong [79, 80] have performed DFT calculations at the B3LYP level of theory, while Larciprete et al. [76, 77] and Šljivančanin et al. [81] have used PBE functionals. This potentially affects the accuracy of the kinetic reaction mechanism, since energies calculated from DFT can vary slightly when different levels of theory are used. Hence, as is described in Chapter 7, a complete and coherent DFT study of all reactions comprising the novel mechanism proposed in this work potentially can further increase its accuracy.

Chapter 3 Computational Approach

This chapter describes the novel computational framework that has been devised in this work for the study of carbon oxidation at the atomic level. First, a precise formulation of the computational problem is provided in Section 3.1, and its resulting applicability and limitations are discussed with respect to the background knowledge about carbon oxidation developed in Chapter 2. After that, the methods that comprise the novel computational framework are described on a conceptual level in Section 3.2.

3.1 Problem Formulation

3.1.1 Problem Setup

Figure 3.1 schematically shows the physical setup of the reaction system that is studied in this work: A single-layer graphene sheet is exposed to oxygen gas from one side. The graphene sheet is flat, and initially free of any adsorbed species. Monovacancy defects that function as seeds for oxidation are introduced into the graphene sheet prior to gas exposure. The gas is a homogeneous mixture of molecular and atomic oxygen.

The temperature T_{solid} of the graphene sheet is considered to be uniform, and in thermal equilibrium with the temperature T_{gas} of the homogeneous gas mixture, such that $T_{solid} = T_{gas} = T = constant$. Note that T is kept constant throughout each simulation. Simulated temperatures are ranging from $T = 850\,\text{K}$ to $T = 2000\,\text{K}$.

If not mentioned otherwise, the gas is considered to be in chemical equilibrium, such that the total gas pressure $P = P_{O_2}(P,T) + P_O(P,T) = constant$ is given by the sum of the partial pressures of molecular oxygen P_{O_2} and atomic oxygen P_O.
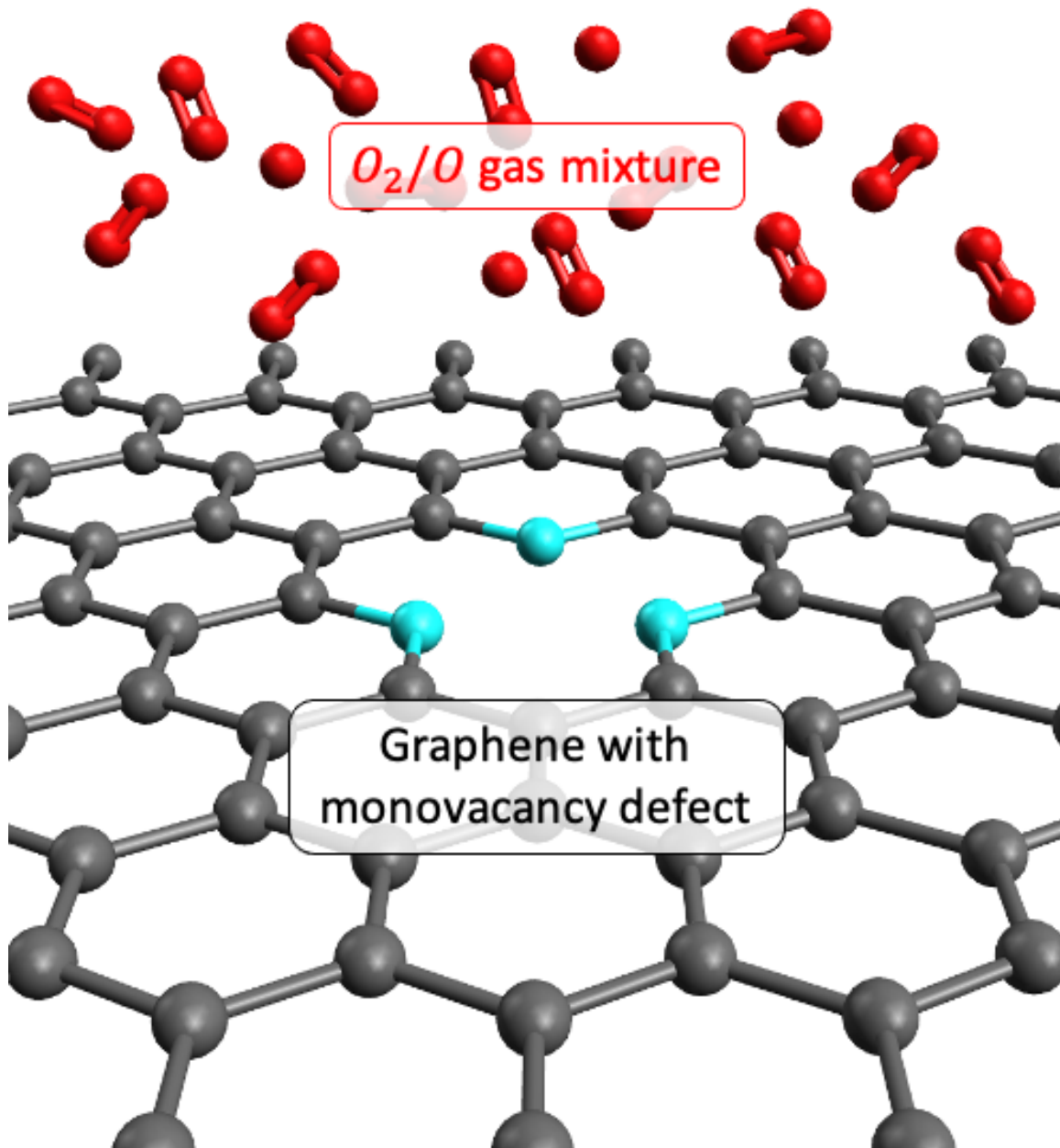
Figure 3.1: Problem setup: graphene is oxidized in an oxygenic environment. C-atoms are colored in grey, O-atoms are colored in red, and the three zigzag carbon edge sites surrounding the monovacancy defect are colored in blue.

Again, notice that P is kept constant for each simulation. The partial pressures and therefore the composition of the gas depend on both T and P, and must be calculated for all simulated conditions. Simulated total pressures range from $P = 0.01\,\mathrm{mbar}$ to $P = 100\,\mathrm{mbar}$.

3.1.2   Applicability and Limitations

Carbon Material   From the perspective of the carbon material, it is obvious that the problem setup mimics the conditions of an ideal graphene etching setup. In regards to how such a setup compares to practical conditions, there are two major points that require discussion: the isolation and flatness of the graphene sheet, as well as its pristine nature with respect to the presence of defects and impurities.

It is well known that single-layer graphene is prone to wrinkling to various extents for example due to intrinsic thermal fluctuations [82] or structural defects [83]. This phenomenon itself can be utilized in clever ways for manufacturing GNR, at least on a laboratory scale [84]. Furthermore, the curvature induced by wrinkling has been shown to locally affect chemical reactivity [85]. Most of these findings have been made on the basis of computer simulations of freestanding graphene, which itself is only an idealized model for real graphene materials. However, there is no evidence that wrinkling plays any practically significant role in either graphene etching or pitting of graphite. In fact, it can be argued that practical setups inhibit wrinkling. Graphene is typically either deposited on a flat solid substrate [86] or suspended between solid support columns [18]. Graphite on the other hand intrinsically supports the outer surface layer through intermolecular Van der Waals forces. In all those cases, the support structure exerts attractive forces on the graphene sheet that counteract the forces that tend to wrinkle freestanding graphene sheets in simulations. Hence, unless experimental evidence emerges that clearly shows the effect of wrinkling, there is no apparent reason for removing the added convenience and simplicity of considering a

flat graphene sheet on the basis of possibly induced inaccuracy.

Moreover, as it has been shown in Chapter 2, there is no apparent difference between carbon oxidation in the context of graphene etching and pitting of graphitic surfaces. The surface layer of graphite reacts just like an isolated graphene sheet on its own. Again, the reason is that the intermolecular forces between separate graphene layers in graphite are far weaker than the forces exerted by the covalent carbon bonds within each graphene layer. Therefore, an isolated flat single-layer graphene sheet is expected to be an accurate model representation for both graphene and graphite materials in real applications. Note that pitting a graphite crystal in depth, i.e. across multiple graphene layers into the bulk graphite crystal, is not directly studied here. While this can be viewed simply as a consecutive reaction of isolated graphene sheets, where one layer after another starts to react once it is uncovered by pitting of the previous layer, effects such as a curved morphology of pit bottoms [40] may or may not be explicable on this basis, and more complex information about the structure and defects in the graphite crystal likely needs to be taken into account.

This directly leads into the second point of discussion here regarding possible defects and impurities in the carbon material. As mentioned in Chapter 2, a number of different types of crystallographic defects are known to exist in graphite and graphene, and they certainly can have a combined effect on the macroscopic oxidation behavior of carbon materials. However, as will be seen later, the restriction to monovacancy defects for the fundamental study of carbon oxidation already delivers sufficient results to explain many aspects of graphene etching and pitting. Again, it is expected that moving from graphene into graphite, this simple approach might reach its limits, based on the complexity in the material structure of the actual graphite crystal that is studied. In particular, grain boundaries are structurally complex and diverse, and their exact composition is still poorly understood, which makes a true fundamental study of those elusive at this point.

With regards to impurities, i.e. the existence of foreign atoms in the carbon matrix itself or adsorbed to its surface, it is well known that they can both speed up or slow down the reaction [58]. The phenomenology is quite rich, it is both possible to observe simple etching figures like hexagonal or circular pits, but channeling due to moving catalyst particles is also often observed [53, 87]. It is however difficult to account for impurities in a fundamental study for several reasons. First, there is a large number of possible impurities in even more possible configurations, so accounting for each and every possible one is elusive. Second, just including a subset that is deemed necessary would require knowledge about their exact positions in the carbon material, which is still not existent. Again, this is not to so much a problem for analyzing graphene etching in the context of this work. But rather, impurities are likely to play a role in macroscopic oxidation behavior of graphitic carbon materials.

Gas Composition This study is restricted to oxygen in molecular and atomic form as the only reactive gas species. This assumption is made on the basis that the carbon-oxygen reaction is at least an order of magnitude faster than the reaction with other prominent gas species like CO_2 and H_2O [58]. Hence, as long as gases are studied with oxygen as a major constituent, this problem setup yields an accurate model.

In typical oxidative graphene etching experiments, oxygen gas is used with or without the addition of argon [18, 19, 86]. Besides that, graphite is typically oxidized in atmospheric air [60, 88]. Hence, for comparison with experimental results, there is no inaccuracy expected from the restriction to simple oxygen gas.

In respect to ablation in hypersonic applications in the earth's atmosphere, the major reactant is atomic oxygen, which is included here. However, atomic nitrogen can also play a role [89, 90] and therefore may need to be added to the present setup in order to increase accuracy. Yet even more reactive gas species may be required

for the study of ablation in other planetary systems, for instance mars where the atmosphere consists predominantly of carbon dioxide.

Range of Conditions   The low temperature cutoff of $T = 850\,\text{K}$ is chosen due to the low temperature limit at which carbon oxidation is observable in the form of etch pits. This limit is naturally given by the reaction kinetics. For the sake of this argument, let's assume that the oxidation rate is following an Arrhenius equation such that it is proportional to temperature as *oxidation rate* $\propto exp(-1/T)$. Hence, the oxidation rate drastically decreases at low temperatures. The lowest temperature at which pits have been observed is $773\,\text{K}$ [60], with oxygen pressures corresponding to atmospheric air. At that temperature, the sample needs to be oxidized for hours up to days in order to create large enough pits that are detectable with microscopy. Such long physical times are not feasible to simulate with computational methods at the atomic level. Here, $T = 850\,\text{K}$ has been found to be the lowest temperature at which simulations are still feasible for all considered pressures.

On the high temperature end, this study is limited through the selection of the computational methods. This limitation comes from the kinetic reaction mechanism, which is described in Chapter 4. The actual reason will become more clear from the descriptions in Section 4.1, but in general it is due to the fact that more and more reactions need to be added to the mechanism with increasing temperature. In that respect, $T = 2000\,\text{K}$ was chosen as a reasonable compromise between complexity of the mechanism and high enough temperatures to reach conditions relevant for ablation. At even higher temperatures, other gas species start to play more significant roles and would need to be included. Furthermore, the carbon structure itself can start to undergo transformations [91, 92], which would be hard to capture with the present computational approach.

3.2 Selection of Computational Methodologies

To start with, it is instructive to recall at which timescales and length scales graphene etching and pitting of graphite are taking place. Typically, one observe etch pits in microscopic images with sizes ranging from a few nanometers (10^{-9} m) to a few micrometers (10^{-6} m) in diameter. At the micrometer level, growth of isolated pits becomes less likely due to the pit potentially coalescing with other pits or approaching grain boundaries. To etch those pits, experiments are typically performed anywhere between a few seconds to minutes or even hours in extremely slow cases ($1\,\text{s}$-$10^3\,\text{s}$). However, the overall carbon oxidation process fundamentally results from elementary atomic scale processes. These elementary processes are ultimately driven by atomic motion, which takes place roughly at the timescale of picoseconds ($10^{-12}\,\text{s}$).

The objective of this research is to study this phenomenon computationally based on first principles. For that purpose, a consideration of commonly used computational methods for the study of comparable chemical surface reactions is useful. Figure 3.2 compares methods that are widely used to study heterogeneous catalysis reactions according to the length- and time scales that are feasible to reach with current computational resources.

As has been discussed, pitting occurs at nano- to micrometer length scales and time scales on the order of seconds. From Figure 3.2 it is clear that the Kinetic Monte Carlo (KMC) falls into that regime. KMC is directly linked to the atomic scale through a kinetic reaction mechanism that incorporates reaction rates derived from first principles. Such a kinetic mechanism for carbon oxidation did not exist prior to this research, and its development is one of the major contributions of this work. The mechanism development is discussed in detail in Chapter 4.

At the atomic level, the reaction rates are derived on the basis of transition state theory (TST). TST builds on the concept that surface reactions are governed by the energetics of the system which are described by a potential energy surface (PES). The
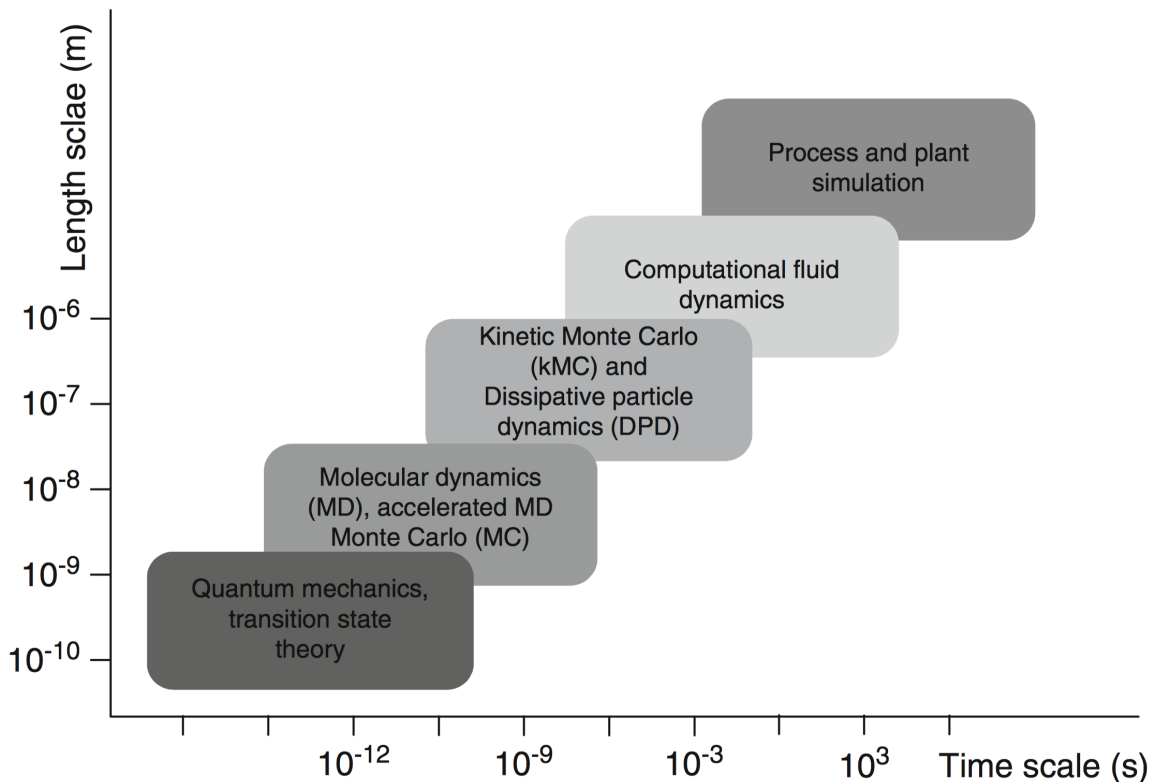
Figure 3.2: Comparison of common computational methods for chemical surface reactions according to their feasibility in time and length scales. Reprinted by permission from Springer Nature: Multiscale Molecular Methods in Applied Chemistry by B. Kirchner et al., Copyright (2011), book chapter [93].

PES itself can be constructed numerically through solutions to the governing quantum mechanical system using density functional theory (DFT). DFT is the fundamental element of this approach that links KMC to first principles.

Coming back to Figure 3.2, on even longer time or larger length scales KMC is replaced by computational fluid dynamics (CFD). However, while it is possible to retain atomic resolution with KMC, CFD is inherently build on continuum mechanical formulations. Hence, it is not suited for a fundamental study of carbon oxidation at the atomic level. On the other hand, at shorter timescales and smaller length scales, molecular dynamics (MD) methods become more attractive relative to KMC. One main advantage of MD versus KMC is the fact that while KMC requires a lot of specific input about the reacting system in the form of a kinetic reaction mechanism,

MD only needs a more or less general force field to simulate the dynamics of the atomic system. For the oxidation of hydrocarbons, the ReaxFF force field has been developed [64, 94], and it has been applied to study oxidation of HOPG in extreme conditions with hyperthermal atomic oxygen[63]. However, with MD it is elusive to study carbon oxidation with respect to graphene etching and pitting at more realistic conditions, due to the long timescales involved.

At this point, the motivation for the selection of computational methods for this study should be clear. All these elements that comprise this computational approach are described in more detail on a conceptual level in the following subsections.

3.2.1 Potential Energy Surface and Density Functional Theory

The potential energy surface (PES) of an atomic system such as the one defined in the problem setup for this work describes the system's energy $E(\mathbf{r})$ as a function of its geometry $\mathbf{r}$, i.e. the location of all involved atoms relative to each other. The dimensionality of the PES is therefore equal to its total number of degrees of freedom. In a system with N atoms, this typically comes down to a total of $3N-6$ dimensions. While such a large number of dimensions is impossible to visualize, it is useful to think of the PES as an energy landscape.

To demonstrate the value of this conceptual analogy, consider the three dimensional model PES shown in Figure 3.3 [95]. Each point on the surface corresponds to a unique geometrical configuration $\mathbf{r}$ of the overall system, with its corresponding energy $E(\mathbf{r})$ given by the height in the vertical direction. A number of characteristic points on the PES are denoted in Figure 3.3, namely inflection points, second order saddle points, local minimum points and transition structures. The latter two are significant from the standpoint of transition state theory, as it is described in the following section. The important thing to notice here is that those points can be found purely from geometrical considerations of the PES, and yet they carry useful
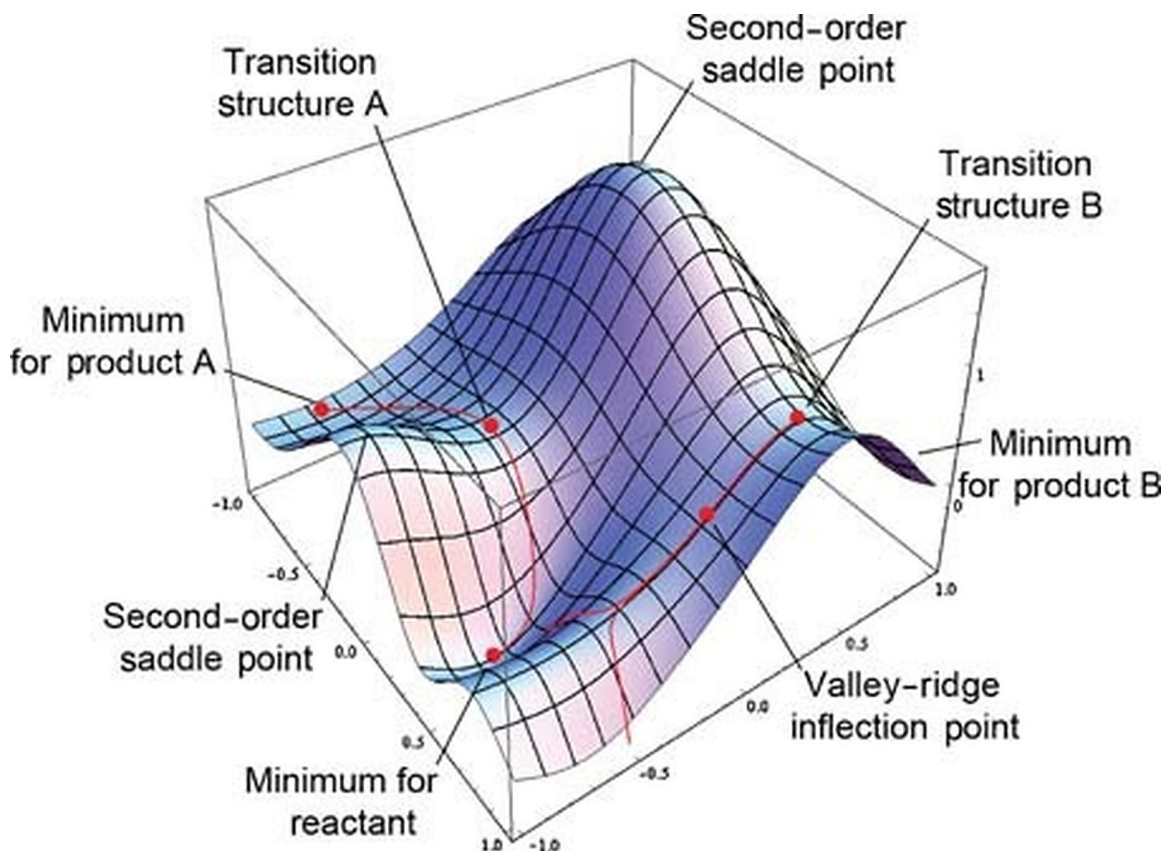
Figure 3.3: Model potential energy surface displaying characteristic points and paths relevant for transition state theory. Reprinted from [95] with permission from John Wiley & Sons.

information about the physics and chemistry of the reaction system.

In the context of this computational study, it is important to be able to numerically calculate $E(\mathbf{r})$. Fundamentally, this requires the solution of the system's Schrödinger equation. The Schrödinger equation is the most fundamental description of a quantum mechanical system, and this is where the computational approach truly is linked to first principles. However, it is impossible to solve the Schrödinger equation for any but the smallest systems with few atoms. Instead, Density Functional Theory (DFT) is applied to yield approximate solutions for larger systems. For that purpose, the first fundamental step is to apply the Born-Oppenheimer approximation. On the basis that an atom's nucleus is much heavier (and therefore slower) than its electrons, the Born-Oppenheimer approximation states that the motion of

the electrons can be separated from that of the nucleus. Therefore, when calculating electronic structures and energies, atom locations, i.e. the position of the nucleii, can be considered stationary. The crucial step in DFT that allows to further simplify the calculations is the replacement of the wavefunction in the Schrödinger equation with a single electron density that is only a function of three spatial coordinates and time, regardless of the number of atoms in the system (unlike the wavefunction). The theory behind DFT now states that if this electron density is known, the ground state energy of the system can be derived. In other words, the energy is a function of the density which is a function of space and time, hence the name density functional theory.

In practice, DFT is a standard tool for the calculation of energies of systems with many atoms, particularly in the context of surface reactions [96–98]. In this work, no DFT calculations have actually been performed. Merely, the results of DFT calculations in existent literature are utilized in Chapter 4 for the construction of a kinetic reaction mechanism.

3.2.2 Transition State Theory

Graphene etching, just like many other (catalytic) surface reactions, is the result of different types of elementary surface reactions: adsorption and dissociation of gas species onto the graphene surface, migration of surface species through diffusive hops between nearby carbon sites, and the desorption of surface species as oxygen and CO oxidation products.

On a more abstract level, one can think of thes elementary processes as transitions between local minima on the potential energy surface (PES) of the system. This idea is sketched out in Figure 3.4. Most of the time, the system will oscillate around the minimum basin of its current state (e.g. epoxy oxygen adsorbate is vibrating in its current bonded location) at timescales of atomic vibrations. In rare occasions,
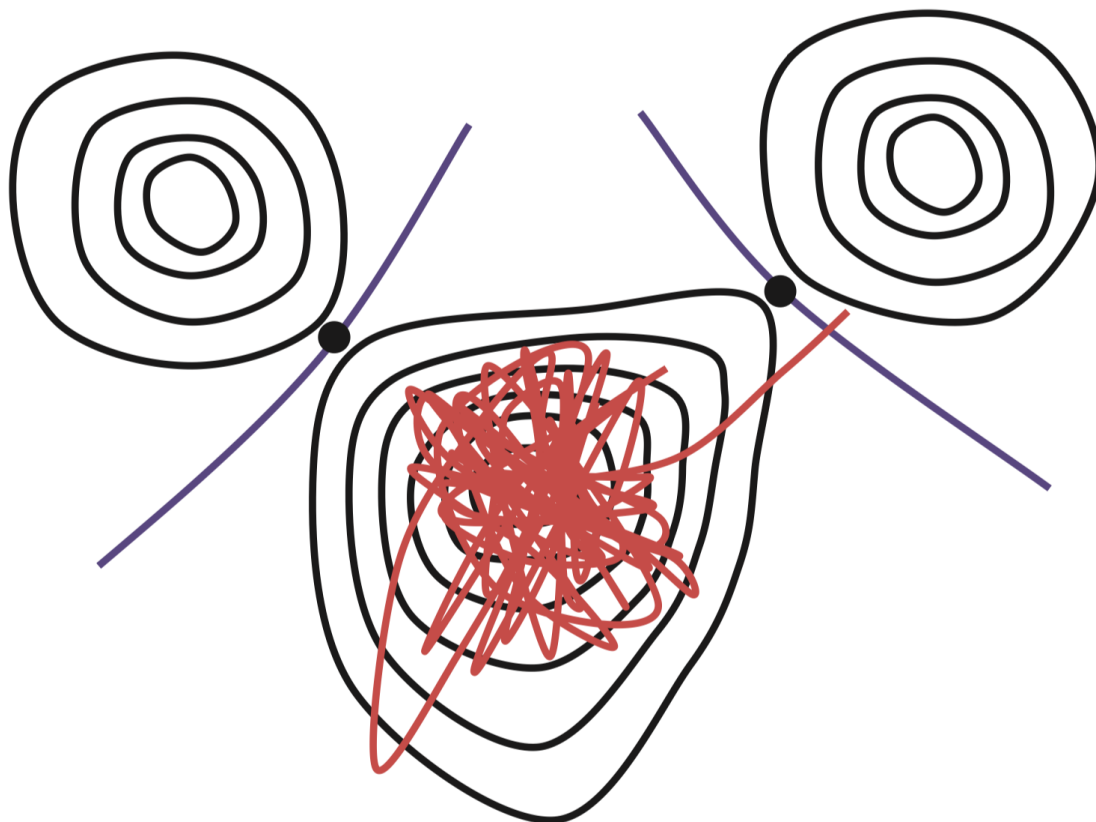
Figure 3.4: Isocontours of model potential energy surface (PES) with typical trajectory of a rare transition event. The dots represent the actual transition states on the PES. Reprinted by permission from Springer Nature: Radiation Effects in Solids by K. E. Sickafus et al., Copyright (2007), book chapter [99].

at timescales much slower than atomic vibrations, an elementary event will happen which is able to overcome the energy barrier on the PES and push the system into a new state (e.g. diffusive hop of an epoxy to a nearby bridge site). This transition occurs approximately along the reaction coordinate so that the trajectory is going through or close by transition structures on the PES. In fact, it is most likely to follow the minimum energy path connecting the reactant state to the product state. The effect of the long oscillation periods inside a minimum basin between elementary events is that the system looses the memory of previous state transitions. In other words, all elementary events are completely independent of each other, and consecutive events are uncorrelated.

In the context of Transition State Theory (TST), the intrinsic rate of each elementary reaction can be approximated as an Arrhenius rate which takes the form

$$k = A \exp\left(-\frac{E_a}{k_B T}\right) ,$$ (3.1)

with a pre-exponential factor A and an activation energy E_a (both specific to each process) as well as temperature T and Boltzmann constant k_B. The parameters A and E_a can in principle be calculated exactly from quantum mechanics. More specifically, for surface processes A is derived as

$$A = \frac{\prod_i^{3N} \nu_i^{min}}{\prod_i^{3N-1} \nu_i^{sad}} ,$$ (3.2)

with the normal mode frequencies ν_i^{min} at the reactant state and ν_i^{sad} at the transition state [99–101]. For adsorption reactions, which are driven by the kinetic energy of gas particles, A is instead derived from a Boltzmann distribution as described in Section 4.2 and Appendix A.2. The activation energy E_a is simply calculated as

$$E_a = E_{sad} - E_{min}$$ (3.3)

i.e. the difference in energy between the transition state (saddle) and reactant state (minimum). Both A and E_a for all elementary surface reactions used in this work are collected from existing DFT literature.

3.2.3 Kinetic Monte Carlo

The Kinetic Monte Carlo (KMC) method inherently builds on the previously described property of the reaction system, that consecutive events, i.e. elementary surface reactions, are uncorrelated. In stochastic terms, the carbon oxidation process can therefore be viewed simply as a chain of those uncorrelated events, which is referred to as a Markov chain, and the process itself is called a Markov process [102].

The idea of KMC is now to neglect all nonreactive vibrations that occur on very fast timescales in the system and just simulate the slower elementary processes in a

probabilistic manner, since carbon oxidation is the result only of those elementary processes taking place on the surface. This allows KMC to simulate to much longer times as compared to conventional deterministic atomic simulation methods like MD, which have to fully resolve the atomic vibrations themselves.

To understand how KMC actually works, the stochastic simulation algorithm (SSA), which is performed within KMC to realize a Markov chain, is briefly outlined here:

Step 1: Initialize the system in a desired state and set simulation parameters,

Step 2: Identify all elementary events i possible at the initial state, and for each generate a random inter-arrival time

$$\tau_i = -\frac{1}{k_i} \ln(1 - u), \tag{3.4}$$

based on its intrinsic rate k_i and a random number $u \in (0, 1)$,

Step 3: Find the elementary event i with the closest inter-arrival time τ_i to the current time t, increment t by τ_i, and change the state of the system according to that event,

Step 4: If $t > t_{final}$, stop the simulation. If not, continue with step 5,

Step 5: Discard elementary events that are not possible anymore in the new state, identify all newly possible elementary events and generate their inter-arrival times,

Step 6: Go back to step 3.

Notice that the inter-arrival time τ_i is essentially an exponentially distributed random number with a mean value of $1/k_i$. To be more precise, it is a sample from the probability density function describing the probability that the event i will happen at time $t + \tau_i$, provided that the system at time t is in a state that allows for event i

to occur. Its form directly follows from treating the elementary processes as Poisson processes, i.e. uncorrelated events. This algorithm goes back to Gillespie [103, 104], and has been proven extremely useful for the stochastic simulation of chemically reacting systems [105–107].

It should be mentioned that the more or less intuitive arguments from above can be expressed in a more rigorous formalism in terms of a set of coupled stochastic ordinary differential equations (ODEs). The resulting set of equations in the context of chemically reacting systems is called chemical master equation (CME) [108]. In the context of the CME, KMC is a method to generate a random walk on the system's state space that satisfies the CME. Such a random walk is also referred to as a stochastic realization of the overall random oxidation process [106].

From a practical perspective, most of the computational effort in the SSA is spent on step 5. Modern lattice-based KMC codes utilize search tree algorithms to efficiently identify possible elementary events [109–113]. In those frameworks, the reaction system (here the graphene sheet) is directly represented by a lattice. This makes it possible to fully resolve every atom in the system. Through the search tree structure, the neighboring structure of those atoms is explicitly accounted for. This in the end significantly accelerates the search for new possible elementary events at each KMC simulation step, since the elementary processes act locally by changing the state of only a few neighboring atoms. The code selected for this study is Zacros [113, 114], which is readily available for academic use. It has been used to study a variety of different catalytic surface reactions [115–120], and this study adds the oxidation of graphene as yet another surface reaction to that list. Interestingly, Zacros has also been used to study fluid transport in porous networks [121].

In order to get accurate results from KMC, all kinds of elementary processes have to be known beforehand and provided to KMC in the form of a kinetic reaction mechanism, each with an intrinsic rate k_i. In carbon oxidation, those are the adsorption

and dissociation of oxygen on the graphene surface, diffusion of oxygen adsorbates, as well as the desorption of oxygen species or the oxidation of carbon edges. The development of this mechanism is described in Chapter 4, followed by a discussion of its implementation in Zacros.

Chapter 4 Kinetic Carbon Oxidation Mechanism

In this chapter, a comprehensive, atomic-scale reaction mechanism for carbon oxidation is developed. Before actually discussing all elementary reactions that enter in this mechanism (Section 4.2), it is important to first discuss the guiding principles that lead into the construction of the mechanism, as well as to recall some of the assumptions that are made along the way.

4.1   Guiding Principles and Assumptions

In order to construct a kinetic mechanism for graphene etching, it is essential to have a clear understanding of the reaction system itself, and the elementary surface reactions that take place. Based on that knowledge, a number of assumptions need to be made in order to obtain an accurate yet feasible mechanism for KMC simulations. This clearly has implications towards the applicability of this novel mechanism.

The present study considers only the gas-solid reaction between a single sheet of graphene and oxygen gas, as described in Section 3.1. Any other gas species, for instance nitrogen, is not considered in the mechanism, based on the observation that oxygen reacts orders of magnitudes faster with carbon than other gas species [58]. Furthermore, only CO is considered as a reaction product, since it is has been found to be the dominant reaction product at practical reaction conditions [122]. Once desorbed, CO only weakly interacts with graphene as compared to O_2, so any possible reactions between graphene and desorbed CO are neglected. Lastly, oxygen is contained in both atomic and molecular form, since already small concentrations of O, which are present in chemically equilibrated oxygen gas at elevated temperatures, play an important role in the reaction process.

The graphene sheet is considered to be flat at all times, and it is comprised

of four different types of carbon sites: On the basal plane, carbon sites are fully incorporated in the hexagonal structure with three carbon neighbors. In contrast, on the edge, carbon sites are missing at least one neighboring carbon atom. They are categorized into zigzag, armchair and dangling carbon edge sites, based on the neighboring structure, as was described in Section 2.1. While zigzag and armchair sites both have two remaining carbon neighbors, they differ such that the carbon neighbors are both basal plane carbons in the case of zigzag sites, whereas armchair sites have at least one edge site as a neighbor. Dangling carbon sites on the other hand only have a single carbon neighbor. This model of the graphene sheet allows a straightforward and consistent implementation in the lattice based KMC code Zacros used for this study.

The only adsorbed surface species are oxygen adsorbates. Other adsorbates, for instance hydrogen species which might be present at graphene edge sites, are neglected. This assumption has been widely used to study edge processes in the oxidation of carbon materials with low hydrogen content [66]. However, it should be noted that studies exist also on carbon structures where the edges are predominantly passivated with hydrogen, for instance Poly-Aromatic Hydrocarbons (PAH), which are of interest in soot formation during combustion [123]. Hence, since this mechanism is focusing on carbons with low H/C ratio such as graphite and graphene, it might be inaccurate if directly applied to carbons with large H/C ratio.

Recall the intrinsic rate equation for elementary surface processes

$$k = A \exp\left(-\frac{E_a}{k_B T}\right) .$$

One interpretation for this rate equation is to view the pre-exponential factor A as the attempt frequency to perform an elementary process, while the exponential factor represents the probability that the process is actually performed. Hence, in order to study carbon oxidation, only those processes that have a high enough probability to occur at the timescale of pitting itself need to be considered. At the upper temper-

ature limit of $2000\,\text{K}$, etch pits grow at least at a rate of a few tens of nanometers per second ($\approx 10^1\,\text{nm}\,\text{s}^{-1}$) at low pressures, which corresponds to a removal rate of carbon atoms on the order of hundreds of thousands of carbon atoms per second ($\approx 10^5$ *carbon atoms*/s) or more. With a typical attempt frequency $A \approx 10^{13}\,\text{s}^{-1}$ for surface processes, which is on the order of magnitude of the frequency of atomic vibrations for example in the C-O bond [124], this translates to a minimum probability of around 10^{-8} for processes to actually play a role. This translates to a maximum activation energy of $E_a = 3\,\text{eV}$ for thermally activated surface processes. Hence, in the following construction of the mechanism, elementary reactions that might be identified in the DFT literature, but have higher activation energies than $E_a = 3\,\text{eV}$, are not included. Note that for adsorption processes, the attempt frequency A is given by the collision frequency of gas particles with the surface, as described in the following section. The resulting attempt frequencies are significantly lower, on the order of $A \approx 10^2\,\text{s}^{-1} - 10^7\,\text{s}^{-1}$, depending on the pressure. However, as will be seen below, the activation energies are much lower than the cutoff of $E_a = 3\,\text{eV}$, so that the adsorption reactions are still fast enough even at low temperatures.

For oxidation of HOPG at high temperatures by a molecular beam with molecular and atomic oxygen in the ground state [125], it has been found that oxidation occurred predominantly from Langmuir-Hinshelwood (LH) type reactions, i.e. thermally activated oxidation reactions involving adsorbed species. In contrast, Eley-Rideal type reactions, which directly result from a collision of gas particles with the carbon surface, have found to be insignificant. For that reason, only thermal oxidation reactions (LH) are included in this mechanism.

4.2 Mechanism Construction

Graphene etching, just like many other (catalytic) surface reactions, is the result of different types of elementary surface reactions: adsorption and dissociation of gas

species onto the graphene surface, migration of surface species through diffusive hops between nearby carbon sites, and the desorption of surface species as oxygen and CO oxidation products.

Based on their intrinsic rates k, elementary reactions are only included in the mechanism provided they are faster or on the timescale of interest in graphene etching. As discussed above, for temperatures below $2000\,\mathrm{K}$ and $A = 10^{13}\,\mathrm{s}^{-1}$, this is roughly at $E_a < 3\,\mathrm{eV}$. Other reactions that may have been discussed in DFT studies are neglected in this mechanism. However, these may be important when extending this mechanism to even higher temperatures in the future.

For adsorption processes, A can be derived as the collision frequency $k_{collision,O2}$ of O_2 molecules with the graphene surface based on thermal equilibrium (see Appendix A.2 for a derivation). This writes as

$$k_{collision,O_2} = \frac{P_{O_2} A_{eff}}{2\pi m_{O_2} k_B T} \, ,\tag{4.1}$$

where $A_{eff} = 2.6199\,\mathrm{\mathring{A}}^2$ is the effective surface area of a carbon site on the graphene basal plane, P_{O_2} is the partial pressure of molecular oxygen, and m_{O_2} is the mass of an oxygen molecule. Similarly, $k_{collision,O}$ for atomic oxygen is derived by replacing the partial pressure and particle mass accordingly. For all other elementary processes, in cases where only E_a is reported in the literature, A is assumed to be $A = 1 \times 10^{13}\,\mathrm{s}^{-1}$. This is the timescale of vibrational frequencies for example of a C-O bond in a surface species, and it is routinely taken as the estimate for A in surface processes in KMC studies [99].

Figure 4.1 shows all oxygen adsorbates that play a role in the carbon oxidation process and therefore appear in the mechanism. They have been identified by a careful cross examination of the available literature, and ultimately some trial and error going back and forth between simulations and further refining the mechanism. It should be noted that this is by no means a complete list of all possible configurations an oxygen species can bind to a graphene sheet.
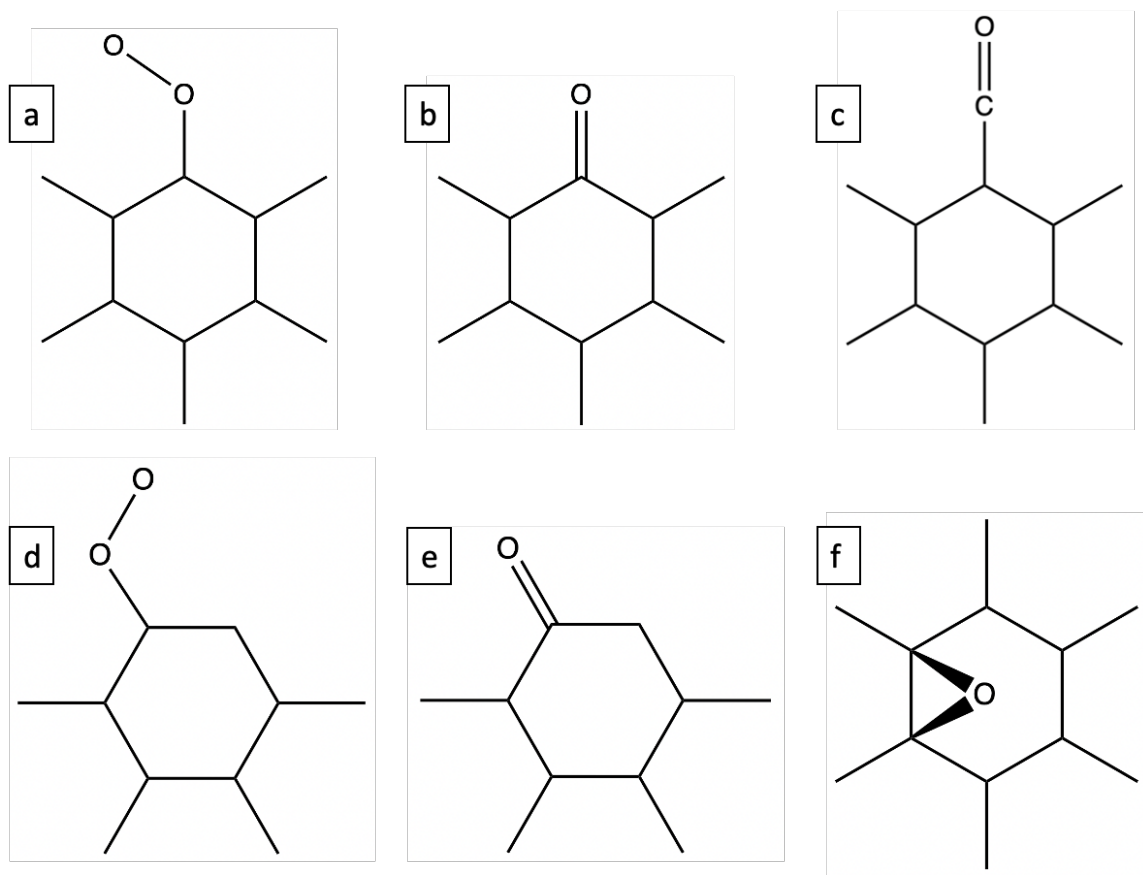
Figure 4.1: Adsorbed oxygen surface species: Molecular oxygen adsorbed to zigzag edge $O_{2,\text{zz}}$ (a), zigzag semiquinone (b), ketone (c), molecular oxygen adsorbed to armchair edge $O_{2,\text{ac}}$ (d), armchair semiquinone (e), epoxide (f).

The following subsections are divided into the different types of elementary surface reactions, and all reactions entering the mechanism are discussed in detail. The mechanism itself is listed in Table 4.1 in full. The parameters A and E_a are directly taken from the DFT literature. In rare cases, where multiple studies can be found on the same elementary reaction, A and E_a are taken as the average between those studies. Furthermore, it needs to be noted that select reactions involving complex edge geometries are not directly calculated in DFT but can be inferred from the elementary reactions on the simpler edge geometries. This comes back to the idea expressed in Section 2.1 about zigzag and armchair edges being the basic types of edge structures, but they can form more complex edge structures like bays, gulfs, coves

and fjords. The reactions where this step has been necessary are clearly marked with an asterisk in the "Reference" column of Table 4.1.

4.2.1 Adsorption and Dissociation

The first surface process that occurs is the adsorption of oxygen atoms and molecules from the gas phase onto the graphene surface. Since this study considers carbon oxidation at elevated temperatures, physisorption phenomena can be disregarded, due to the fact that physisorbed species are stable only at low temperatures. Hence, only chemisorption reaction are considered. Generally speaking, oxygen can either adsorb on the basal plane or on edge sites of graphene. On carbon edges, O_2 readily chemisorbs without any activation energy in the case of zigzag edges (ADS1, this and the following abbreviations refer to the reaction nomenclature in the mechanism in Table 4.1) [70, 75] and a small activation energy of $0.311\,eV$ on armchair edges (ADS2) [69, 74]. This chemisorption first occurs in molecular form, i.e. the oxygen molecule does not dissociate before adsorption. However, once adsorbed, the adsorbed oxygen molecule readily dissociates and forms two neighboring semiquinones on the edge, provided that a neighboring edge site is available for adsorption. Other pathways for dissociation, which become important at higher edge coverage, are discussed later. On the basal plane, O_2 cannot adsorb in molecular form. Rather, the oxygen molecule has to dissociate in the process of approaching the graphene layer, and finally form two neighboring epoxides on the graphene surface. This dissociation requires a larger activation energy of $1.7\,eV$ (ADS3) [76]. On the other hand, O is much more reactive and chemisorbs barrierless on all types of carbon sites (ADS4-7)[81].

Turning back to the adsorbed $O_{2,zz}$ and $O_{2,ac}$ species, they can dissociate in various ways. The easiest way, which was already mentioned previously, is the direct dissociation to form to neighboring oxygen species, provided that free neighboring edge sites exist. On zigzag sites, this dissociation into two O_{zz} (semiquinone) species

is nearly barrierless (DIS1) [70, 75]. On armchair sites, the energy barrier depends on the exact configuration. If the free neighbor is on the same ring, there is an energy barrier of 0.694 eV (DIS2) [69], whereas dissociation to a neighbor across two rings only takes 0.238 eV (DIS3) [74]. If no direct neighbors are free, the dissociation is much more difficult. In fact, only a single study dealing with this high coverage case has been found, and it is only dealing with zigzag sites [75]. The two additional pathways identified there are the migration of the $O_{2,zz}$ species until it finds a free neighbor to dissociate, and the dissociation to form an epoxide on the basal plane. The latter is referred to as oxygen spillover. The activation energies are 0.943 eV (DIFF2) [75] and 1.513 eV (DIS4) [75] respectively.

4.2.2 Diffusion
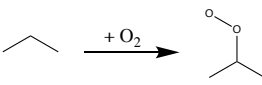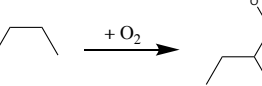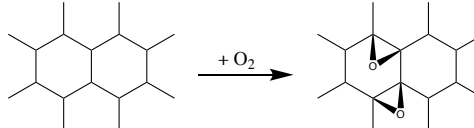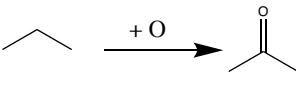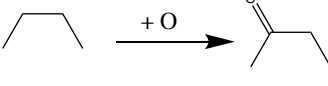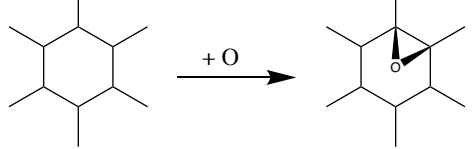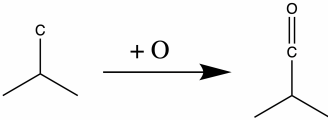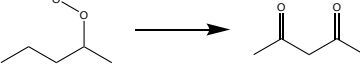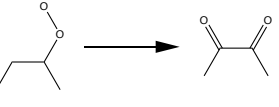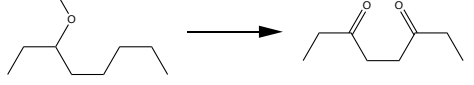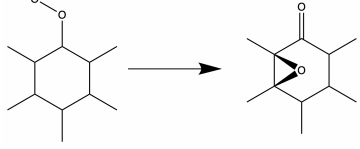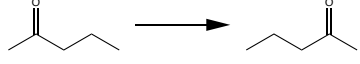
All surface species are able to migrate on the graphene surface, provided there are available neighboring sites. The fastest diffusive species are epoxides on the basal plane with activation energies of 0.73 eV (DIFF5) [76]. If epoxides are close to the graphene edge, they can also hop to an edge site and form edge oxygen species (DIFF8-10) [76]. Oxygen species on the edge can migrate along the edge. On armchair edges, this takes 1.399 eV (DIFF3, DIFF6) [72] or 1.275 eV (DIFF4,DIFF12,DIFF14) [72], depending on the armchair configuration, whereas on zigzag edges it takes 1.904 eV (DIFF1, DIFF11, DIFF13, DIFF15) [70, 72]. Furthermore, semiquinones can diffuse to a ketone with an activation energy of 1.904 eV (DIFF7) [70, 72]. As will become clear later, diffusion plays a key role in the mechanism in particular for the epoxide species on the basal plane, since they can significantly accelerate oxidation processes.
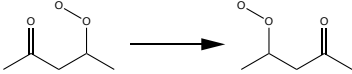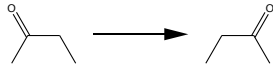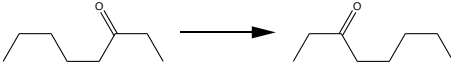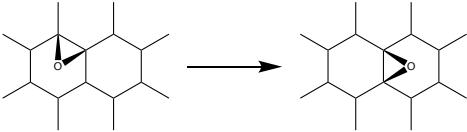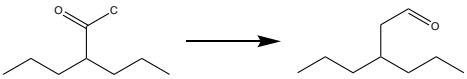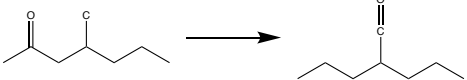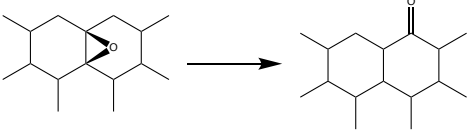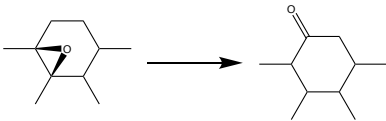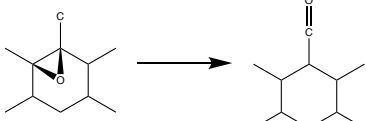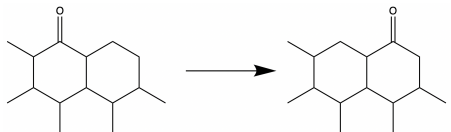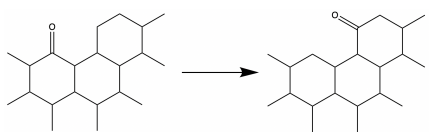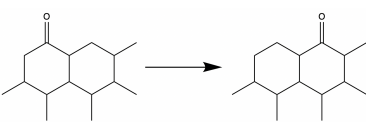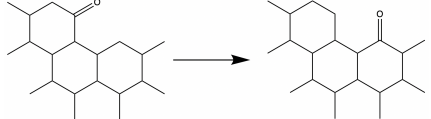
4.2.3 Oxidation and Desorption

Oxidation, i.e. the desorption of CO species from edge sites with oxygen adsorbates, has to be considered separately for armchair and zigzag edges in order to be able to predict isotropic and anisotropic etching. Generally speaking, isolated O_{zz} and O_{ac} species are very slowly desorbed. On armchair sites, this takes $2.743\,\text{eV}$ (OXac1, OXac5) [66], and on zigzag sites even $3.622\,\text{eV}$ (OXzz1) [66, 72]. If there are neighboring edge oxygen species, the activation energies lower to $1.704\,\text{eV}$ on armchair sites (OXac2, OXac6, OXac7) [66]. However, by far the most significant reduction in activation energies occurs if epoxide groups are neighboring the edge oxygen species. O_{zz} removal is facilitated to $2.3\,\text{eV}$ (OXzz2, OXzz3) [66, 72], and O_{ac} even down to $1.829\,\text{eV}$ (OXac3) [66] or $1.136\,\text{eV}$ (OXac4) [66], depending on the exact neighboring structure. This is a profoundly important characteristic of the reaction mechanism and carbon oxidation in general. Moreover, ketones, i.e. dangling carbons with adsorbed oxygen, also can desorb as CO with activation energies ranging from $2.17\,\text{eV}$ (OXd1) [78] down to $0.447\,\text{eV}$ (OXd2) [78] depending on the neighboring structure (OXd1-7) [66, 78].

In contrast, oxygen adsorbates can desorb back into the gas phase without removing carbon atoms from the graphene sheet. On the basal plane, this is theoretically possible through breaking both C-O bonds of an epoxide. However, this takes an activation energy of more than $3\,\text{eV}$ and is therefore not included in the mechanism. Instead, recombination of two nearby epoxides to form gaseous O_2 is much more likely with an activation energy of $1.13\,\text{eV}$ (DES3) [76]. The picture on graphene edges is somewhat similar in the sense that single oxygen species are extremely unlikely to simply desorb away as atomic O from an edge site. However, the O_2 adsorbates can desorb before dissociation with activation energies of $1.42\,\text{eV}$ (DES1) [75] and $1.104\,\text{eV}$ respectively for zigzag and armchair (DES2) [69, 74].

Table 4.1: Kinetic Reaction Mechanism

with rate constant: $k = A \exp\left(-E_a/k_B T\right)$

#	Reaction	$A\,(\mathrm{s}^{-1})$	$E_a\,(\mathrm{eV})$	Reference
ADS1	$\xrightarrow{+\,O_2}$	$\dfrac{P_O A_{eff}}{\sqrt{2\pi m_{O_2} k_B T}}$	0.000	[70, 75]
ADS2	$\xrightarrow{+\,O_2}$	$\dfrac{P_O A_{eff}}{\sqrt{2\pi m_{O_2} k_B T}}$	0.311	[69, 74]
ADS3	$\xrightarrow{+\,O_2}$	$\dfrac{P_O A_{eff}}{\sqrt{2\pi m_{O_2} k_B T}}$	1.700	[76]
ADS4	$\xrightarrow{+\,O}$	$\dfrac{P_O A_{eff}}{\sqrt{2\pi m_O k_B T}}$	0.0	[81]*
ADS5	$\xrightarrow{+\,O}$	$\dfrac{P_O A_{eff}}{\sqrt{2\pi m_O k_B T}}$	0.0	[81]*
ADS6	$\xrightarrow{+\,O}$	$\dfrac{P_O A_{eff}}{\sqrt{2\pi m_O k_B T}}$	0.0	[81]
ADS7	$\xrightarrow{+\,O}$	$\dfrac{P_O A_{eff}}{\sqrt{2\pi m_O k_B T}}$	0.0	[81]*
DIS1	$\longrightarrow$	3.6×10^{12}	0.041	[70, 75]
DIS2	$\longrightarrow$	1.5×10^{12}	0.694	[69]
DIS3	$\longrightarrow$	3.5×10^{12}	0.238	[74]
DIS4	$\longrightarrow$	1.2×10^{12}	1.513	[75]
DIFF1	$\longrightarrow$	5.4×10^{12}	1.904	[70, 72]

DIFF2		3.0×10^{11}	0.943	[75]
DIFF3		4.3×10^{12}	1.399	[72]
DIFF4		3.4×10^{13}	1.275	[72]
DIFF5		1.0×10^{13}	0.730	[76]
DIFF6		4.3×10^{12}	1.399	[72]*
DIFF7		5.4×10^{12}	1.904	[70, 72]*
DIFF8		1.0×10^{13}	0.730	[76]*
DIFF9		1.0×10^{13}	0.730	[76]*
DIFF10		1.0×10^{13}	0.730	[76]*
DIFF11		5.4×10^{12}	1.904	[70, 72]*
DIFF12		3.4×10^{13}	1.275	[72]*
DIFF13		5.4×10^{12}	1.904	[70, 72]*
DIFF14		3.4×10^{13}	1.275	[72]*

47

	Reaction	A	n	Ref.
DIFF15		5.4×10^{12}	1.904	[70, 72] *
DES1	− O$_2$	1.3×10^{14}	1.420	[75]
DES2	− O$_2$	6.4×10^{14}	1.104	[69, 74]
DES3	− O$_2$	1.0×10^{13}	1.130	[76]
OXzz1	− CO	1.2×10^{16}	3.622	[66, 72]
OXzz2	− CO	1.2×10^{16}	2.300	[66, 72]
OXzz3	− CO	1.2×10^{16}	2.300	[66, 72]
OXac1	− CO	1.0×10^{13}	2.743	[66]
OXac2	− CO	1.0×10^{13}	1.704	[66]
OXac3	− CO	1.0×10^{13}	1.829	[66]
OXac4	− CO	1.0×10^{13}	1.136	[66]
OXac5	− CO	1.0×10^{13}	2.743	[66]*

48

OXac6		- CO		1.0×10^{13}	1.704	[66]*
OXac7		- CO		1.0×10^{13}	1.704	[66]*
OXd1		- CO		1.0×10^{13}	2.170	[78]
OXd2		- CO		1.0×10^{13}	0.447	[78]
OXd3		- CO		1.0×10^{13}	1.227	[78]
OXd4		- CO		1.0×10^{13}	1.860	[78]
OXd5		- CO		1.0×10^{13}	1.860	[78]*
OXd6		- CO		1.0×10^{13}	1.704	[66]*
OXd7		- CO		1.0×10^{13}	1.829	[66]*

49

Chapter 5 Kinetic Monte Carlo (KMC)

In this chapter, some of the details of the implementation of the reaction setup and kinetic reaction mechanism are discussed. This is followed by an assessment of the statistical analysis that has to be performed to derive accurate results from stochastic KMC simulations.

5.1 Implementation

As mentioned previously, the computational code used in this study is Zacros [113, 114], which offers an efficient implementation of the KMC method based on Gillespie's stochastic simulation algorithm [104]. It uses a binary search tree structure for efficient bookkeeping of the possible elementary events and their inter-arrival times during the simulation, and it provides the possibility of having locally different activation energies for the same elementary process due to energetic interactions with surrounding adsorbates. Zacros has been developed and is used extensively for applications in heterogeneous catalysis. In such simulations, the catalyst is modelled as a substrate offering sites to adsorbates in a regular lattice configuration. This formalism is often referred to as a lattice-gas model, and it is used here for modelling the graphene sheet.

Figure 5.1 shows the lattice used to model graphene in this study. It consists of corner sites where the carbon atoms in the graphene sheet are located, and bridge sites where oxygen can adsorb and form epoxy adsorbates on the basal plane. The distance between carbon atoms in the lattice has been set to $1.42\,\text{Å}$. Furthermore, periodic boundary conditions are imposed in both in-plane directions. This lattice is defined in Zacros in the *simulation_input.dat* file. The size of the lattice used for all simulations is 102×59 unit cells, which corresponds to a graphene sheet spanning
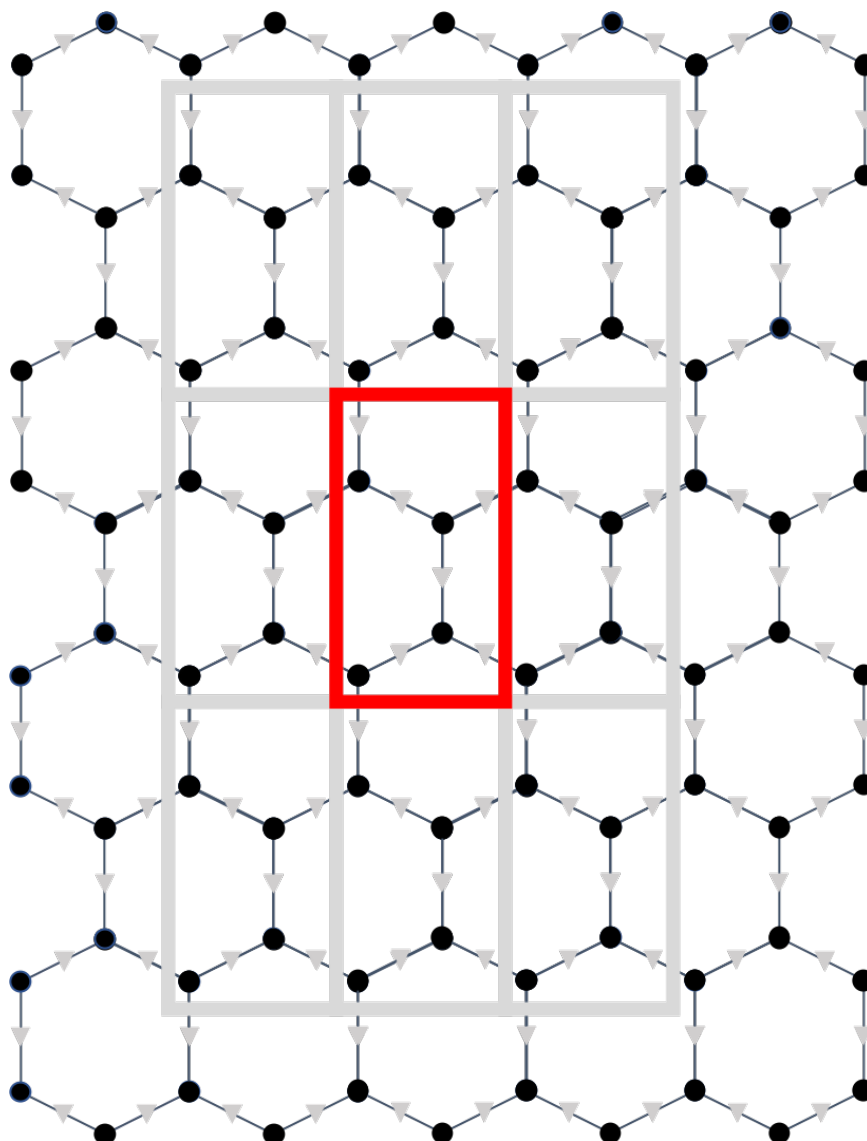
Figure 5.1: Lattice representing graphene with corner (circle) and bridge (triangle) sites. The corner sites are the locations where carbon atoms are located, the bridge sites are open for adsorption of oxygen in form of epoxies. The unit cell to build periodic geometries is also drawn.

an area of $25\,\mathrm{nm} \times 25\,\mathrm{nm}$. This corresponds to a total of 24072 carbon atoms in the simulation box.

The initial monovacancy defect that is used in this work as the seed for etch pits is located in the center of the graphene lattice, and is provided to Zacros in the *state_input.dat* file.

The implementation of the elementary reactions in the mechanism is mostly

straightforward, and is given to Zacros in the *mechanism_input.dat* file. However, one trick has to be applied here: While a substrate generally remains unchanged during catalysis, oxidation removes carbon atoms from the graphene sheet. Modern KMC codes normally do not provide the possibility of adapting the lattice dynamically through removal of sites. Instead, removed carbon sites have to be treated as species that are not interacting with any elementary process. Whenever a carbon atom is removed from an oxidation reaction, new edge sites are created, and they have to be categorized based on the local geometry. At the end of the *mechanism_input.dat* file, there is a set of 16 infinitely fast "reactions" which are denoted as EDGE1-16, that deliver this categorization of edge carbons during the simulation without interfering with the actual carbon oxidation process. This in turn now allows to track active sites and the geometry of defect lines in the simulation, from which pitting can be investigated.

Another trick that has been employed on the mechanism is rate constant rescaling [126] of fast diffusion reactions to improve computational performance. The rationale for this is fairly simple: Diffusion reactions tend to have low activation energies as compared to all other surface reactions in the mechanism, so they are the fastest category of processes. Hence, in the course of a simulation, most events performed will be diffusion events. The effect of fast diffusion reactions shows physically as smoothing out the different oxygen surface coverages, particularly on the basal plane. The large separation of timescales can now be shrunk as long as there is no noticeable effect on the slow dynamics, i.e. the surface coverages or even pit growth rate. While an automated feature for this exists in Zacros based on previously published schemes [127–129], rate constant have been manually rescaled for this work. The rescaled reactions are DIFF1, DIFF3-5, and DIFF11-15, with a reduction of the pre-exponential factor A by a factor of 10^4.

Two more simulation files have to be provided to Zacros by default. The *energet-*

ics_input.dat file provides the possibility of having locally different activation energies for the same elementary process due to energetic interactions with surrounding adsorbates. These interactions are however intrinsically part of the mechanism created in Chapter 4, and therefore the *energetics_input.dat* file doesn't contain any sort of energetic interactions for this study. The *simulation_input.dat* file is the main input to Zacros. All gas parameters are defined in that file. For this study, chemical equilibrium compositions for the O_2/O gas mixture have to be provided in molar fractions. Those have been previously calculated as a function of T and P using the widely used combustion code cantera (see [130] for an example program to calculate chemical equilibrium of a gas, with fixed T and P). Furthermore, all surface species that are used in the mechanism are defined in the *simulation_input.dat* file, together with all remaining simulation parameters such as the random seed for the pseudorandom number generator.

A sample of all Zacros simulation files described here is provided for a simulation at $T = 1000\,\mathrm{K}$ and $P = 1\,\mathrm{mbar}$ as supplementary files.

Recently, the Zacros developers have started to offer Zacros-post, a post-processing and visualization suite for KMC simulations performed with Zacros. For this work, an in-house suite for postprocessing and analyzing the KMC simulations has been developed in python.

One method worth noting that is employed in the postprocessing is the removal of artifacts inside the pit. Figure 5.2 demonstrates clearly what this means, and why it is important. The mechanism allows in some instance for the oxidation of carbon edge sites that cut off small carbon chains or artifacts inside the pit. When the pit is later analyzed on the basis of the carbon edge sites, those artifacts that remain inside the pit need to be sorted out, in order to get accurate results on the edge sites of that constitute the pit boundary only. Physically, it is somewhat questionable that longer carbon chains such as the one in Figure 5.2 (a) can actually
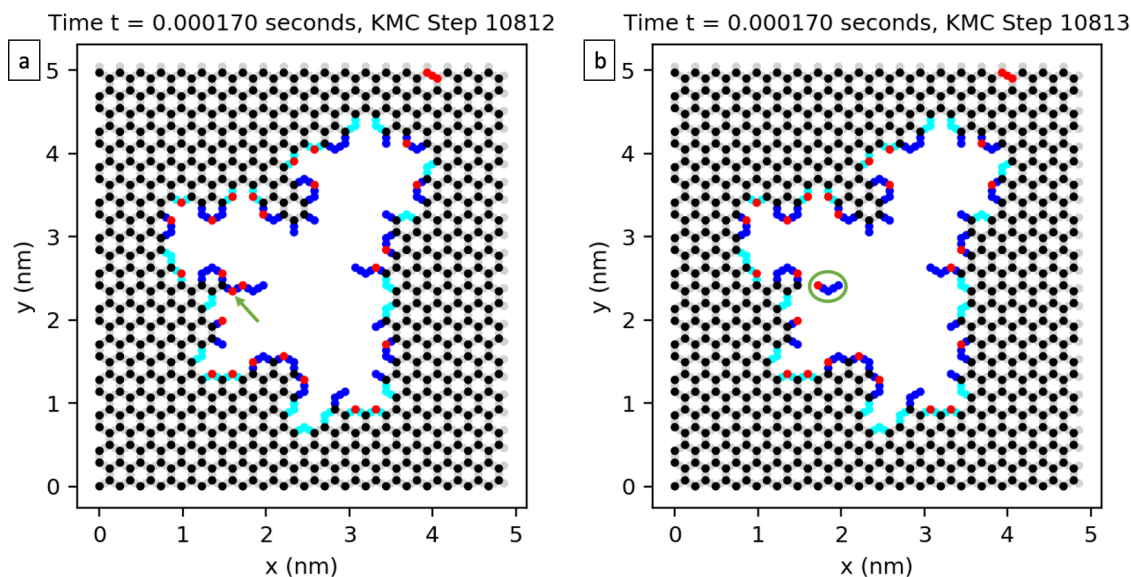
Figure 5.2: Two consecutive simulation steps demonstrating the removal of artifacts. In the first step (a), the semiquinone indicated with a green arrow is removed due to oxidation. In the second step (b), the artifact remaining inside the pit (green circle) is removed during postprocessing. For a description of the coloring of atoms, refer to Figure 6.1.

be stable. However, potential reconfiguration of such atoms is not straightforward, and capturing it within a lattice-based KMC approach is very difficult and would require a more or less complex mechanism on its own.

5.2 Statistical Analysis

In order to demonstrate the statistical analysis that is necessary to obtain accurate results from KMC simulations, a number of simulations have been performed early in this study, with a very simplified mechanism as described in [131]. A pristine graphene sheet was considered without any defects, such that the only processes that occur are dissociative adsorption of molecular oxygen to form two epoxies on the surface, and the recombinative desorption of two epoxies back to molecular oxygen in the gas phase. The result is a quickly established constant level of oxygen coverage (which is much higher than the basal plane coverages encountered later due to the simplified
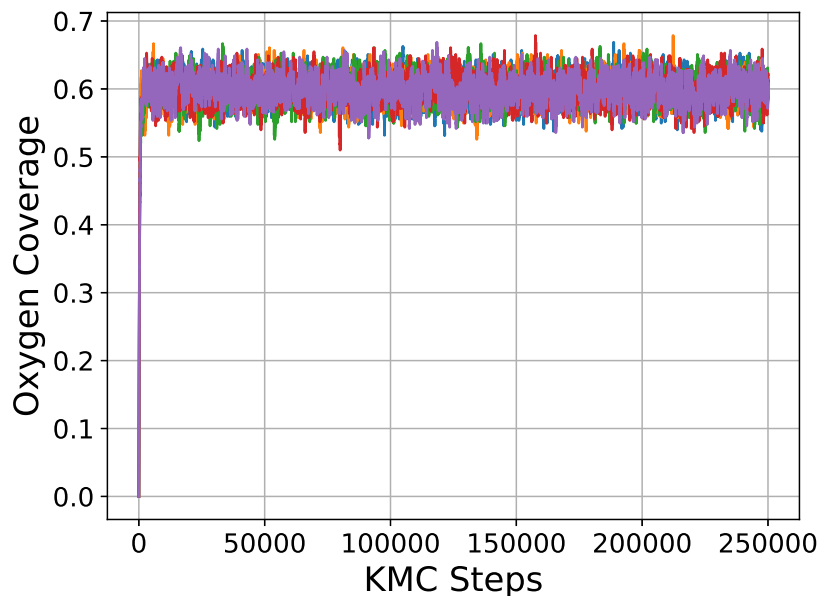
Figure 5.3: Sample trajectories for the evolution of oxygen coverage. The random seeds have been varied from 1 to 5.

nature of the mechanism here). Figure 5.3 shows the evolution of the oxygen coverage for five 5 different simulation trajectories. All simulation trajectories are run with the same parameters, except that the random seed is changed in order to generate a different sequence of random numbers in each trajectory. This demonstrates clearly the stochastic nature of KMC simulations.

The oxygen coverages in Figure 5.3 have similar forms, such that they quickly approach a steady state level and then continue to fluctuate around that steady state. This is also true for most of the results that are calculated from the full mechanism in Chapter 6. It is interesting that the magnitude of fluctuations stays constant throughout the simulations reported here. This is due to the fact that no carbon atoms are ever removed, so the oxygen coverage is always calculated on the same graphene sheet with a constant number of atoms. In the later simulations, the trend is often for the fluctuations to decrease in amplitude with growing pit size. This is particularly true for edge coverages, since the number of edge carbons monotonically
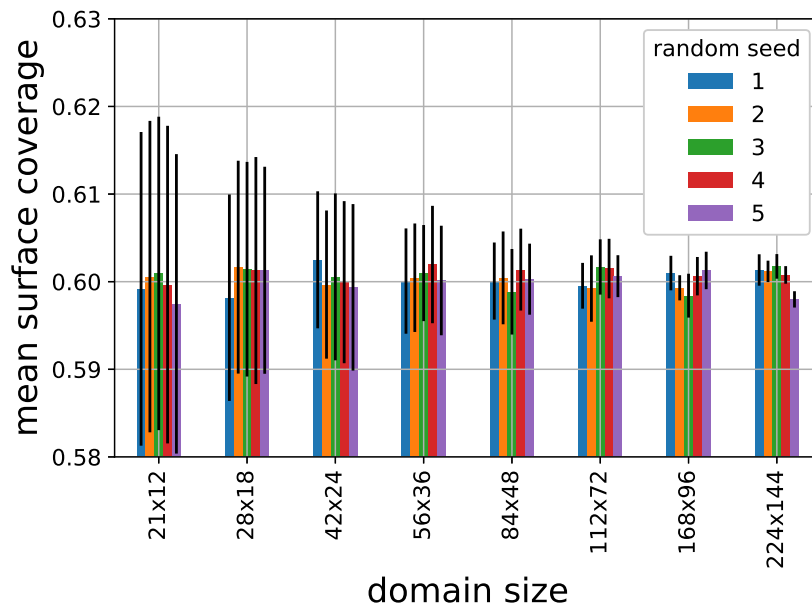
Figure 5.4: Dependence of the mean oxygen coverage and standard deviation (black bars) on size of the simulation domain in terms of unit cells. 5 different trajectories are displayed at each domain size.

increases and therefore delivers a more accurate basis for calculating the coverage. To further strengthen this argument, Figure 5.4 shows how the fluctuations in this simple system depends also on the domain size, i.e. the number of carbon atoms. As was discussed, the amplitude of the fluctuations keeps decreasing with an increasing number of carbon atoms.

However, notice in Figure 5.4 that although the fluctuations within each trajectory decrease in amplitude, the variance between the mean value of the steady state oxygen coverage remains essentially constant. This in turn shows that it is extremely important to sample multiple KMC simulation trajectories for the same parameters, in order to increase the accuracy of results like mean coverages. Obviously, the more trajectories are considered, the better the statistical accuracy, if as in this case the mean value between the results of all trajectories is taken.

Hence, for the simulations that follow, a reasonable balance has to be found between feasibility and statistical accuracy. For that purpose, a lattice size of 102×59

unit cells has been selected, and a total of 16 trajectories are performed for each set of parameters. Furthermore, simulations are always run until the pit reaches the boundary, to ensure the longest possible simulated times.

Chapter 6 Results

A detailed computational study of graphene etching and pitting of graphitic carbon surfaces is performed in this chapter. Section 6.1 considers a single typical KMC simulation in order to demonstrate the kinds of results that this novel computational study delivers. After that, in Section 6.2 pitting is assessed in detail on the basis of KMC simulations performed over a wide range of conditions, and the results are interpreted on the fundamental basis of the underlying kinetic mechanism.

6.1 Example Simulation Analysis

The selected representative simulation has been performed with conditions of $T = 1000\,\text{K}$ and $P = 1\,\text{mbar}$, and system parameters as described in the previous chapters. For reference, at these conditions, the molar fraction of atomic oxygen $X_\text{O} \approx 5 \times 10^{-9}$ is extremely low, so the gas is almost purely molecular oxygen.

To start with, Figure 6.1 shows the simulated pit at the end of the simulation run, where the pit has reached the boundary of the simulation box at the center left. The snapshot corresponds to a final physical time of $t_{final} \approx 1.457\,\text{s}$, which was reached after roughly 4.8 million KMC simulation steps. A video demonstrating the growth of the pit throughout the simulation is provided as supplementary material (Supplementary Video SV1). The coloring of the sites is explained in detail in the caption of Figure 6.1, and is kept consistent with all simulation snapshots and videos that are included in the remainder of this work.

The following subsections describe the information that can be gathered from this and all other simulations that are part of this study.
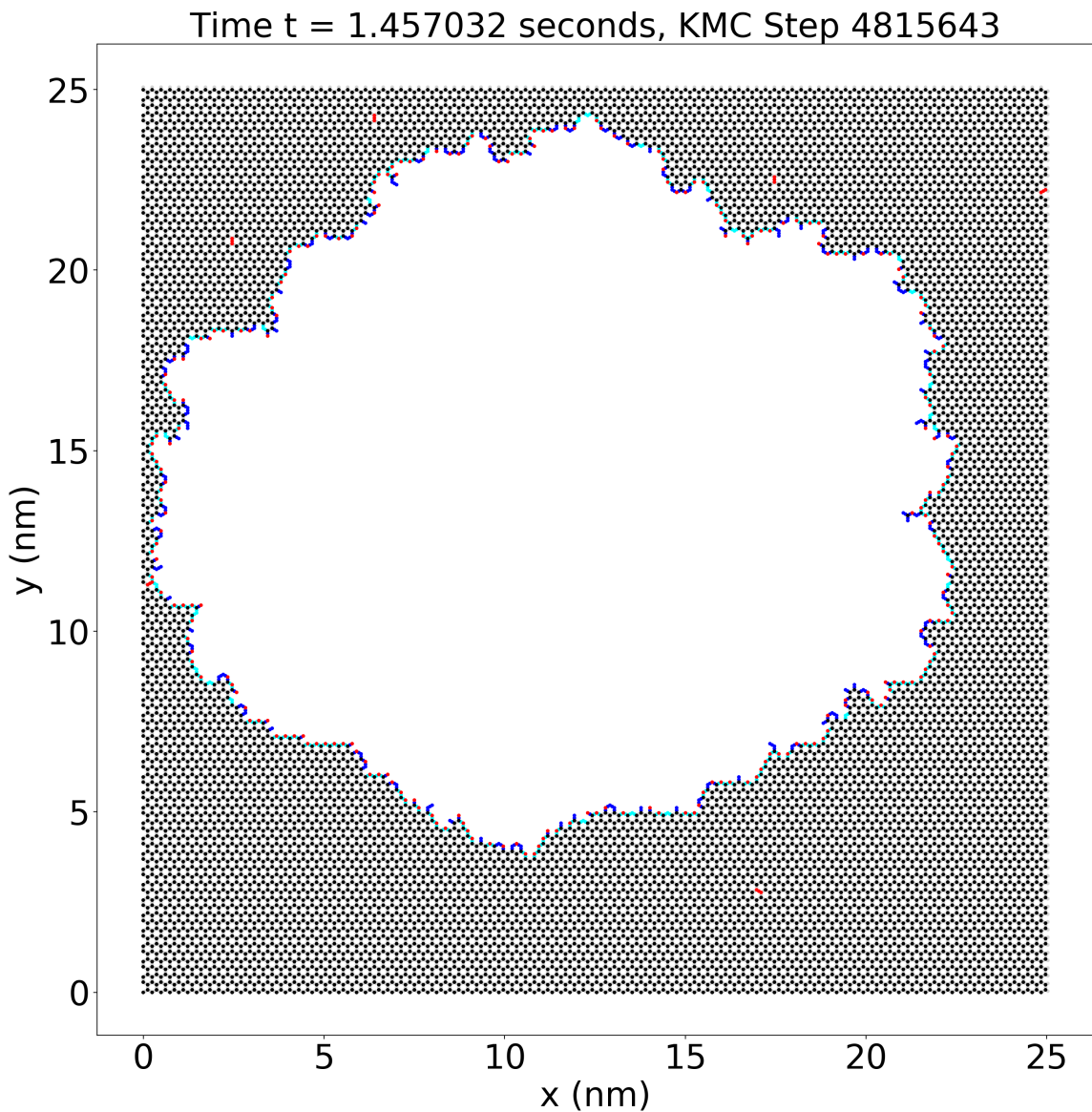
Figure 6.1: Simulation snapshot of etch pit at $T = 1000\,\mathrm{K}$ and $P = 1\,\mathrm{mbar}$. Basal carbon sites are colored in black, with the connecting bridge sites colored in grey. Zigzag edge sites and the connecting bridge sites are colored in bright blue, all other carbon and bridge edge sites are colored in dark blue (armchair and dangling). Sites with oxygen adsorbates are colored in red. On edge sites, only the carbon site where the oxygen is adsorbed is colored in red, while on the basal plane, both carbon sites and the connecting bridge site that compose the epoxide adsorbate are colored in red. A full video of this simulation is provided as Supplementary Video SV1.

6.1.1 Pit Radius and Growthrate

An obvious result of interest, that can be directly compared to experimental data for validation purposes, is the growth rate of the pit. To do that, the evolution of the pit radius $r(t)$ over time t needs to be considered. The pit radius $r(t)$ is calculated as the mean distance of all edge carbon sites to the location of the initial monovacancy, i.e. the center of the pit. If we denote the distance of edge carbon site i to the initial monovacancy as $d_{i,center}$, this writes as

$$r(t) = \frac{\sum_{i=1}^{N(t)} d_{i,center}}{N(t)},$$

where $N(t)$ is the total number of edge carbon sites at time t. For instance, at the beginning of each simulation, $N(t = 0) = 3$, because there are three zigzag carbon edge sites surrounding the monovacancy defect. All of them have the same distance to the monovacancy, namely the carbon-carbon bond length in graphene, such that $r(t = 0) = 0.142\,\text{nm}$. Note that instead of choosing the position of the initial monovacancy defect as the static center of the pit, the pit center could also be calculated at each step as the mean position of all carbon edge sites. For the calculation of the pit radius, this could be important if the position of the center of the pit undergoes meaningful changes during oxidation. However, as is demonstrated in Appendix A.3, for the example simulation considered in this section, which shows a shift of the pit center to the north west direction in Figure 6.1, the calculated radii only differ insignificantly.

Figure 6.2 shows the evolution of the pit radius in this example simulation. It is obvious that the pit doesn't immediately start to grow at a constant growth rate in time. In fact, for $t < 0.5\,\text{s}$, the pit barely grows at all. Notice that the initial radius $r(t = 0)$ is nonzero as was explained before. The pitting rate then speeds up considerably between $t = 0.5\,\text{s}$ to $t = 1\,\text{s}$, until it reaches the regime of constant pit growth rate at $t > 1\,\text{s}$. This initial transit phase from inhibited pit growth to
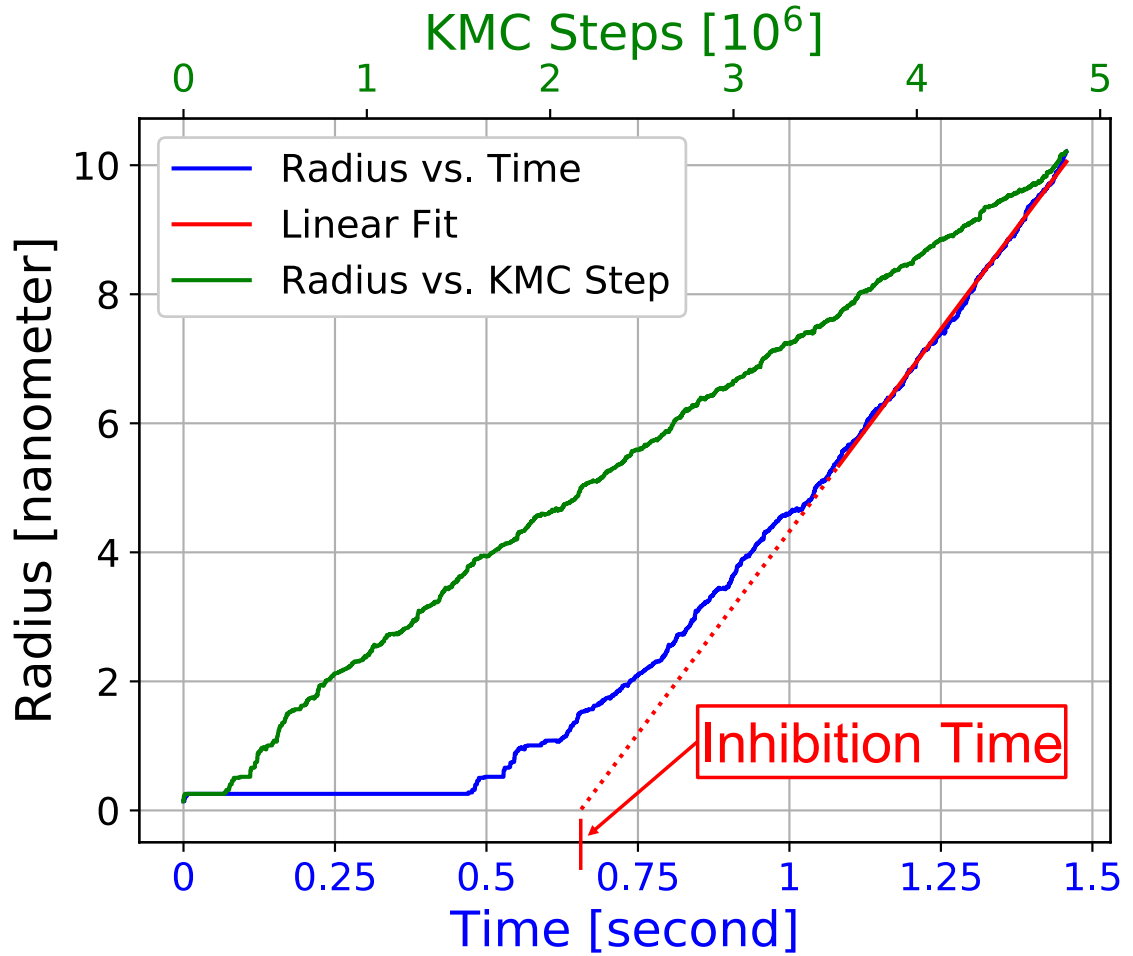
Figure 6.2: Pit radius evolution for a pit simulated at $T = 1000\,\mathrm{K}$ and $P = 1\,\mathrm{mbar}$, plotted against time (blue) and KMC simulation steps (green). Linear regression is applied to a late part of the time signal (red line, procedure explained in detail in text). The inhibition time for pit growth is found as the time where the continuation of the fit line reaches zero radius.

finally reaching the regime of constant pit growth rate is only rarely recognized in experimental studies due to reasons that will be discussed in Section 6.2.4. For now it is sufficient to acknowledge this as a real dynamic phenomenon present in pitting.

For later analysis purposes, there are now two quantities that can deduced from this graph, namely the pit growth rate in the regime of constant fast growth, as well as the inhibition time after which pitting enters the fast growth regime. The simulations generally show that the onset of fast pit growth is depending on the size

of the pit, and fast growth is reached at latest at a pit size of $r = 5$ nm. There will be a longer discussion on the underlying mechanistic reason for this later in this chapter. However, for now it is important to notice that simulations are carried out to pit sizes of roughly $r(t_{final}) = 10$ nm, so there is a long enough time spent in the fast growth regime. In fact, with respect to the KMC simulation steps, it can be seen that more than half of the simulation steps are performed in that regime, when $r > 5$ nm. This is found universally throughout all simulated conditions.

In order to accurately calculate the pit growth rate in an automated way, the following procedure has been developed: The pit growth rate is calculated as the slope of a least-square linear regression through the time evolution of $r(t)$ corresponding to the second half of each simulation based on the number of KMC steps. Looking at Figure 6.2, this linear fir corresponds to the solid red line, so it can be seen that taking the last half of the simulation in terms of KMC steps does not necessarily also correspond to the second half of the time evolution. In this particular case, it is less than the last third of the time signal. The R-squared value of those linear regression fits to the pit growth rate are no less than 0.95, and larger than 0.99 at most simulated conditions. This shows that this procedure of calculating the growth rate from simulations is generally very accurate.

The linear fit is furthermore utilized to infer the inhibition time. As it is shown in Figure 6.2, the fit curve can be extended to earlier times (dotted red line), where it intersects the time axis ($r = 0$) at some finite non-zero time $t_{intersect}$. This $t_{intersect}$ is directly taken as the inhibition time $t_{inhibition}$ for the pit growth. Note that $t_{inhibition}$ can appear negative in cases where pit growth more or less instantly sets in (high T, high P), as a result of the statistical nature of the fit. However, the magnitude of $t_{inhibition}$ in those cases is negligible and of no physical relevance, so that $t_{inhibition} = 0$ can safely be assigned for those cases. An example for such a case is provided in Appendix A.4.

6.1.2 Oxygen Surface Coverages

Another result of interest is the coverage of the graphene sheet with oxygen adsorbates. It is important here to differentiate directly between the basal plane and the edge, because those play different roles in the oxidation process. The coverages are calculated on a per site basis. This is one of the key advantages that this atomically resolved simulation approach offers, because all information about the carbon sites and adsorbates in system is accessible at all times. Taking for example the coverage of zigzag carbon edge sites $\theta_O^{zigzag}(t)$, it is calculated as

$$\theta_O^{zigzag}(t) = \frac{\text{number of zigzag carbon edge sites covered with oxygen}}{\text{total number of carbon zigzag edge sites}} .$$

This is similar for θ_O^{basal}, $\theta_O^{armchair}$ and $\theta_O^{dangling}$, with the number of basal, armchair and dangling sites respectively. Notice that $\theta_O^{zigzag}(t)$ is time dependent as the number of carbon sites of each type changes with pit growth, and the oxygen adsorbates are mobile due to diffusion, or can desorb altogether with or without removing carbon sites from the graphene sheet. In the case of θ_O^{edge}, the zigzag, armchair and dangling coverages are aggregated, such that

$$\theta_O^{edge}(t) = \frac{\text{number of all carbon edge sites combined, covered with oxygen}}{\text{total number of carbon edge sites}} .$$

Note that a single epoxide on the basal plane covers two carbon sites, which is intrinsically taken into account by calculating the coverage on the basis of carbon sites rather than adsorbed species. Similarly, if an edge site is covered with molecular oxygen, it is only counted as a single covered site.

Figure 6.3 show the evolution of all edge coverages with time, i.e. $\theta_O^{edge}(t)$, $\theta_O^{zigzag}(t)$, $\theta_O^{armchair}(t)$ and $\theta_O^{dangling}(t)$. Initially, when $t < 0.5\,\text{s}$, large fluctuations can be seen. This is due to the low number of carbon sites that go into the calculations of those quantities. However, as the pit begins to grow more rapidly at $t > 0.5\,\text{s}$, the coverages quickly converge to steady state with only small remaining

Figure 6.3: Time evolution of edge coverages. All coverages asymptotically approach a steady state coverage at late times where the pit has grown to a significant size.

fluctuations. Again, the reason for this behavior is simply due to the size of the pit and therefore the number of edge sites that are taken into account for calculating the coverage terms.

To quantify the edge coverages for later analysis, a procedure similar to the pit growth rate is followed. Again, only the second half of the simulation in terms of KMC steps is considered, i.e. the regime of fast pit growth at a constant rate. The difference is that instead of a least-square linear regression to the radius, a simple weighted average with time is performed in order to find the steady state values for the coverages. This holds for all different types of edge coverages, over all simulated conditions.

On the other hand, Figure 6.4 shows the time evolution of the basal plane coverage
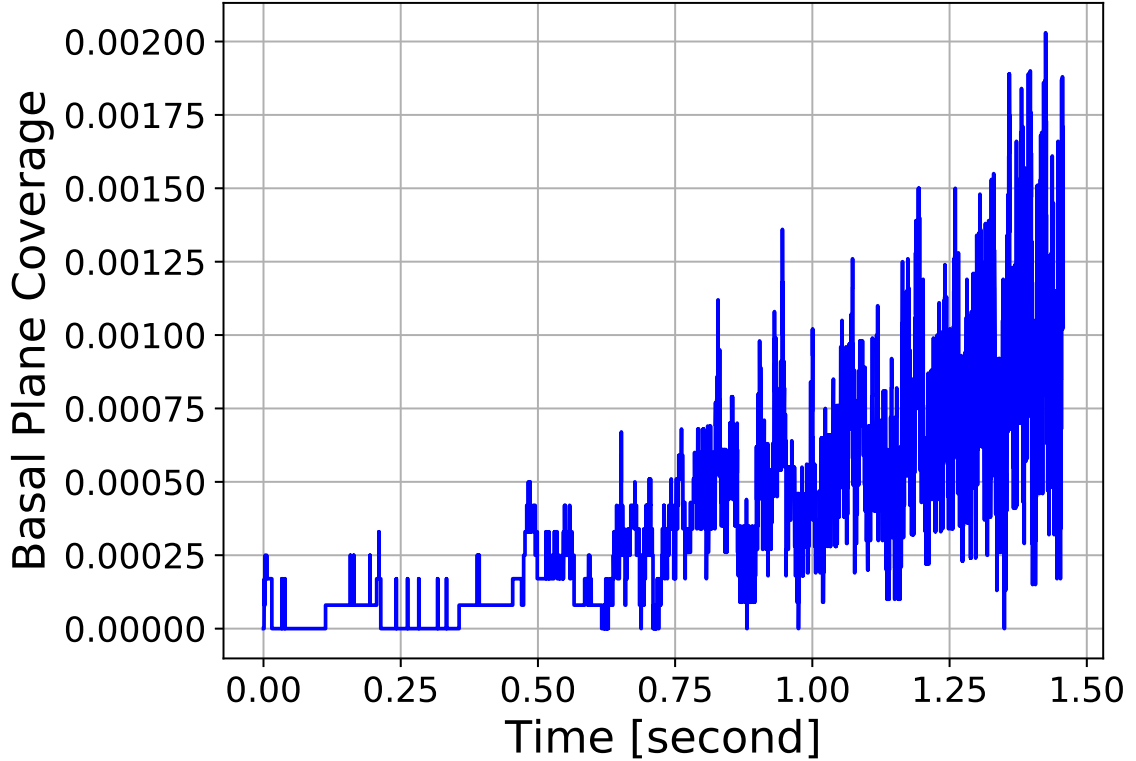
Figure 6.4: Time evolution of basal plane coverage. The coverage increases with time as the pit grows in size and more oxygen spills over from the edge to the basal plane.

$\theta_{\mathrm{O}}^{basal}(t)$. Clearly, it behaves much different to the edge coverages. First of all, notice that its magnitude is much smaller than that of the edge coverages. The reason for this is discussed later. From a dynamic perspective, it is interesting to note that $\theta_{\mathrm{O}}^{basal}(t)$ is increasing with time and therefore with the size of the pit. This indicates that spillover of adsorbed oxygen species from the highly covered edges to the basal plane is playing an important role, as will be seen later.

For later analysis, it is again important to find a single quantity to denote $\theta_{\mathrm{O}}^{basal}$. One straightforward way would be to use the basal plane coverage $\theta_{\mathrm{O}}^{basal}(t = t_{final})$ at the end of the simulation. However, since the fluctuations increase with increasing time, instead a weighted mean value is calculated similar to the procedure of calculating steady state values of edge coverages. While this is not ideal and somewhat undermines the dynamic nature of $\theta_{\mathrm{O}}^{basal}(t)$ in this particular case, it will be

seen that spillover effects are not significant across all conditions. For example, Appendix A.5 shows the basal plane coverage evolution at $T = 2000\,\mathrm{K}$ and $P = 1\,\mathrm{mbar}$, where a steady state is reached almost instantly. In the end, this procedure provides reasonably accurate data that proves itself useful in later analysis.

6.1.3 Carbon Edge Site Ratios (Edgeratios)

The composition of the edge in terms of it's individual types of edge sites is of interest in analyzing the pit geometry. Similarly to the oxygen coverages, these can be simply inferred by counting on a per site basis. For instance, the zigzag edgeratio $\gamma_{zigzag}(t)$ can be calculated as

$$\gamma_{zigzag}(t) = \frac{\text{number of zigzag carbon edge sites}}{\text{total number of carbon edge sites}}\;.$$

A similar calculation follows for the armchair edgeratio $\gamma_{armchair}(t)$ and dangling edgeratio $\gamma_{dangling}(t)$.

Figure 6.5 shows the evolution of those edgeratios with time. They show the same dynamic behavior as the edge coverages. Initially, before significant pitting occurs starts at $t = 0.5\,\mathrm{s}$, fluctuations are large. Interestingly, it can be seen that $\gamma_{zigzag}(t = 0) = 1$, because there are only three edge sites surrounding the initial monovacancy, and they are all zigzag sites. Then, as the pit grows larger, more sites are taken into account in their calculation, which decreases the magnitude of the fluctuations and converges the edgeratios to a steady state.

Again, the corresponding steady state values are calculated from a weighted average of the second half of the simulation, as is the case with the coverages. These are utilized as a quantitative measure for determining pit geometries in later analysis.

6.1.4 Gas Production and Consumption

It is interesting to consider how pitting actually consumes oxygen from the gas phase and in return releases CO as an oxidation product. Figure 6.6 shows the time evo-
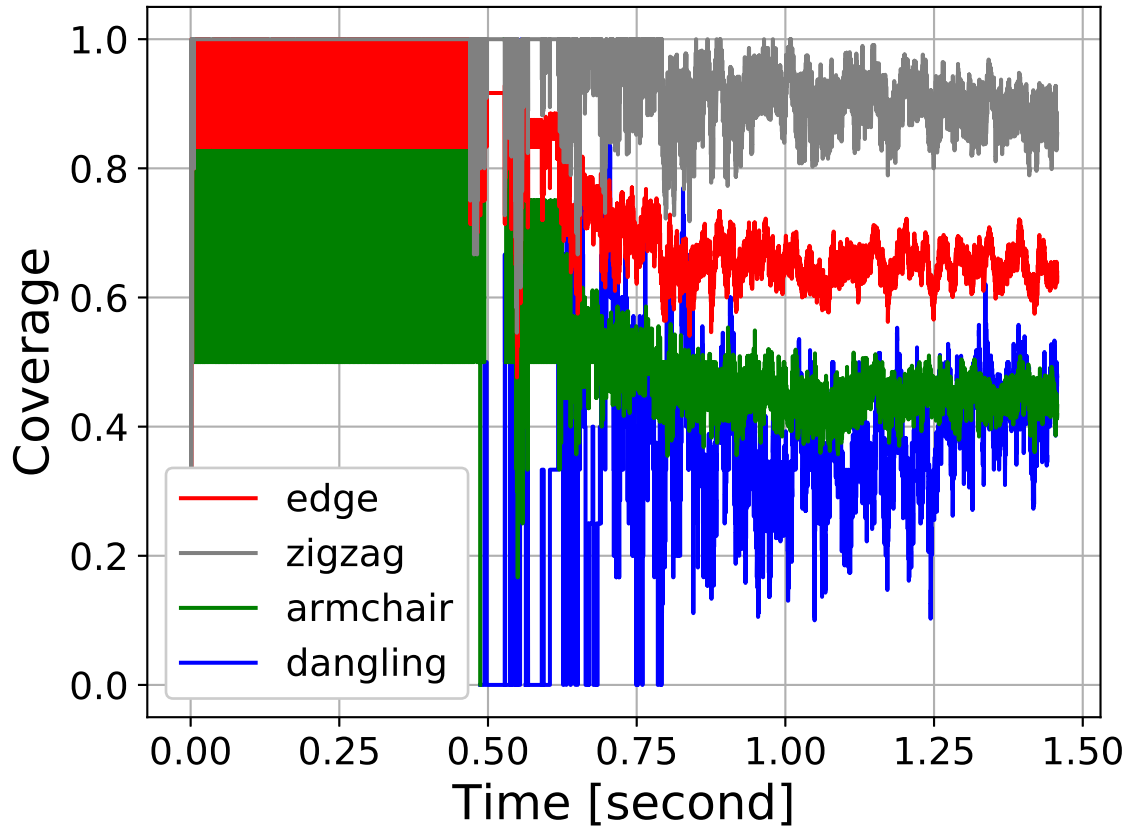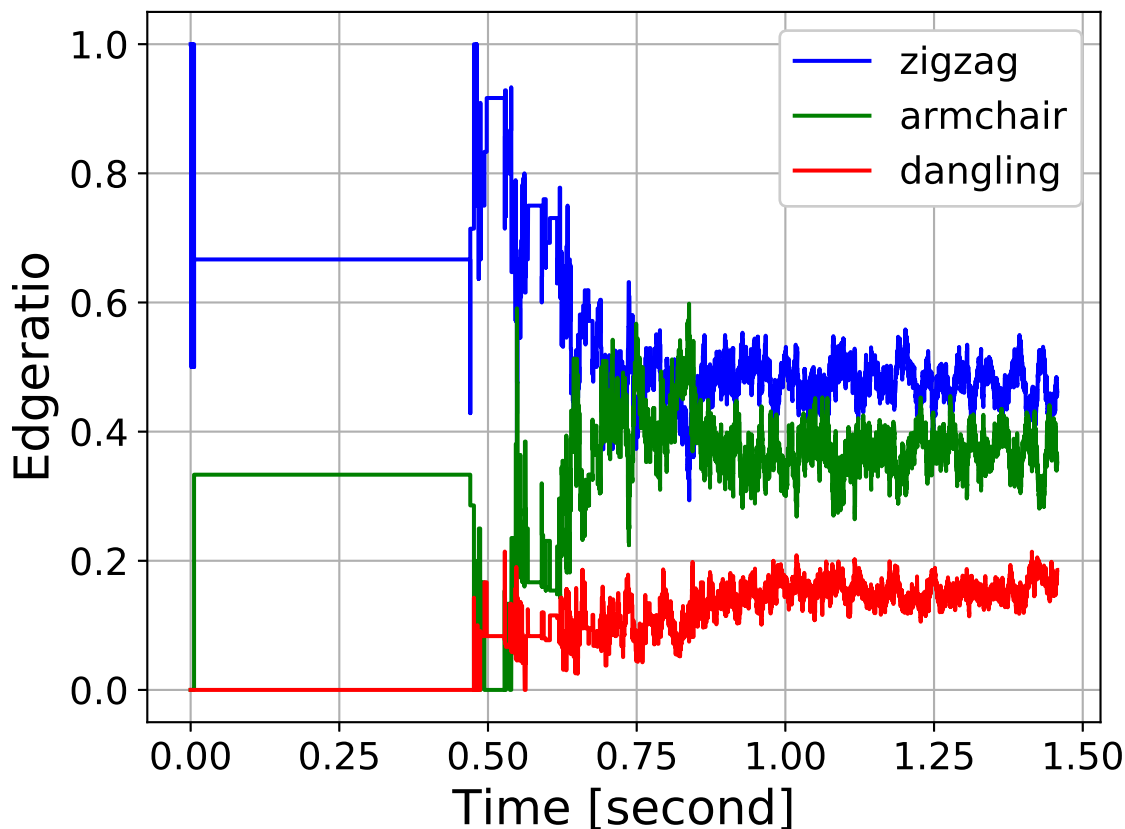
Figure 6.5: Time evolution of edgeratios. All edgeratios asymptotically approach a steady state coverage at late times where the pit has grown to a significant size.

lution of the net number of species that have been produced or consumed from the graphene sheet. First, notice that negative numbers denote species consumption, whereas positive numbers denote species production. Clearly, the production of CO seems to be balanced with the consumption of O_2, while O doesn't show a significant change. The behavior of atomic oxygen can simply be explained from the fact that at the simulated conditions the molar fraction of atomic oxygen $X_O \approx 5 \times 10^{-9}$ is vanishingly small. Hence, most oxygen that is turned into CO comes from molecular oxygen. In fact, the number of CO species is nearly twice as large as the number of O_2 consumed. There is however a small remaining difference in that balance, namely the oxygen adsorbates that remain on the graphene surface. Note that under different conditions, significant amounts of O can be consumed and even produce a net gain in
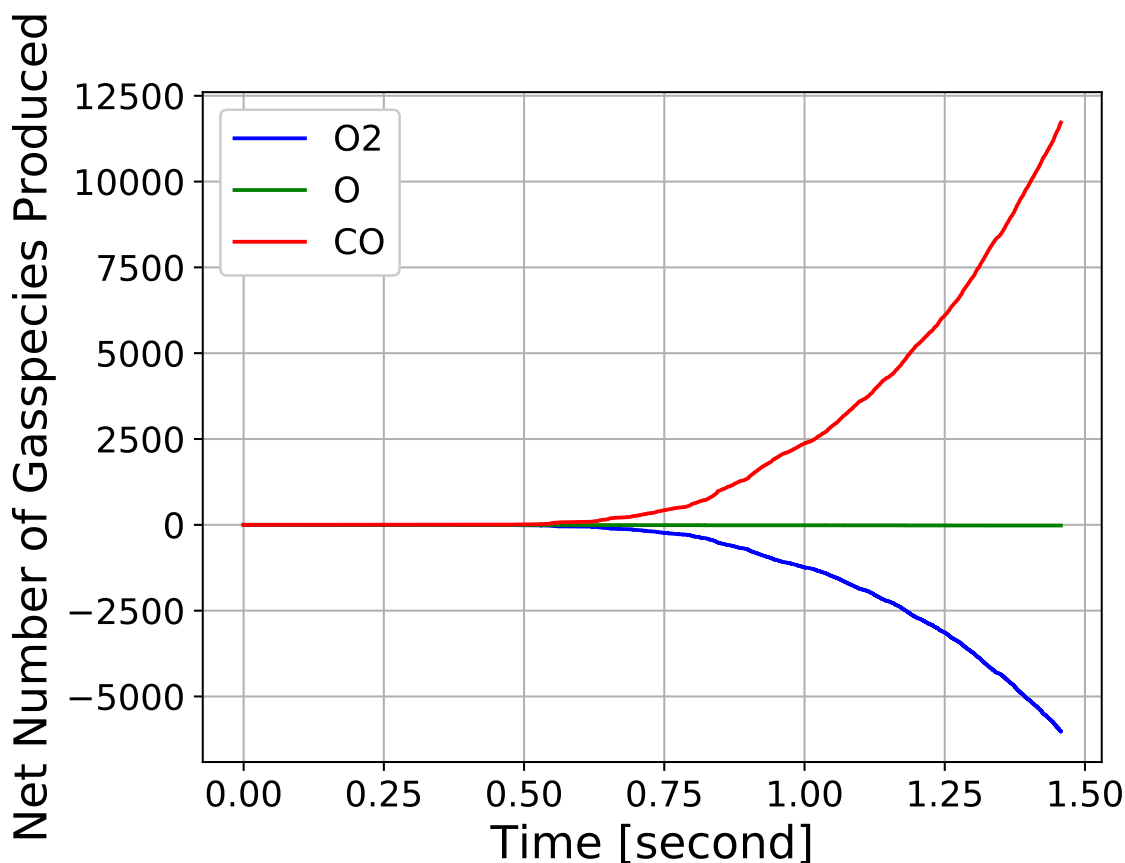
Figure 6.6: Gas species evolution: net number of molecular and atomic oxygen consumed, and carbon monoxide produced as a function of time.

O_2. Yet even more interestingly, cases exist where initially atomic oxygen produces a net in O_2, which eventually gets turned into a net consumption again by faster consumption due to a larger pit size (see Appendix A.6).

Considering the shape of the CO evolution, it clearly follows an exponential growth. In fact, it is roughly quadratic. This is because the production of CO directly correlates with pit growth. As has been shown in Figure 6.2, the pit grows linearly in time with a constant rate. This in turn means that the area of the pit grows roughly quadratically, assuming a circular pit shape. The production of each CO species through oxidation increases the pit area by an equal amount. This incremental area is basically the surface area of a single carbon atom in the graphene sheet, which equals about $2.6199\,\text{Å}$. Hence, the quadratic growth of the CO production is

a consequence of linear pit growth.

This is an interesting thought to bare in mind, considering that usually carbon materials have somewhat constant macroscopic oxidation rates at otherwise constant conditions. Obviously, pitting cannot directly yield an explanation for this. Hence, mesoscopic models will likely need to be developed to predict macroscopic reaction rates from first principles.

6.2 Pitting Results

Before discussing the results with respect to the dynamics and geometry of pitting, it is instructive to consider the coverages, as they provide a strong basis for understanding those results.

6.2.1 Surface Coverage

Figure 6.7 shows the basal plane oxygen coverage θ_O^{basal} and edge oxygen coverage θ_O^{edge} as a function of both temperature and pressure. The first thing to notice is that the basal plane coverage is extremely small (below one percent at almost all conditions), whereas the edge is nearly fully covered at low temperatures, and starts to free up with increasing temperature. The coverage is obviously a result of the balance between processes that produce adsorbates, such as adsorption and diffusion, and ones that remove adsorbates, such as desorption and oxidation.

Origin of Epoxide Adsorbates   In order to understand the basal plane coverage, Figure 6.8 gives an overview of the processes from which epoxide adsorbates originate. Figure 6.8 (a) shows that the dissociative adsorption of molecular oxygen on the basal plane is only contributing significantly at high pressures. This is obviously due to the adsorption rate being directly proportional to the pressure, and the activation energy of this process being fairly high. In contrast, adsorption of atomic oxygen,
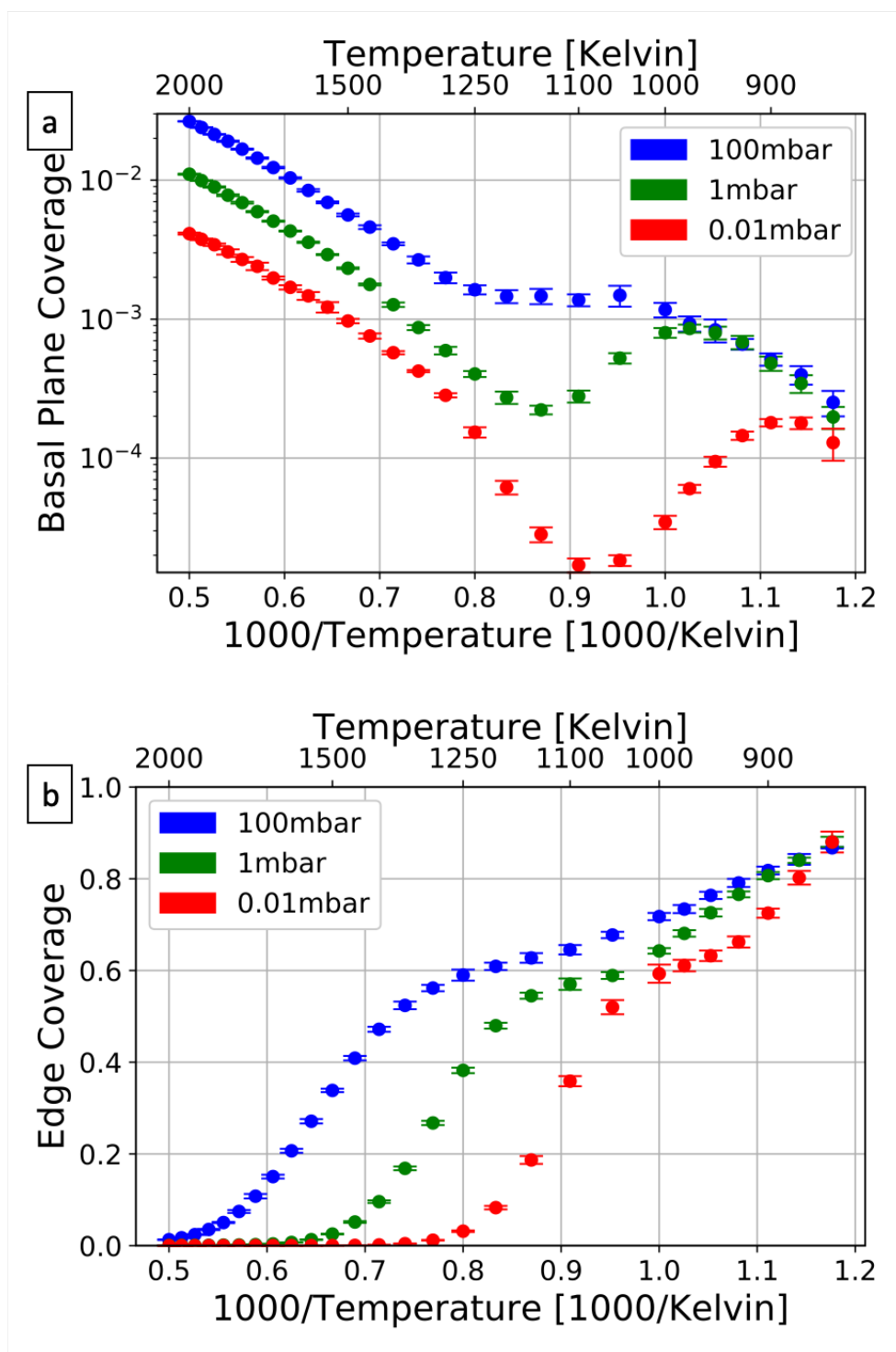
Figure 6.7: Oxygen coverage of the basal plane (a) and edge sites (b) as functions of temperature and pressure. The errorbars correspond to the standard deviation between all simulated trajectories for each case.

which is shown in Figure 6.8 (b), occurs without an energy barrier. However, the amount of atomic oxygen in chemical equilibrium is so low that this process never occurs at low temperatures. At higher temperatures, the mass fraction of atomic oxygen increases, and this type of adsorption quickly takes a dominating role. Lastly, Figure 6.8 (c), shows the role of the spillover mechanism. At low pressures and low temperatures, spillover is clearly the dominant epoxide forming process. Notice that the non-monotonic behavior of molecular oxygen adsorption in Figure 6.8(a) is caused by the onset of atomic oxygen adsorption at relatively higher temperatures as compared to the decrease in spillover.

Linking this back to the basal plane coverage in Figure 6.7 (a), it is clear that the coverage is close to zero at low temperatures, since the only processes occurring are spillover (or dissociative adsorption at high pressure), which are very slow due to their high activation energies. Any epoxide species produced in that regime get quickly consumed either in an oxidation or desorption reaction. With increasing temperature, the small increase in θ_O^{basal} can be attested to the spillover reactions, which then start to rapidly decline between $1000\,\mathrm{K}$-$1150\,\mathrm{K}$, causing the rapid decrease to intermediate minima in θ_O^{basal}. Only after atomic oxygen becomes more important at temperatures higher than $1100\,\mathrm{K}$ does the basal plane coverage increase sharply with increasing temperature.

Edge Coverage The edge coverage has a clear tendency to decrease from high coverage at low temperatures to zero coverage at high temperatures, irrespective of the pressure. This trend even holds when considering distinctly the coverages of zigzag, armchair and dangling edge carbons, as it is shown in Figure 6.9.

The reason for this universal behavior is simple. As long as oxidation reactions are slow compared to adsorption, the carbon edges are almost fully covered with oxygen. This stems from the close to barrierless adsorption on edge sites, which even
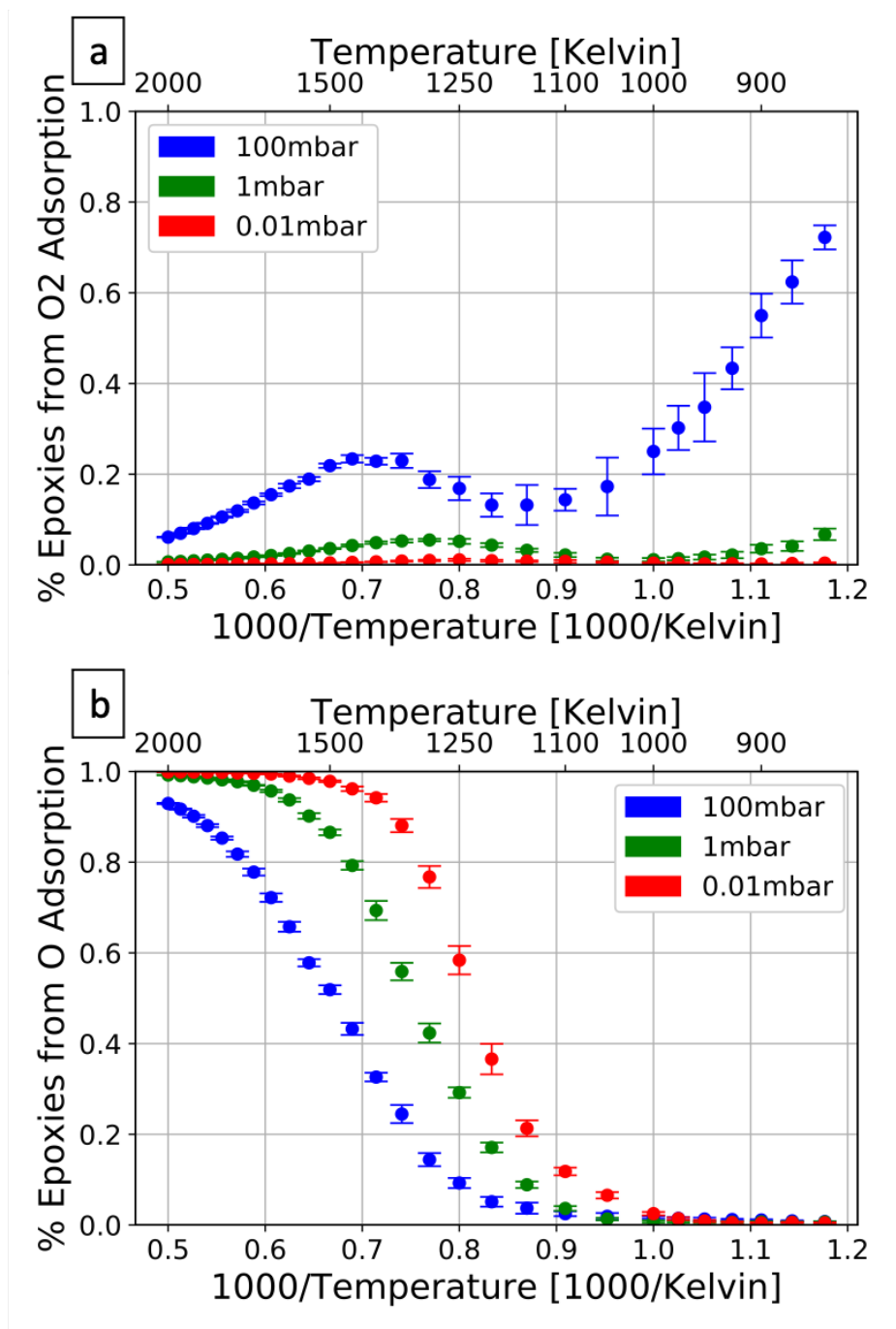
Figure 6.8: (Continued on the following page.)
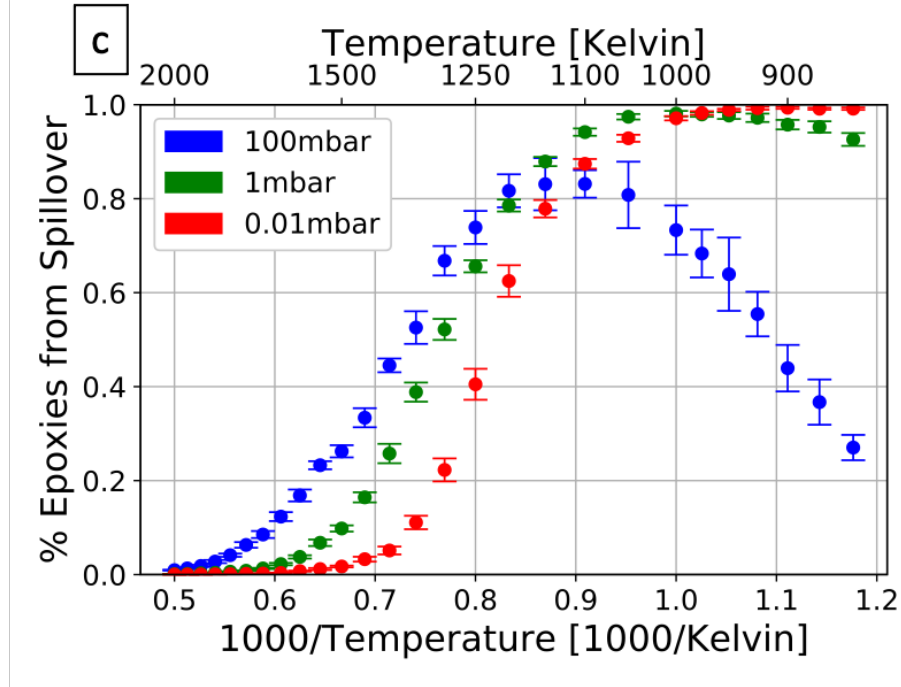
Figure 6.8: Ratios of basal plane oxygen produced from O_2 adsorption (a), O adsorption (b) and spillover (c) as functions of temperature and pressure. The sum of all three ratios (a,b,c) equals one. The errorbars correspond to the standard deviation between all simulated trajectories for each case.

ensures fast adsorption at low pressures. Increasing temperatures disproportionately accelerates oxidation reactions, which eventually depletes oxygen from edge carbons faster than they can arrive at the edge.

The intermediate plateau suggests that there is a shift in the dominant type of oxidation reactions at around 1000 K-1100 K.

6.2.2 Pit Growth Rate

Enough background knowledge has been collected to consider now the actual pit growth rates. Figure Figure 6.10 shows these as a function of temperature for different pressures. As was the case with all the coverages reported above, the errorbars show the variability of the etchrate between different simulated trajectories, which is a result of the probabilistic nature of KMC. It is fair to say that these errors that stem from the stochastic nature of KMC are generally negligible.

73
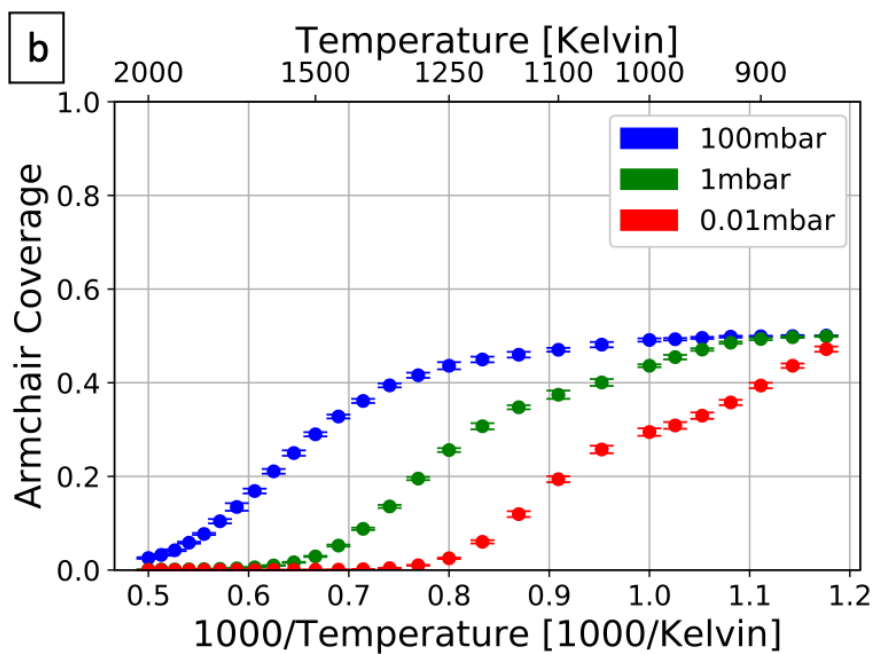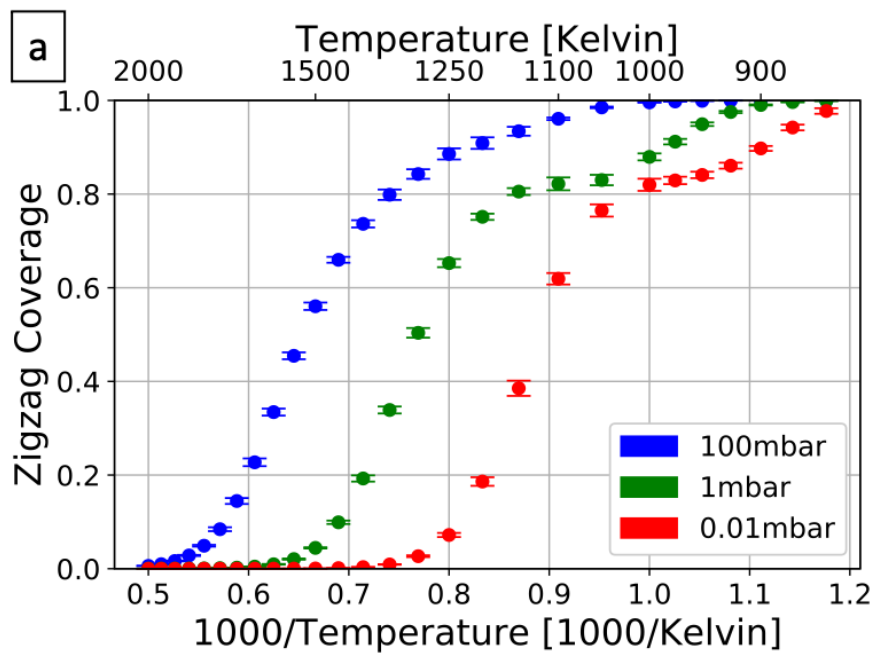
Figure 6.9: (Continued on the following page.)
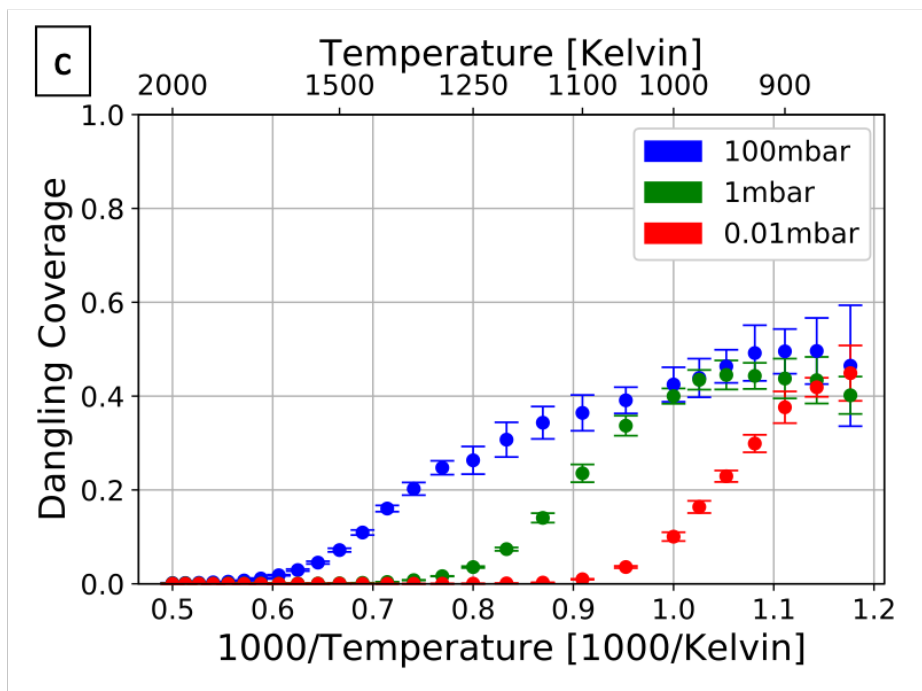
Figure 6.9: Oxygen coverage of zigzag (a), armchair (b) and dangling edge sites (c) as functions of temperature and pressure. The errorbars correspond to the standard deviation between all simulated trajectories for each case.

The simulated growth rates compare only moderately well with experimental results. Obviously, the qualitative trends of increasing growth rates with higher temperature and pressure are fully captured. However, on a quantitative level there are regions with varying degree of agreement. Generally, the simulated rates overpredict the experimental rates. It seems that at higher temperatures, KMC produces rates that are at least on the same order of magnitude, which is great agreement considering that the kinetic mechanism has not undergone any fine tuning within the inherent uncertainty limit of DFT derived reaction rates. This point is discussed in more detail in Section 7.3. However, the weak agreement at lower temperatures is a point for concern. In the worst case (low T and low P), the simulated growth rate differs from experimental rates by up to two orders of magnitude. It is not clear weather such a large margin can be resolved purely by tweaking reaction rates, or if the mechanism itself is not accurate enough at those conditions. It should be
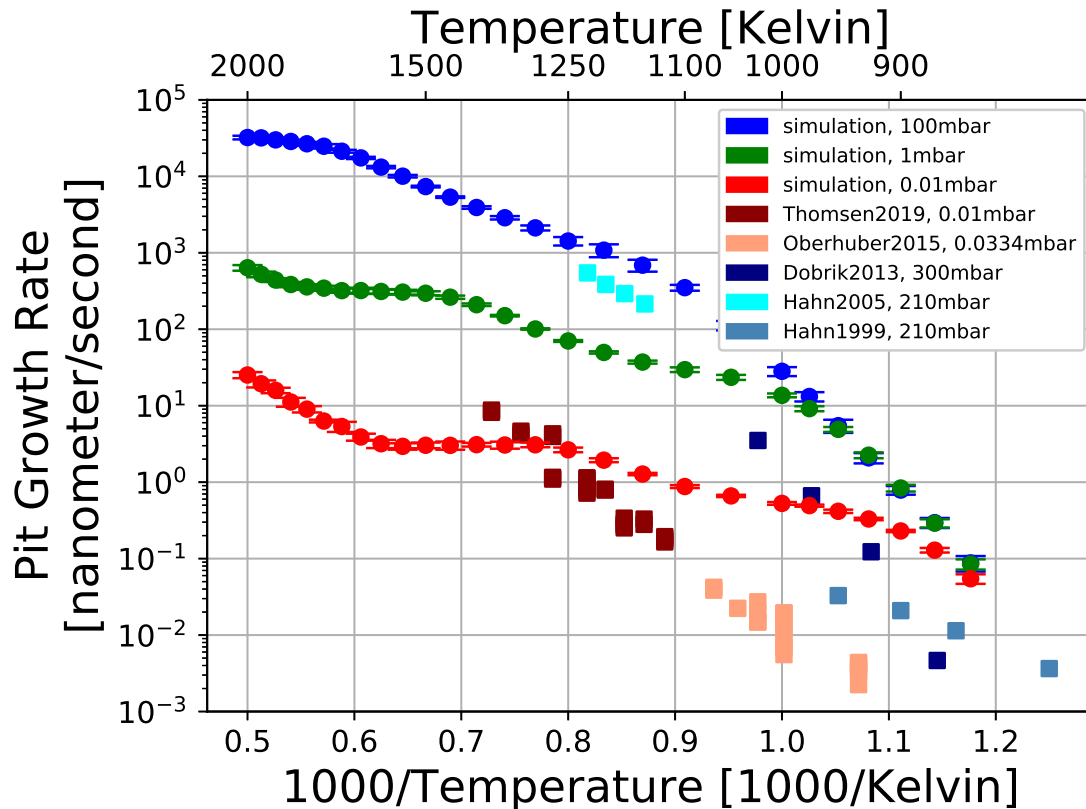
Figure 6.10: Pit growth rates as a function of temperature and pressure. The error-bars correspond to the standard deviation between all simulated trajectories for each case. Experimental pit growth rates are included with squared boxes. The reference keys are Thomsen2019 [18], Oberhuber2015 [132], Dobrik2013 [88], Hahn2005 [43], Hahn1999 [60].

noted however, that experimental results themselves show considerable variance in those regimes (see Dobrik2013 vs. Hahn1999 in Figure 6.10). Besides, due to the Arrhenius dependence of the intrinsic rates of elementary reactions on temperature, uncertainties in either the pre-exponential factors or activation energies have a more pronounced effect at lower temperatures, which may explain why the discrepancies are larger at low temperatures.

Clearly, more work needs to be done on this issue both from a experimental perspective, as well as from the viewpoint of this study. It can be hoped that the addition of this computational study in this context facilitates a better assessment

of the experimental data itself. Nevertheless, the fact that this first attempt on simulating actual pitting rates already produces moderately reasonable quantitative results shows the validity of the computational approach and motivates refinement of this computational study in the future. To the authors best knowledge, this is the first time that graphene etching has been simulated in long enough timescales to calculate those rates, with a comprehensive mechanism based on first principles.

Now follows a discussion of the simulated pitting rates on the basis of the kinetic mechanism. Looking at Figure 6.10, it can be seen that at the low temperature end, the etchrate is completely independent of pressure. Furthermore, the edge coverage in those conditions is very high. This clearly indicates that graphene etching is rate limited by the elementary oxidation reactions in this regime. Even at the lowest pressure, transport of oxygen to the edge through adsorption reactions is much faster than oxidation reactions, which causes the edge oxygen coverage to stay high.

Considering now the temperature increase up to around 1100 K, two notable things stand out. First of, the rate at which the pit growth rate increases with temperature quickly drops off at the low pressure already at temperatures below 900 K, whereas the intermediate pressure starts to fall off at 950 K. This coincides with a drop in the edge coverage, and can be particularly well seen in Figure 6.9 (a) for the zigzag coverage. Obviously, this behavior is dictated by the relative rate of adsorption reactions to oxidation reactions. Oxidation reaction have much larger activation energies as adsorption reactions on edge carbon sites. Hence, they speed up much faster with an increase in temperature. The drop off from the regime where graphene etching is purely rate limited by oxidation reactions is therefore dependent on both the pressure and temperature. The higher the pressure, the higher a temperature it takes for oxidation reactions to compete in speed with adsorption reactions on the edge. Furthermore, the negative slope that is observed in Figure 6.10 gives an indication to which type of elementary oxidation reaction is actually rate limiting. Looking

back at the mechanism itself, one can see that oxidation events on zigzag edges tend to have the highest activation energy, ranging from $3.622\,\text{eV}$ (OXzz1) to $2.3\,\text{eV}$ (OXzz2,OXzz3). The difference comes from the possible reduction of activation energy due to nearby epoxies on the basal plane. From the high pressure curve, a linear regression through the temperature range $T = 850\,\text{K} - 1000\,\text{K}$ returns an activation energy of roughly $2.8\,\text{eV}$. This clearly demonstrates that zigzag oxidation events are the rate limiting factor. Figure 6.11 confirms this, since only a small percentage of all oxidation events at low temperatures and pressures are zigzag oxidation events. Furthermore, Figure 6.12 shows that most oxidation events in this regime are sped up through nearby oxygen, which explains the intermediate apparent activation energy of $2.8\,\text{eV}$.

In the temperature range $T = 1100\,\text{K} - 1250\,\text{K}$, the pit growth rates show the same qualitative temperature trend. The slope is significantly lower than in the low temperature regime, which shows that zigzag oxidation reactions are no longer solely rate limiting. Clearly, there is now a large dependence on the pressure, which stems from the adsorption reactions.

Looking at the low pressure curve, there is a constant pit growth rate observed between $1250\,\text{K}$ and $1600\,\text{K}$. Similarly, such a regime of constant pit growth rates is present in the intermediate pressure curve, ranging from $T = 1500\,\text{K} - 1750\,\text{K}$. In those parameter regimes, graphene etching is truly rate limited by adsorption of oxygen on the edge. Those adsorption reactions are approximately barrierless, which explains the constant pit growth rate. In contrast, the oxidation reactions have much higher activation energies. However, the temperature is high enough that the resulting reaction probability is high. This behavior is seemingly not encountered in the high pressure curve, since the rates of adsorption reactions, which are directly proportional with the pressure, are still fast enough to compete with oxidation.

Finally, the speed up of the pit growth rate at the high temperature end is caused
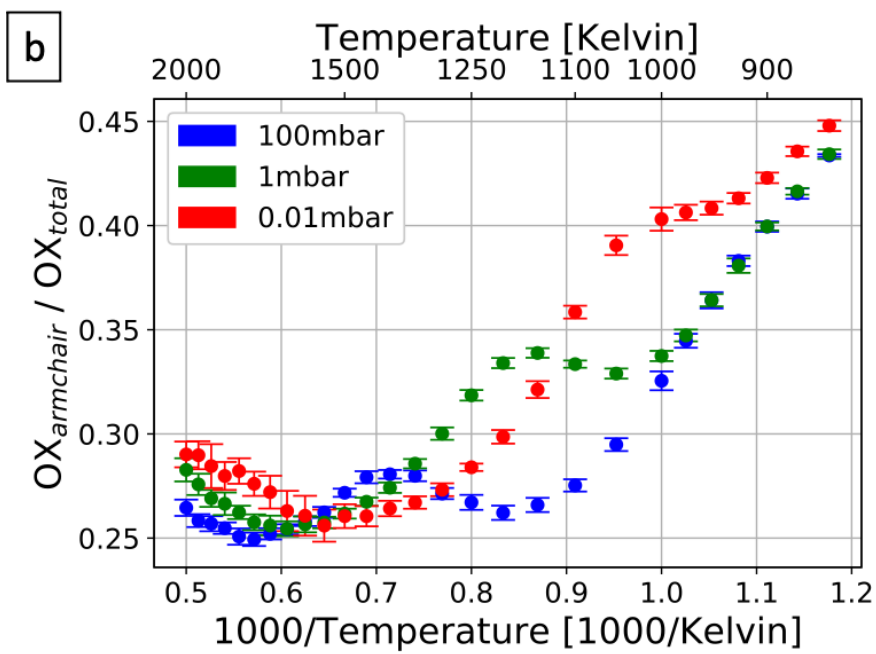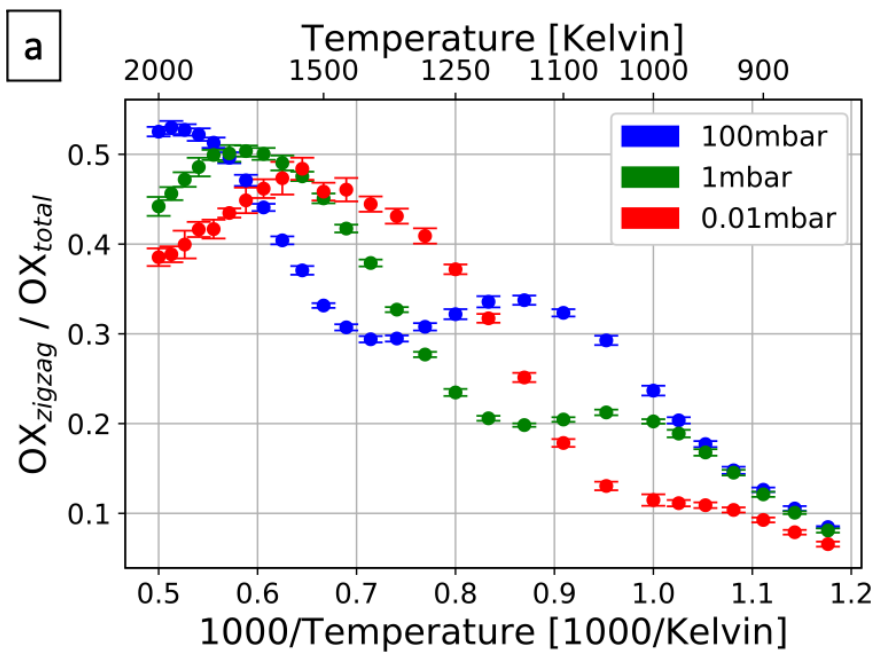
Figure 6.11: (Continued on the following page.)
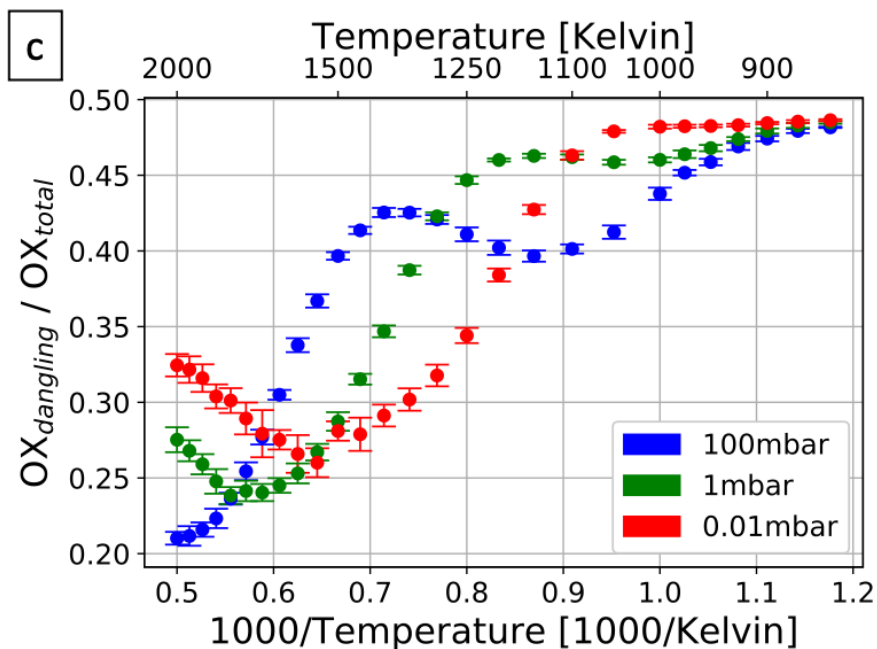
Figure 6.11: Ratios of zigzag (a), armchair (b) and dangling (c) oxidation events performed as functions of temperature and pressure. The errorbars correspond to the standard deviation between all simulated trajectories for each case.

by the increased presence of atomic oxygen. It can be seen in Figure 6.7 that while the edge coverage is now approaching zero for all pressures due to faster and faster oxidation, the basal plane coverage starts to noticeably increase. Hence, epoxies that are formed over the vast surface of the graphene sheet are now able to diffuse to edge carbons, where they are quickly removed via fast oxidation.

6.2.3 Pit Geometry

Figure 6.13 shows the zigzag edgeratio γ_{zigzag} as a function of both temperature and pressure. Furthermore, Figure 6.14 shows two simulated etch pits at conditions relating to hexagonal pit growth (a) and circular pit growth (b). Videos showing the full growth of these simulated etch pits are provided in the supplementary material (Supplementary Videos SV1 and SV2). First of all, notice that the edges around the hexagonal pit are almost all zigzag edges. This can also be directly seen in Figure 6.13,
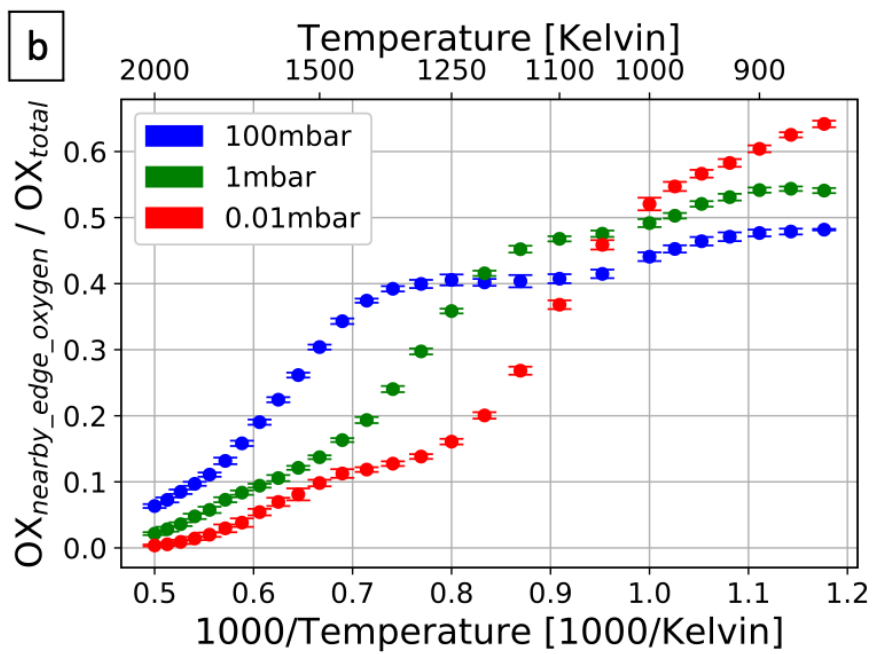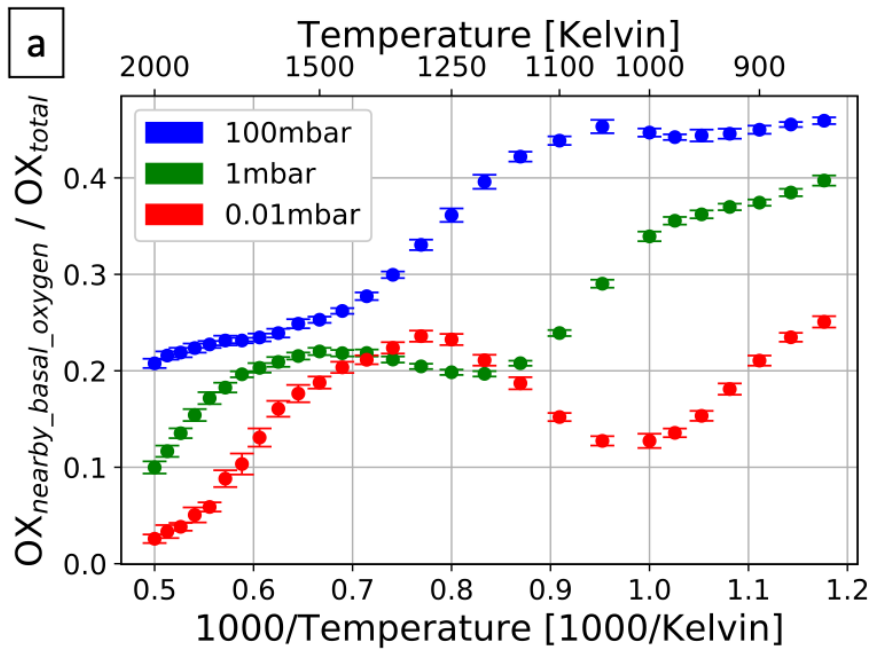
Figure 6.12: (Continued on the following page.)
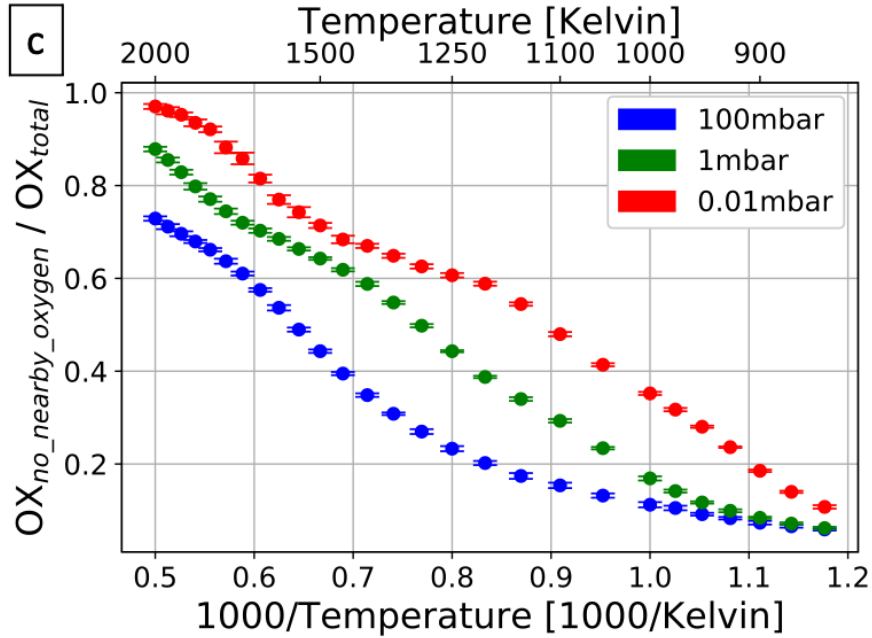
Figure 6.12: Ratios of oxidation events performed with nearby oxygen on the basal plane (a), nearby oxygen on the edge (b) and without nearby oxygen (c) as functions of temperature and pressure. The errorbars correspond to the standard deviation between all simulated trajectories for each case.

where γ_{zigzag} is very high at low temperatures and pressures. In contrast, the circular pit has a very irregular edge, where all edge carbon types are present at roughly equal amounts. Notice that when pits are observed to be circular (or cylindrical) on the macroscale of experiments, the irregularity or roughness along the edge is present, but likely too small to be visually detectable, such that the edge can actually appear to be smooth. However, in the context of graphene nanoribbons, smoothness of graphene edges is required at the atomic level, and this can only be found in hexagonal pits.

From Figure 6.13, it is obvious that pits tend to become circular with increasing temperature. Furthermore, at a constant temperature below 1100 K, an increase in pressure also leads to lower zigzag edgeratio and therefore circular pits. Qualitatively, this is in agreement with the two experiments presented in Section 2.2. Thomsen et al. [18] have observed a pressure dependent transition from hexagonal to circular pits at a constant temperature of 1073 K. The pressure transition was observed in the range

Figure 6.13: Zigzag edgeratio as a function of temperature and pressure. The error-bars correspond to the standard deviation between all simulated trajectories for each case.

of 0.055 mbar-6 mbar Delehouzé et al. [19] have reported a temperature dependent transition at a constant oxygen pressure of 1.4 mbar. The temperature transition was observed in the range of 1018 K-1053 K. The transition in the present KMC simulations has been found to be not as clear as the experiments may suggest. In general it can be said that all pits with zigzag edgeratios $\gamma_{zigzag} >= 0.7$ appear hexagonal in the simulations. Looking for example at $T = 1073$ K in Figure 6.13, the zigzag edge ratio is roughly $\gamma_{zigzag} = 0.6$. At those conditions, different trajectories can produce both hexagonal and circular pits in the simulation at the low pressure. However, there is a clear tendency of pits to only grow circular at the higher pressures at this temperature. Hence, this agrees very well with the Thomsen et al. [18] experiment. On the other hand, the temperature transition reported by Delehouzé et al. [19] oc-
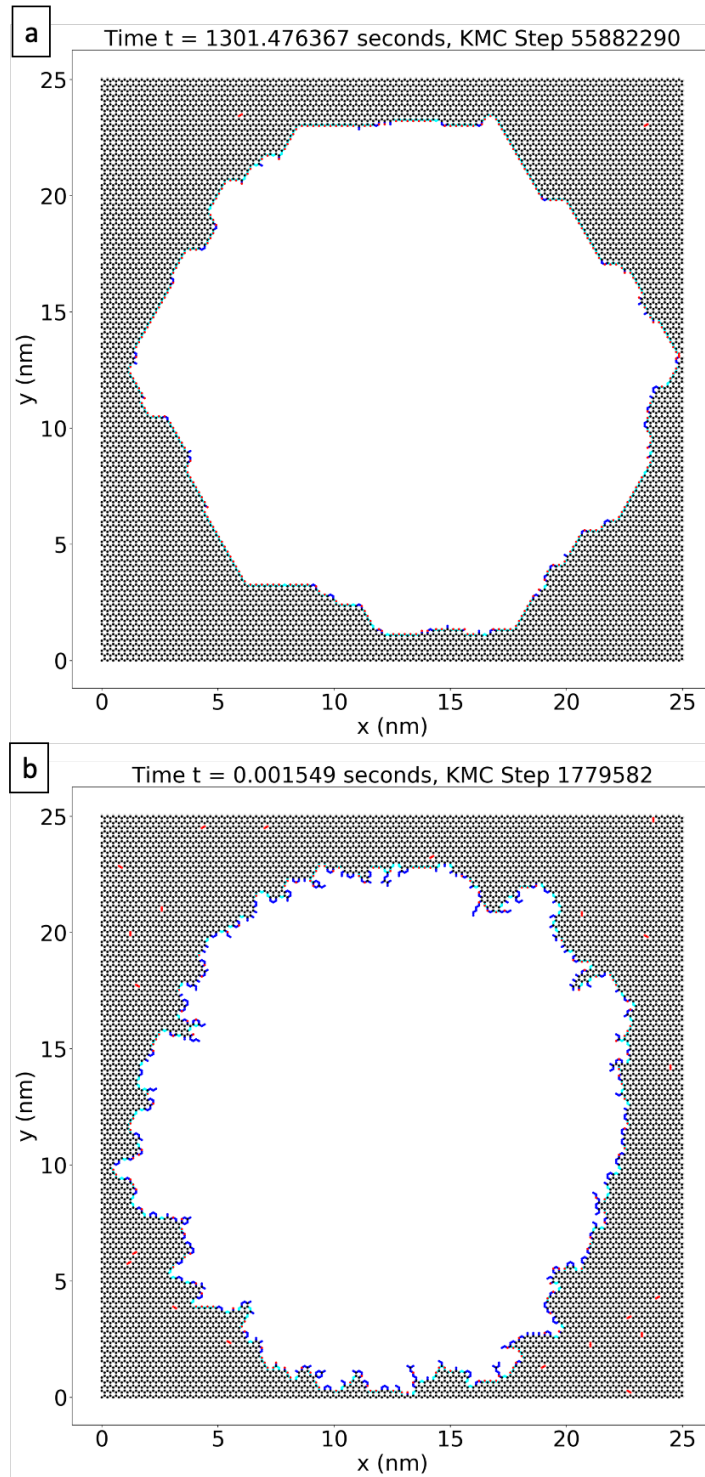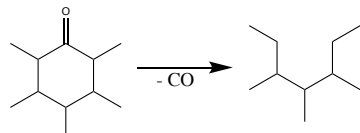
Figure 6.14: Geometry comparison of simulated etch pits: hexagonal shape with smooth zigzag carbon edges at $T = 850\,\mathrm{K}$, $P = 0.01\,\mathrm{mbar}$ (a); circular shape with rough carbon edges at $T = 1500\,\mathrm{K}$, $P = 100\,\mathrm{mbar}$ (b). A full videos of these simulations are provided as Supplementary Video SV2 (a) and Supplementary Video SV3 (b).

curs at considerably lower temperatures in the simulations, between 900 K-1000 K. Again, as was the case with the simulated pit growth rates, this is not in perfect agreement with available experimental data. But there is undoubtedly better agreement in the predicted pit geometries. This is further evidence for the validity of this novel computational framework to study graphene etching.

As was explained previously in Chapter 2, anisotropy (hexagonal pits) has been explained heuristically with removal of zigzag and armchair sites respectively at different rates. If armchair sites are removed much faster than zigzag sites, hexagons are created. Contrary, if zigzag sites are removed faster, the pits are isotropic (circular) with different degree of roughness along the edge. It is therefore necessary to consider how the oxidation rate on zigzag sites depends on the reaction conditions, relative to the armchair rates. Table 6.2 shows the key reactions in that respect. Generally, it can be seen that zigzag oxidation (OXzz1, OXzz2) has much higher activation energies than armchair oxidation (OXac1, OXac3). This already points to the fact that at armchair oxidation events are faster than zigzag oxidation events. The Arrhenius behavior of elementary reaction rates now explains the observed temperature dependence. Differences in activation energies have a much more pronounced effect on the reaction rate at lower temperatures. Hence, zigzag oxidation is relatively speaking much slower than armchair oxidation at lower temperatures than at high temperatures. This relative change however is enough to cause a transition from hexagonal pits, where zigzag oxidation is much slower, to circular pits, where zigzag oxidation is not that much slower anymore.

Table 6.2: Selected reactions of importance for pit geometry.

#	Reaction	$A\,(\mathrm{s}^{-1})$	$E_a\,(\mathrm{eV})$
OXzz1		1.2×10^{16}	3.622

OXzz2		1.2×10^{16}	2.300
OXac1		1.0×10^{13}	2.743
OXac3		1.0×10^{13}	1.829
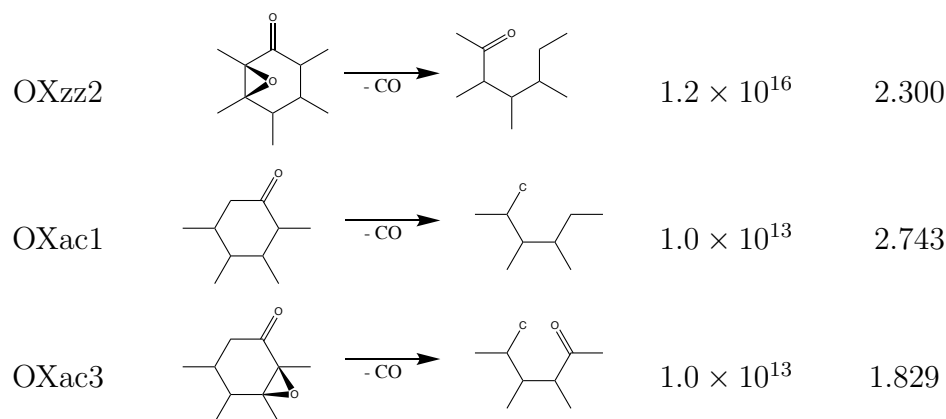
In order to understand what role the pressure plays, one needs to consider the effect of epoxides on the basal plane. The higher the pressure, the higher the epoxide coverage. This in turn has an effect on the zigzag and armchair oxidation rates. It can be seen in Table 6.2 that epoxides lower the activation energy for zigzag oxidation by 1.322 eV, whereas the armchair oxidation rate is only lowered by 0.914 eV. Hence, epoxides speed up zigzag oxidation more than they speed up armchair oxidation. This in turn means that the presence of epoxides tends to make pits more circular rather than hexagonal. And this is ultimately why extremely low pressures are necessary for anisotropic (hexagonal) etching.

6.2.4   Pitting Inhibition

Few studies have reported that etching from a point defect in the graphene basal plane only starts after a finite inhibition time. For example, Hahn et al. [60] reports inhibition times on the order of seconds at 833 K and air at atmospheric pressure. An explanation of this phenomenon has not heretofore been given.

The simulated inhibition times are shown in Figure 6.15 as a function of tempera- ture and pressure. Clearly, reasonably long inhibition times that make pit inhibition actually measurable in experiments are only present at low temperatures and pres-

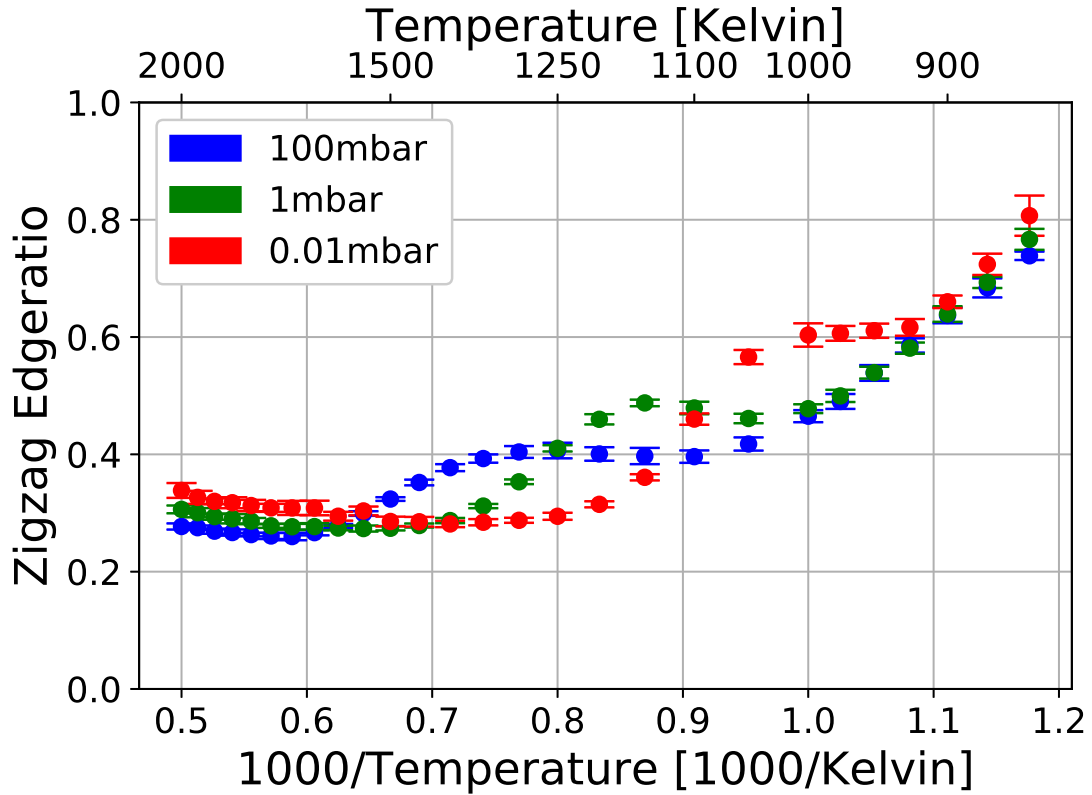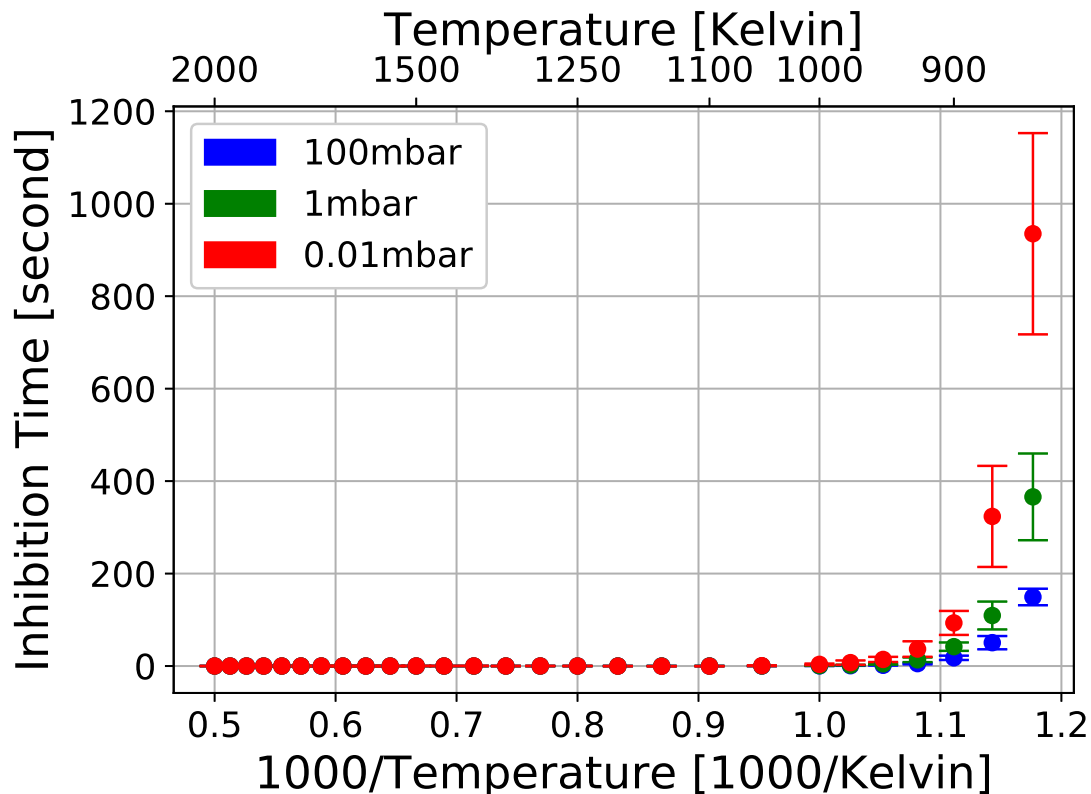Figure 6.15: Pit growth inhibition time as a function of temperature and pressure. The errorbars correspond to the standard deviation between all simulated trajectories for each case.

sure. This explains why there are not many studies that even mention the inhibition of pit growth. Quantitatively, at $T = 875\,\mathrm{K}$ and $P = 100\,\mathrm{mbar}$, the simulated inhibition time is $50\,\mathrm{s}$. This is in great agreement with the inhibition time reported by Hahn et al. [60].

Notice that the standard deviation between different trajectories is quite substantial at long inhibition times. This deviation however does not come from uncertainties induced through KMC, but rather is a manifestation of the stochastic nature of the carbon oxidation process at the atomic level. The mechanistic reason for the inhibition of pit growth reveals the reason for this behavior also: At temperatures $T > 1000\,\mathrm{K}$, the intrinsic rates of elementary oxidation reactions without the influence of epoxides are already fast enough to facilitate oxidation from small pits. In

contrast, at low temperatures, zigzag oxidation effectively does not occur without a nearby epoxide on the basal plane. Hence, the effect of epoxides is of critical importance. The number of edge sites is initially small. As a result, oxygen spillover is rare, since its apparent rate is proportional to the number of edge sites. This is actually one reason why pit growth eventually starts speeding up. Larger pits produce more epoxies through spillover, which are able to keep oxidation sustained at faster rates. The other reason is that larger pits have elongated edges, where neighboring edge sites are covered with oxygen and can speed up oxidation themselves. The other way to produce such epoxides is via adsorption, which is determined by the pressure. This is the reason why there are only short inhibition times at low temperature and higher pressure, whereas inhibition times increase drastically with lowering the pressure. These arguments can also be proven on the basis of the simulation results. Figure 6.12 (c) shows that indeed almost no oxidation events occur without the influence of neighboring oxygen species at low temperatures and pressures. Furthermore, Figure 6.8 shows where the epoxides required to overcome pit growth inhibition originate. At low pressures, they are solely created by spillover, whereas dissociative adsorption is viably fast at higher pressures. The before mentioned large deviations in inhibition times result from the slow timescales of either spillover or dissociative adsorption. While transition state theory predicts intrinsic reaction rates for these processes, they are still fundamentally rare events that result from random atomic motion. Hence, they actually occur at random times that follow a Poisson distribution.

Chapter 7 Conclusions and Future Work

7.1 Summary

This dissertation describes the development of a novel computational framework for the study of carbon oxidation at the atomic level, and applies it to understand graphene etching and pitting of graphitic carbon surfaces from first principles. A literature review in Chapter 2 shows that oxidative etching of a single graphene layer is mostly similar to pitting of the outermost layer of graphitic carbon surfaces and is therefore a sufficient problem for studying carbon oxidation on a fundamental level. In both cases, starting from structural defects on the material surface, etch pits grow as a result of localized removal of carbon through oxidation reactions. The lack of a comprehensive computational study of this phenomenon thus far is identified, and a discussion of existing experimental work makes apparent the value that such a fundamental study can add.

The development of the novel computational framework starts in Chapter 3 with a description of all elements of the computational approach. First, the problem setup, namely a single layer of graphene with monovacancy defects, subjected to oxygen gas, is defined and discussed with respect to its applicability and limitations. After that, the Kinetic Monte Carlo (KMC) method is identified as the appropriate method to carry on due to its capability of studying surface reactions at the length- and timescales at which pit growth is observed in graphene etching. A combination of Transition State Theory (TST) and Density Functional Theory (DFT) incorporates first principle based reaction kinetics into this KMC framework through a kinetic reaction mechanism. Descriptions of these methods are given on a conceptual level in order to clarify the methodologies, and point out advantages and possible shortcomings of this approach. The kinetic mechanism is then built on the basis of existing

89

DFT data in Chapter 4. It incorporates all elementary surface reactions that play a role in the oxidation of carbon materials at the atomic level under the conditions relevant to this study. Those are adsorption, dissociation, diffusion, oxidation and desorption reactions of various different oxygen and carbon-oxygen species. Chapter 5 then describes the implementation of this new mechanism into KMC, and provides a discussion of the statistical analysis that is necessary to obtain accurate results. This concludes the development of the novel computational framework.

The computational study of graphene etching is finally carried out in Chapter 6. It starts with a complete analysis of a single representative simulation, in order to show the kinds of results that can be inferred from this novel computational framework. In particular, the full picture of the dynamics of pitting is unveiled, which has heretofore not been attainable from previous studies. After that, pitting is examined across the whole range of simulated temperatures and pressures selected for this study. An analysis of the oxygen surface coverages on both edge and basal plane carbon sites provides the necessary background for the interpretation of following results. Pit growth rates, which are the most obvious and often only measurable quantity in experiments, are examined for the validation of the novel computational framework. Moreover, discussing them with regard to the underlying kinetic reaction mechanism gives a fundamental explanation of the apparent reaction behavior. At low temperatures and pressures, pitting is rate controlled by elementary oxidation reactions, whereas the rate control shifts to the adsorption reactions at higher temperatures and pressures. Next, the possible pit geometries, i.e. hexagonal pits with smooth edges and circular pits with rough edges, are examined as a function of temperature and pressure, and again discussed with regards to the underlying mechanism. It is shown that fast oxidation of armchair edge sites relative to zigzag edge sites is required for hexagonal etch pits, and this is favored by low temperatures and pressures. Lastly, the phenomenon of pit inhibition, i.e. a delay in the initial growth

of etch pits due to the initially small number of edge sites, is assessed. In all cases, the existence of nearby oxygen adsorbates, especially epoxide adsorbates on the basal plane, plays a key role in the oxidation process.

7.2 Original Contributions

1. **Development of a comprehensive atomic scale kinetic reaction mechanism for carbon oxidation:** Prior to this work, kinetic reaction mechanisms for the study of carbon oxidation in the context of pitting have either been crudely oversimplified for computational ease without accounting for fundamental knowledge from the atomic level, or just dealt with a small subset of the possible surface reactions due to their complexity. Here, a comprehensive kinetic reaction mechanism for carbon oxidation at the atomic level is constructed with fundamental reaction rate constants compiled from preexisting DFT simulation results.

2. **Implementation of novel mechanism into Kinetic Monte Carlo simulation framework:** The newly developed kinetic reaction mechanism is directly implemented in the readily available Zacros KMC code, which enables simulations of graphene etching and pitting for relevant time and lengthscales, which have previously not been in reach.

3. **First principle based computational study of graphene etching and pitting of graphitic carbon surfaces:** For the first time, graphene etching and pitting of graphitic carbon surfaces has been studied computationally from first principles. The simulations reveal on the one hand information about the dynamics of the oxidizing system, such as the constant pit growth rate. But also more intricate phenomena like the inhibition of pit growth at low pressures and temperatures has now we been studied in detail. Furthermore, all phenomena

can be explained fundamentally on the basis of the actual elementary surface reactions that control the overall process.

7.3 Future Work

1. **Optimization of reaction rate constants in the kinetic mechanism:** The rate constants used in this work have been compiled from several different DFT studies on different aspects of carbon oxidation from graphite edges as well as polyaromatic hydrocarbons (PAH). They carry uncertainty due to the relatively small but intrinsic inaccuracies of DFT itself, and the combination of such results from different sources that use different DFT setups and potentials. This range of uncertainty can be directly utilized to perform a parameter optimization for example with the objective of more accurate pit growth rates. Another route for optimization is to perform a fully coherent DFT study of all reactions included in the mechanism.

2. **Extension of kinetic mechanism to higher temperatures and inclusion of other gas species:** It has been seen that higher temperatures increasingly give the system access to surface reactions with higher activation energies. The kinetic mechanism has been built with a cutoff energy of around $3.5\,\text{eV}$. Hence, reactions with even higher activation energies will need to be added in order to extend the mechanism to higher temperatures. Furthermore, adding other (less reactive) gas species to the mechanism make it applicable to gas environments that are not predominantly composed of oxygen, such as mars' atmosphere.

3. **Extension of KMC framework to directly simulate multilayer graphene and graphite:** This work is limited in the setup of the computational problem to a single graphene layer. Modifications to the lattice based KMC implementation to include multiple layers could potentially be made with rea-

sonable effort, starting from this existing setup. Such an extension could explain the in depth growth of etch pits in graphite from first principles rather than through simplified model considerations.

4. **Oxidation of grain boundaries and other defects in carbon materials:** In order to truly predict macroscopic oxidation behavior of complex graphitic carbon materials form first principles, it is likely that other defects such as grain boundaries and impurities need to be considered alongside monovacancy defects that cause pitting. In principle, the kinetic mechanism developed here should still hold for those cases, although the necessity for additional surface species and reactions can not be excluded indefinitely.

5. **Pitting modelling:** The results found from this computational study of pitting, first and foremost the pit growth rates, could be utilized on a mesoscopic scale to build models that describe the structural evolution of macroscopic carbon materials due to pitting and therefore link first principle information about the carbon oxidation process on the atomic level to macroscopic material behavior. Such a model would have strong predictive capabilities, since the chemical reaction kinetics are effectively decoupled from the material structure, and therefore are universally valid for all possible conditions, even those encountered in hypersonic flight.

Appendix

A.1 Simple model simulation for pit shape transition

Simulations have been reproduced from [19, 61, 62] to observe the pit shape transition as a function of $\lambda = \frac{\text{rate of armchair removal}}{\text{rate of zigzag removal}}$.
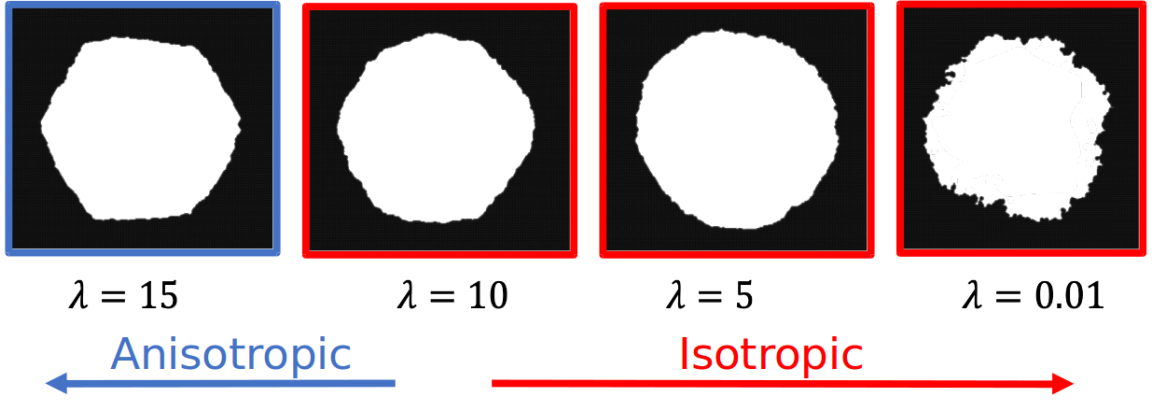
Figure A.1: Pit shape transition from anisotropic/hexagonal (fast armchair oxidation) to isotropic/circular (slow armchair oxidation) pits.

A.2 Derivation of the site-specific collision rate of an ideal gas with a graphene surface

Assuming ideal gas, one can derive the collision rate $k_{collision}$ of a gas particle with a surface as follows. Starting with the Maxwell-Boltzmann velocity distribution for an ideal gas

$$f(\mathbf{v}) = \left(\frac{m}{2\pi k_B T}\right)^{3/2} \exp\left[-\frac{m\left(v_x^2 + v_y^2 + v_z^2\right)}{2k_B T}\right], \tag{A.1}$$

with the mass m of a gas particle at velocity $\mathbf{v} = (v_x, v_y, v_z)$, one can derive the Maxwell-Boltzmann distribution for the v_x component as

$$f\left(v_x\right) dv_x = \left(\frac{m}{2\pi k_B T}\right)^{3/2} \exp\left(-\frac{mv_x^2}{2k_B T}\right) dv_x \int_{-\infty}^{\infty} \int_{-\infty}^{\infty} \exp\left[-\frac{m\left(v_y^2 + v_z^2\right)}{2k_B T}\right] dv_y dv_z$$

(A.2)

$$= \left(\frac{m}{2\pi k_B T}\right)^{1/2} \exp\left(-\frac{mv_x^2}{2k_B T}\right) dv_x .$$

(A.3)

The Gaussian integral $\int_{-\infty}^{\infty} e^{-ax^2} dx = \left(\frac{\pi}{a}\right)^{1/2}$ has been employed here. The Maxwell-Boltzmann distribution $f\left(v_x\right) dv_x$ represents the fraction of particles in the ideal gas with velocity v_x.

Consider now a differential surface element with area dA exposed to the ideal gas from one side. Furthermore, consider a region of the gas spanned by dA over a distance $v_x dt$ away from the surface, where dt is an infinitesimal time interval. The volume of that region is $v_x dt\, dA$, and it contains $nv_x dt\, dA$ gas particles. Here, n is the number density of the ideal gas. From above it is known that $f\left(v_x\right) dv_x$ is the fraction of particles in the region with velocity v_x. Hence, the number of particles hitting dA with a velocity v_x in a time interval dt is $nv_x dt\, dA\, f\left(v_x\right) dv_x$. As a result, the flux (number of particles hitting the surface per unit time and unit area) is simply $nv_x f\left(v_x\right) dv_x$. By integration over v_x (only positive v_x, which is the direction towards the surface), the total flux Γ to the surface follows as

$$\Gamma = n \int_0^{\infty} f\left(v_x\right) v_x\, dv_x$$

(A.4)

$$= n \int_0^{\infty} \left(\frac{m}{2\pi k_B T}\right)^{1/2} v_x \exp\left(-\frac{mv_x^2}{2k_B T}\right) dv_x$$

(A.5)

$$= n \left(\frac{m}{2\pi k_B T}\right)^{1/2} \int_0^{\infty} v_x \exp\left(-\frac{mv_x^2}{2k_B T}\right) dv_x .$$

(A.6)

With the integral identity $\int_0^\infty x e^{-ax^2} dx = \frac{1}{2a}$ one can furthermore obtain

$$\Gamma = n \left(\frac{m}{2\pi k_B T}\right)^{1/2} \frac{1}{2\left(\frac{m}{2k_B T}\right)} \tag{A.7}$$

$$= n \left(\frac{k_B T}{2\pi m}\right)^{1/2} . \tag{A.8}$$

Using the ideal gas law $n = \frac{N}{V} = \frac{P}{k_B T}$, the total flux to the surface is derived as

$$\Gamma = \frac{P}{\sqrt{2\pi m k_B T}} , \tag{A.9}$$

with units of $\frac{\text{number of collisions}}{\text{unit time} \times \text{unit surface area}}$. Since $k_{collision}$ needs to be the collision rate per adsorption site in KMC, Γ needs to be converted from the unit surface area to an effective area per adsorption site A_{eff}. Hence, the collision frequency is finally derived as

$$k_{collision} = \frac{P A_{eff}}{\sqrt{2\pi m k_B T}} . \tag{A.10}$$

This has units of $\frac{1}{\text{unit time} \times \text{adsorption site}}$, which is easily verified by the following unit check

$$\frac{1}{\text{unit time} \times \text{adsorption site}} = \frac{kg\, m^{-1}\, s^{-2} \times m^2\, \text{adsorption site}^{-1}}{\sqrt{kg \times m^2\, kg\, s^{-2}\, K^{-1} \times K}} \tag{A.11}$$

$$= \frac{kg\, m\, s^{-2}\, \text{adsorption site}^{-1}}{kg\, m\, s^{-1}} \tag{A.12}$$

$$= \frac{1}{s \times \text{adsorption site}} . \tag{A.13}$$

A.3   Comparison of pit radius calculated from initial vacancy and current position of the center of the pit

Figure A.2 compares the pit radii computed with the initial monovacancy and the current position of the pit center at conditions of $T = 1000\,\text{K}$ and $P = 1\,\text{mbar}$. Obviously, the static monovacancy center gives a larger radius than the pit center that is updated at every step. However, the radii deviate at most by $2\,\text{Å}$ at any given time. More importantly, this deviation is not increasing with time. Furthermore, the growth rates that are calculated from the linear fits differ by less than one percent.
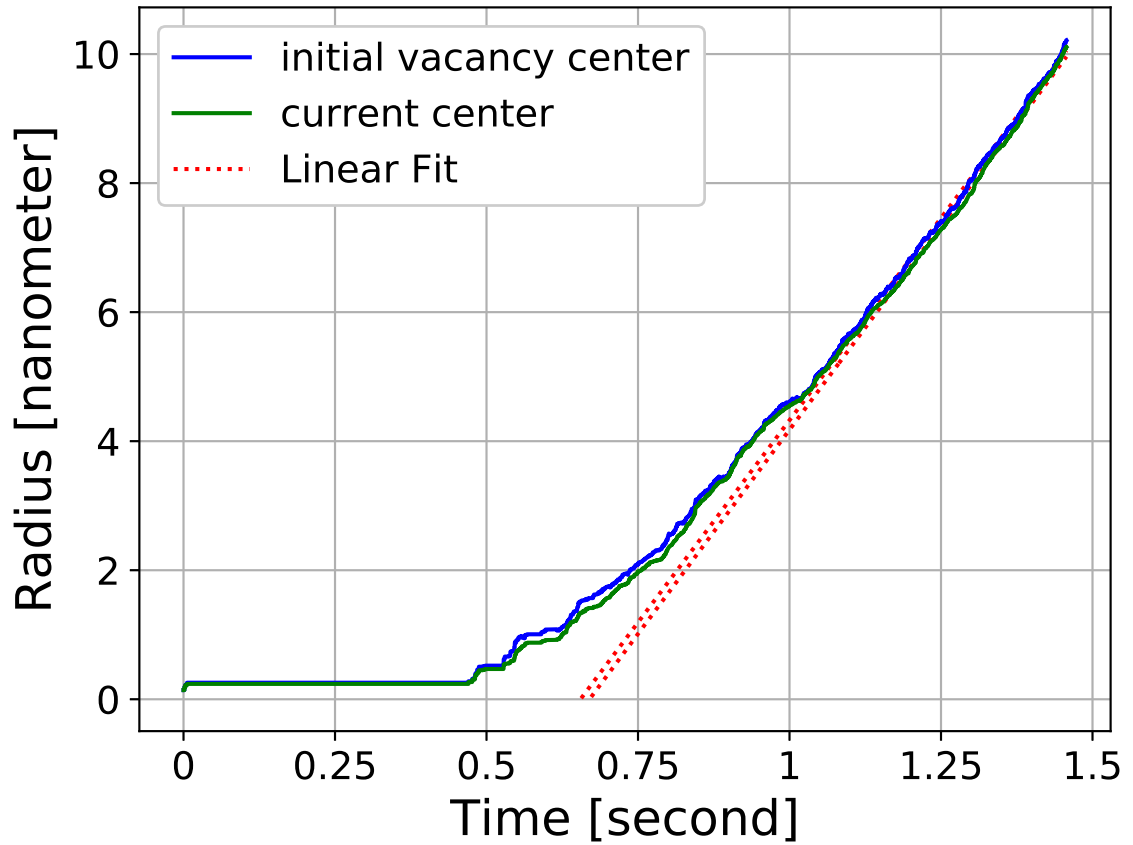
Figure A.2: Pit radius evolution with time at $T = 1000\,\mathrm{K}$ and $P = 1\,\mathrm{mbar}$. For comparison, radii are calculated from the position of the initial monovacancy and the current position of the pit center, showing only negligible deviation.

A.4   Pit radius evolution zero/negative inhibition time

Figure A.3 demonstrates an example where the inhibition time would be calculated as negative. In those cases, it is assumed to be zero.

A.5   Constant basal plane coverage

Figure A.4 demonstrates an example where the basal plane coverage reaches a steady state value (with fluctuations).
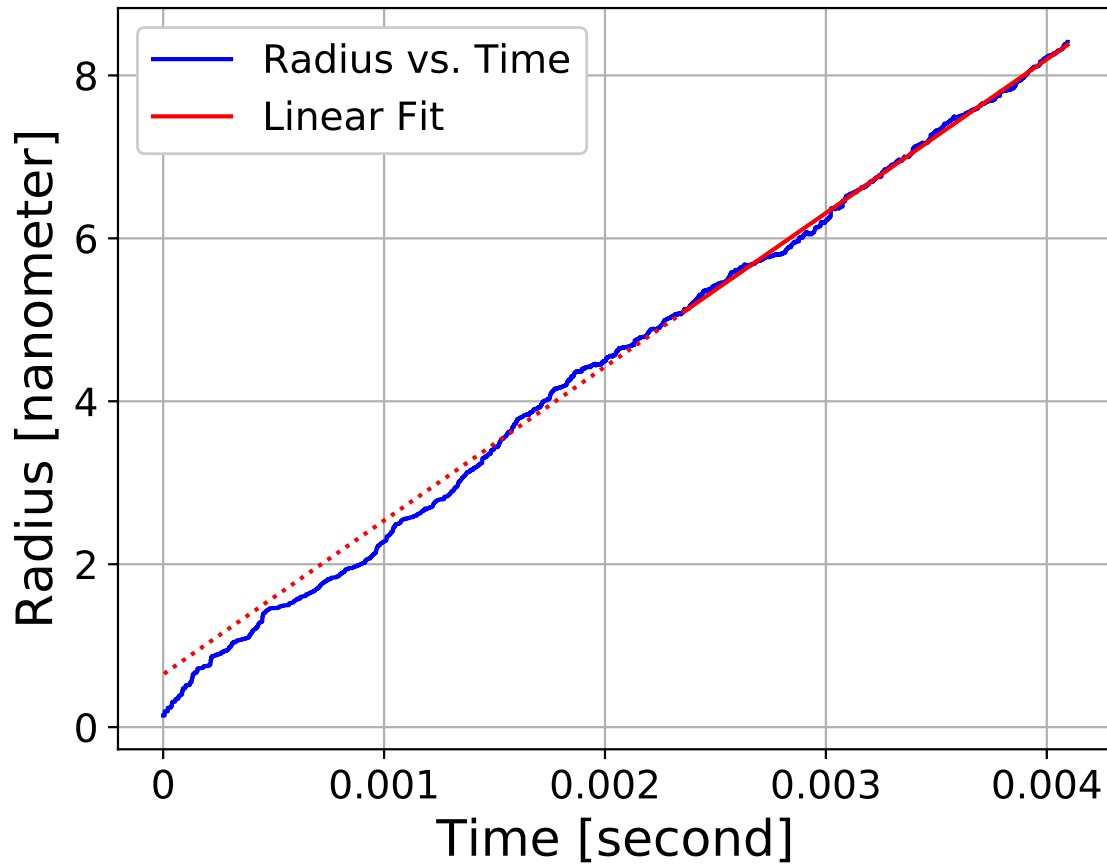
Figure A.3: Pit radius evolution with time at $T = 1300\,\mathrm{K}$ and $P = 100\,\mathrm{mbar}$. The linear fit does not cross zero radius at a positive time.

A.6   Net consumption/production of gas species

Figure A.5 demonstrates an example where molecular oxygen temporarily sees a net production, and eventually gets consumed.
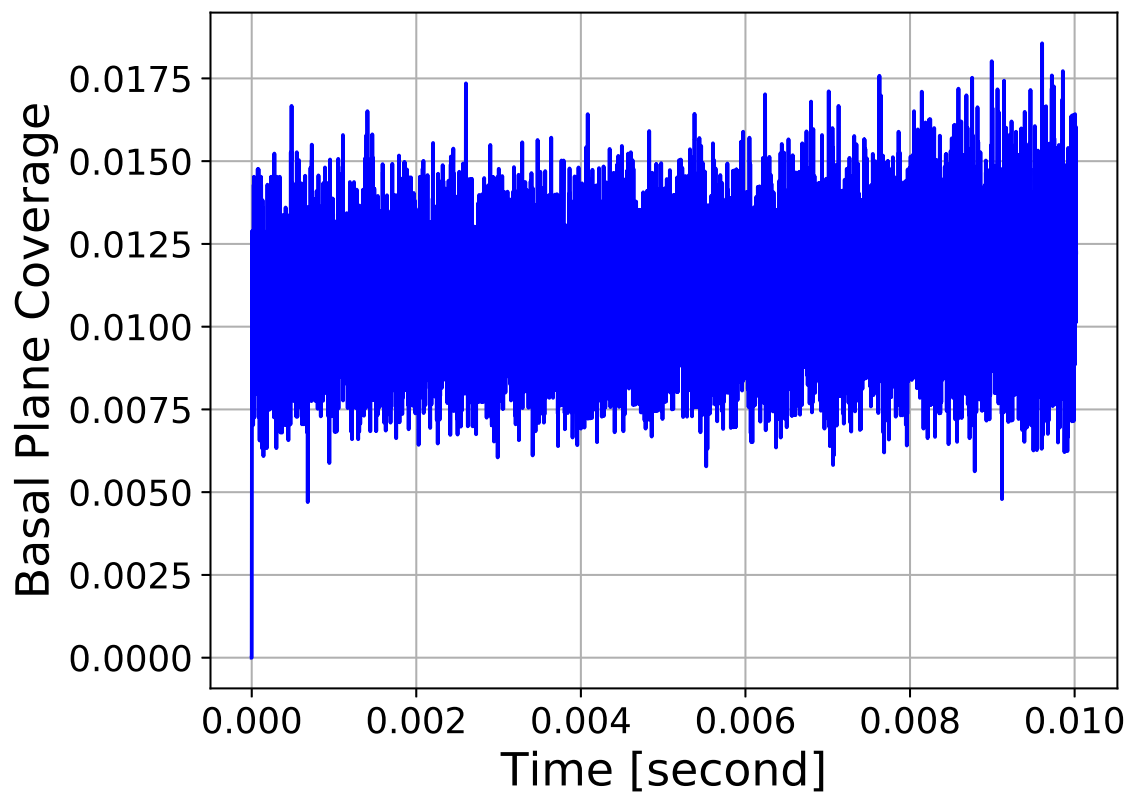
Figure A.4: Basal plane coverage evolution with time at $T = 2000\,\mathrm{K}$ and $P = 1\,\mathrm{mbar}$. The coverage almost instantly reaches a steady state value.
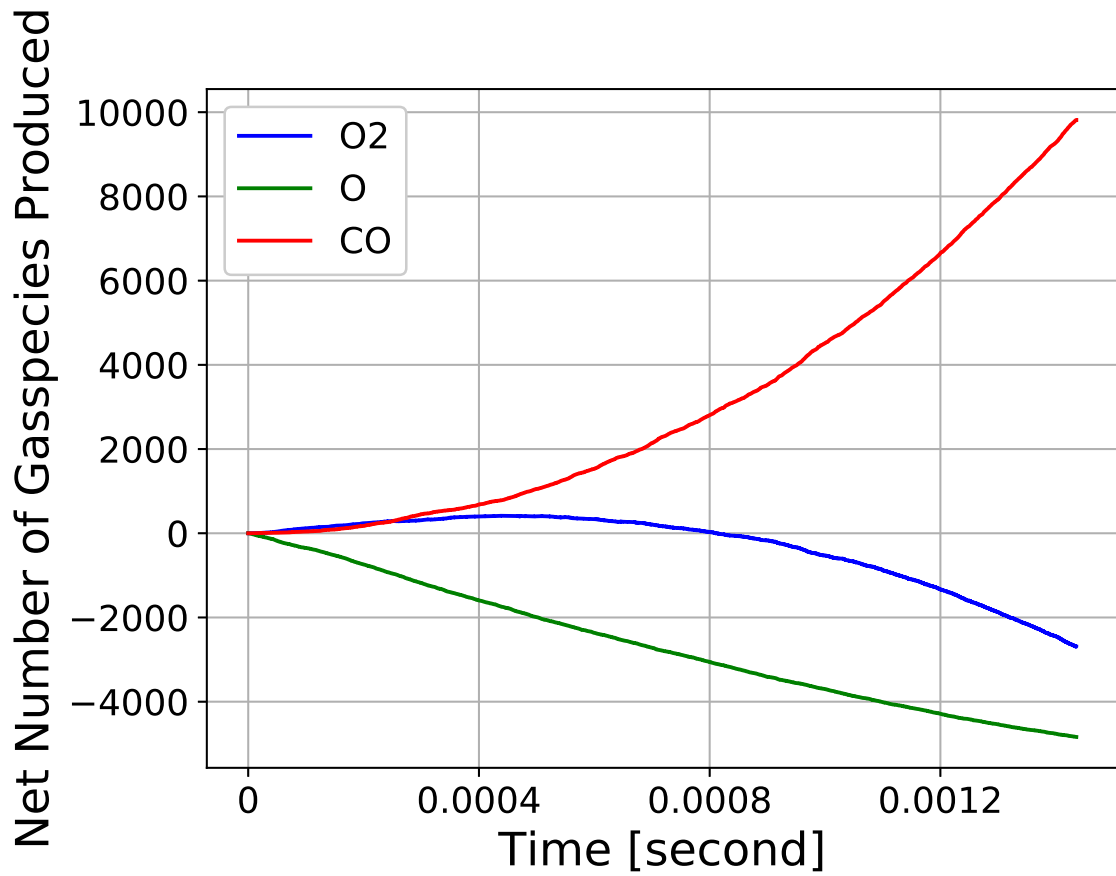
Figure A.5: Gas species evolution with time at $T = 1500\,\mathrm{K}$ and $P = 100\,\mathrm{mbar}$. There is an initial net production of O_2, until the pit grows large enough to consume more O_2, turning it back into a net consumption.

Bibliography

[1] I. A. Leyva. "The relentless pursuit of hypersonic flight". In: *Physics Today* 70.11 (Nov. 2017), pp. 30–36. DOI: 10.1063/PT.3.3762.

[2] W. H. Bowman and R. M. Lawrence. "Ablative materials for high-temperature thermal protection of space vehicles". In: *Journal of Chemical Education. Space Resource for Teachers* 48.10 (Oct. 1971), pp. 690–691. DOI: 10.1021/ed048p690.

[3] F. Panerai, A. Martin, N. N. Mansour, S. A. Sepka, and J. Lachaud. "Flow-tube Oxidation Experiments on the Carbon Preform of PICA". In: *44th AIAA Thermophysics Conference*. Reston, Virginia: American Institute of Aeronautics and Astronautics, June 2013, pp. 1–14. DOI: 10.2514/6.2013-2769.

[4] F. Panerai, J. C. Ferguson, J. Lachaud, A. Martin, M. J. Gasch, and N. N. Mansour. "Micro-tomography based analysis of thermal conductivity, diffusivity and oxidation behavior of rigid and flexible fibrous insulators". In: *International Journal of Heat and Mass Transfer* 108 (May 2017), pp. 801–811. DOI: 10.1016/j.ijheatmasstransfer.2016.12.048.

[5] X. Chen and B. Chen. "Direct Observation, Molecular Structure, and Location of Oxidation Debris on Graphene Oxide Nanosheets". In: *Environmental Science & Technology* 50.16 (Aug. 2016), pp. 8568–8577. DOI: 10.1021/acs.est.6b01020.

[6] G. V. Candler. "Rate Effects in Hypersonic Flows". In: *Annual Review of Fluid Mechanics* 51 (2019), pp. 379–402. DOI: 10.1146/annurev-fluid-010518-040258.

[7] Condensed Matter Physics Group at the University of Manchester (UK). *Image Library (Last accessed: November 8, 2020)*. URL: http://www.condmat.physics.manchester.ac.uk/imagelibrary/.

[8] K. S. Novoselov and A. K. Geim. "Electric Field Effect in Atomically Thin Carbon Films". In: *Science* 306.5696 (Oct. 2004), pp. 666–669. DOI: 10.1126/science.1102896.

[9] K. S. Novoselov, V. I. Fal'Ko, L. Colombo, P. R. Gellert, M. G. Schwab, and K. Kim. "A roadmap for graphene". In: *Nature* 490.7419 (2012), pp. 192–200. DOI: 10.1038/nature11458.

[10] A. K. Geim. "Graphene: Status and Prospects". In: *Science* 324.5934 (June 2009), pp. 1530–1534. DOI: 10.1126/science.1158877.

[11] S. P. Surwade, S. N. Smirnov, I. V. Vlassiouk, R. R. Unocic, G. M. Veith, S. Dai, and S. M. Mahurin. "Water desalination using nanoporous single-layer graphene". In: *Nature Nanotechnology* 10.5 (May 2015), pp. 459–464. DOI: 10.1038/nnano.2015.37.

[12] G. F. Schneider, S. W. Kowalczyk, V. E. Calado, G. Pandraud, H. W. Zandbergen, L. M. K. Vandersypen, and C. Dekker. "DNA Translocation through Graphene Nanopores". In: *Nano Letters* 10.8 (Aug. 2010), pp. 3163–3167. DOI: `10.1021/nl102069z`.

[13] S. J. Heerema and C. Dekker. "Graphene nanodevices for DNA sequencing". In: *Nature Nanotechnology* 11.2 (Feb. 2016), pp. 127–136. DOI: `10.1038/nnano.2015.307`.

[14] A. Kaplan, Z. Yuan, J. D. Benck, A. Govind Rajan, X. S. Chu, Q. H. Wang, and M. S. Strano. "Current and future directions in electron transfer chemistry of graphene". In: *Chemical Society Reviews* 46.15 (2017), pp. 4530–4571. DOI: `10.1039/C7CS00181A`.

[15] F. Schwierz. "Graphene transistors". In: *Nature Nanotechnology* 5.7 (2010), pp. 487–496. DOI: `10.1038/nnano.2010.89`.

[16] R. Kumar, S. Sahoo, E. Joanni, R. K. Singh, W. K. Tan, K. K. Kar, and A. Matsuda. "Recent progress in the synthesis of graphene and derived materials for next generation electrodes of high performance lithium ion batteries". In: *Progress in Energy and Combustion Science* 75 (Nov. 2019), p. 100786. DOI: `10.1016/j.pecs.2019.100786`.

[17] L. P. Biró, P. Nemes-Incze, and P. Lambin. "Graphene: nanoscale processing and recent applications". In: *Nanoscale* 4.6 (2012), pp. 1824–1839. DOI: `10.1039/C1NR11067E`.

[18] J. D. Thomsen, J. Kling, D. M. A. Mackenzie, P. Bøggild, and T. J. Booth. "Oxidation of Suspended Graphene: Etch Dynamics and Stability Beyond 1000 °C". In: *ACS Nano* 13 (Jan. 2019), acsnano.8b08979. DOI: `10.1021/acsnano.8b08979`.

[19] A. Delehouzé, F. Rebillat, P. Weisbecker, J.-M. Leyssale, J.-F. Epherre, C. Labrugère, and G. L. Vignoles. "Temperature induced transition from hexagonal to circular pits in graphite oxidation by O2". In: *Applied Physics Letters* 99.4 (July 2011), p. 044102. DOI: `10.1063/1.3615801`.

[20] M. Inagaki and F. Kang. *Materials Science and Engineering of Carbon: Fundamentals.* Elsevier, 2014. DOI: `10.1016/C2013-0-13699-9`.

[21] M. Inagaki, F. Kang, M. Toyoda, and H. Konno. *Advanced Materials Science and Engineering of Carbon.* Elsevier, 2014, pp. 1–434. DOI: `10.1016/C2012-0-03601-0`.

[22] P. Debye and P. Scherrer. "Interference on inordinate oriented particles in roentgen light". In: *Physikalische Zeitschrift* 17 (1916), pp. 277–283.

[23] H. O. Pierson. "Handbook of Carbon, Graphite, Diamonds and Fullerenes: Processing, Properties and Applications (Materials Science and Process Technology)". In: *William Andrew Inc* (1993), p. 399. DOI: `http://dx.doi.org/10.1016/B978-0-8155-1339-1.50008-6`.

[24]   M. S. Dresselhaus, G. Dresselhaus, K. Sugihara, I. L. Spain, and H. A. Gold-berg. *Graphite Fibers and Filaments*. 2011, p. 396. DOI: `10.1002/adma.19890010410`.

[25]   B. T. Kelly. *Physics of Graphite*. 1981.

[26]   T. Xu and L. Sun. "Structural defects in graphene". In: *Defects in Advanced Electronic Materials and Novel Low Dimensional Structures*. Elsevier, 2018, pp. 137–160. DOI: `10.1016/B978-0-08-102053-1.00005-3`.

[27]   K. Amsharov. *Breakthrough in graphene research (Last accessed: November 8, 2020)*. URL: `https://www.fau.eu/2019/01/29/news/research/breakthrough-in-graphene-research/`.

[28]   D. Lungerich, O. Papaianina, M. Feofanov, J. Liu, M. Devarajulu, S. I. Troyanov, S. Maier, and K. Amsharov. "Dehydrative π-extension to nanographenes with zig-zag edges". In: *Nature communications* 9.1 (2018), pp. 1–8.

[29]   R. E. Franklin. "Crystallite growth in graphitizing and non-graphitizing carbons". In: *Proceedings of the Royal Society of London. Series A. Mathematical and Physical Sciences* 209.1097 (Oct. 1951), pp. 196–218. DOI: `10.1098/rspa.1951.0197`.

[30]   P. J. F. Harris. "New Perspectives on the Structure of Graphitic Carbons". In: *Critical Reviews in Solid State and Materials Sciences* 30.4 (Oct. 2005), pp. 235–253. DOI: `10.1080/10408430500406265`.

[31]   D. J. Johnson. "Structure-property relationships in carbon fibres". In: *Journal of Physics D: Applied Physics* 20.3 (1987), p. 286.

[32]   P. L. J. Walker. "Gas Reactions of Carbons and Graphites". In: *Proceedings of the Conferences on Carbon*. 1956.

[33]   P. L. J. Walker. "Carbon Gasification – A Ubiquitous Reaction of Great Importance to Mankind". In: *Carbon and Coal Gasification*. Vol. 24. 1. Dordrecht: Springer Netherlands, Jan. 1986, pp. 3–23. DOI: `10.1007/978-94-009-4382-7_1`.

[34]   N. M. Laurendeau. "Heterogeneous kinetics of coal char gasification and combustion". In: *Progress in Energy and Combustion Science* 4.4 (Jan. 1978), pp. 221–270. DOI: `10.1016/0360-1285(78)90008-4`.

[35]   J. J. Kane, C. I. Contescu, R. E. Smith, G. Strydom, and W. E. Windes. "Understanding the reaction of nuclear graphite with molecular oxygen: Kinetics, transport, and structural evolution". In: *Journal of Nuclear Materials* 493 (Sept. 2017), pp. 343–367. DOI: `10.1016/j.jnucmat.2017.06.001`.

[36]   N. R. Laine, F. J. Vastola, and P. L. J. Walker. "The Importance of Active Surface Area in the Carbon-Oxygen Reaction". In: *The Journal of Physical Chemistry* 67.10 (Oct. 1963), pp. 2030–2034. DOI: `10.1021/j100804a016`.

[37]   J. M. Thomas. "Microscopic studies of graphite oxidation". In: *Chemistry and Physics of Carbon*. Ed. by P. L. J. Walker. Vol. 1. Marcel Dekker, New York, 1965, pp. 121–202.

[38] W. J. Thomas. "Effect of oxidation on the pore structure of some graphitized carbon blacks". In: *Carbon* 3.4 (Feb. 1966), pp. 435–443. DOI: 10.1016/0008-6223(66)90029-7.

[39] D. W. McKee. "Carbon and Graphite Science". In: *Annual Review of Materials Science* 3.1 (Aug. 1973), pp. 195–231. DOI: 10.1146/annurev.ms.03.080173.001211.

[40] K. T. Nicholson, T. K. Minton, and S. J. Sibener. "Spatially Anisotropic Etching of Graphite by Hyperthermal Atomic Oxygen". In: *The Journal of Physical Chemistry B* 109.17 (May 2005), pp. 8476–8480. DOI: 10.1021/jp045960c.

[41] F. Panerai, A. Martin, and N. N. Mansour. "Numerical and experimental study of carbon fiber oxidation". In: *52nd Aerospace Sciences Meeting*. Reston, Virginia: American Institute of Aeronautics and Astronautics, Jan. 2014, pp. 1–15. DOI: 10.2514/6.2014-1208.

[42] Z. Wangxi, L. Jie, and W. Gang. "Evolution of structure and properties of PAN precursors during their conversion to carbon fibers". In: *Carbon* 41.14 (2003), pp. 2805–2812. DOI: 10.1016/S0008-6223(03)00391-9.

[43] J. R. Hahn. "Kinetic study of graphite oxidation along two lattice directions". In: *Carbon* 43.7 (June 2005), pp. 1506–1511. DOI: 10.1016/j.carbon.2005.01.032.

[44] E. McCafferty. "The electrode kinetics of pit initiation on aluminum". In: *Corrosion Science* 37.3 (Mar. 1995), pp. 481–492. DOI: 10.1016/0010-938X(94)00150-5.

[45] E. McCafferty. "Semiconductor aspects of the passive oxide film on aluminum as modified by surface alloying". In: *Corrosion Science* 45.2 (Feb. 2003), pp. 301–308. DOI: 10.1016/S0010-938X(02)00095-1.

[46] Z. Szklarska-Smialowska. "Pitting corrosion of aluminum". In: *Corrosion Science* 41.9 (Aug. 1999), pp. 1743–1767. DOI: 10.1016/S0010-938X(99)00012-8.

[47] M. A. Amin. "Metastable and stable pitting events on Al induced by chlorate and perchlorate anions—Polarization, XPS and SEM studies". In: *Electrochimica Acta* 54.6 (Feb. 2009), pp. 1857–1863. DOI: 10.1016/j.electacta.2008.10.009.

[48] G. R. Hennig. "Electron microscopy of reactivity changes near lattice defects in graphite". In: *Chemistry and Physics of Carbon*. Ed. by P. L. J. Walker. Vol. 2. Marcel Dekker, New York, 1966. Chap. 1, pp. 1–49.

[49] L. R. Radovic, P. L. J. Walker, and R. G. Jenkins. "Importance of carbon active sites in the gasification of coal chars". In: *Fuel* 62.7 (July 1983), pp. 849–856. DOI: 10.1016/0016-2361(83)90041-8.

[50] E. E. G. Hughes, B. R. Williams, and J. M. Thomas. "Etching of graphite surfaces with oxygen". In: *Transactions of the Faraday Society* 58 (1962), p. 2011. DOI: 10.1039/tf9625802011.

[51] J. Brunner and H. Hammerschmid. "Zur Morphologie des Graphits". In: *Zeitschrift für anorganische und allgemeine Chemie* 155.1 (July 1926), pp. 255–256. DOI: 10.1002/zaac.19261550125.

[52] G. R. Hennig. "Catalytic oxidation of graphite". In: *Journal of Inorganic and Nuclear Chemistry* 24.9 (1962). DOI: 10.1016/0022-1902(62)80258-9.

[53] P. J. Goethel and R. T. Yang. "Mechanism of catalyzed graphite oxidation by monolayer channeling and monolayer edge recession". In: *Journal of Catalysis* 119.1 (Sept. 1989), pp. 201–214. DOI: 10.1016/0021-9517(89)90146-2.

[54] J. M. Thomas. "Reactivity of carbon: Some current problems and trends". In: *Carbon* 8.4 (Oct. 1970), pp. 413–421. DOI: 10.1016/0008-6223(70)90001-1.

[55] B. McCarroll and D. W. McKee. "The reactivity of graphite surfaces with atoms and molecules of hydrogen, oxygen and nitrogen". In: *Carbon* 9.3 (May 1971), pp. 301–311. DOI: 10.1016/0008-6223(71)90049-2.

[56] J. M. Thomas and C. Roscoe. "Non-basal glide in graphite". In: *Journal of Nuclear Materials* 15.3 (Jan. 1965), pp. 245–246. DOI: 10.1016/0022-3115(65)90188-1.

[57] E. E. G. Hughes, J. M. Thomas, H. Marsh, and R. Reed. "Origin of etch pits on graphite surfaces". In: *Carbon* 1.3 (Apr. 1964), pp. 339–343. DOI: 10.1016/0008-6223(64)90289-1.

[58] R. T. Yang. "Etch–Decoration Electron Microscopy Studies of the Gas–Carbon Reactions". In: *Chemistry and Physics of Carbon: Volume 19*. 1984. Chap. 3.

[59] R. Edel, T. Grabnic, B. Wiggins, and S. J. Sibener. "Atomically-Resolved Oxidative Erosion and Ablation of Basal Plane HOPG Graphite Using Supersonic Beams of O 2 with Scanning Tunneling Microscopy Visualization". In: *The Journal of Physical Chemistry C* 122.26 (July 2018), pp. 14706–14713. DOI: 10.1021/acs.jpcc.8b04139.

[60] J. R. Hahn, H. Kang, S. M. Lee, and Y. H. Lee. "Mechanistic Study of Defect-Induced Oxidation of Graphite". In: *The Journal of Physical Chemistry B* 103.45 (Nov. 1999), pp. 9944–9951. DOI: 10.1021/jp9920895.

[61] C. D. Eklund. "A scanning electron microscope study of the reaction of graphite with carbon dioxide". PhD thesis. University of Colorado, Boulder, 1976.

[62] E. F. Brown. "Analyzing the oxidation of graphite using a microcomputer". In: *Computers & Chemistry* 12.1 (1988), pp. 27–37. DOI: 10.1016/0097-8485(88)85004-6.

[63] S. Poovathingal, T. E. Schwartzentruber, S. G. Srinivasan, and A. C. T. van Duin. "Large Scale Computational Chemistry Modeling of the Oxidation of Highly Oriented Pyrolytic Graphite". In: *The Journal of Physical Chemistry A* 117.13 (Apr. 2013), pp. 2692–2703. DOI: 10.1021/jp3125999.

[64] A. C. Van Duin, S. Dasgupta, F. Lorant, and W. A. Goddard. "ReaxFF: A reactive force field for hydrocarbons". In: *Journal of Physical Chemistry A* 105.41 (2001), pp. 9396–9409. DOI: 10.1021/jp004368u.

[65] N. Chen and R. T. Yang. "Ab Initio Molecular Orbital Study of the Unified Mechanism and Pathways for GasCarbon Reactions". In: *The Journal of Physical Chemistry A* 102.31 (July 1998), pp. 6348–6356. DOI: 10.1021/jp981518g.

[66] N. Chen and R. T. Yang. "Ab initio molecular orbital calculation on graphite: Selection of molecular system and model chemistry". In: *Carbon* 36.7-8 (1998), pp. 1061–1070. DOI: 10.1016/S0008-6223(98)00078-5.

[67] J. A. Moulijn and F. Kapteijn. "Towards a unified theory of reactions of carbon with oxygen-containing molecules". In: *Carbon* 33.8 (Jan. 1995), pp. 1155–1165. DOI: 10.1016/0008-6223(95)00070-T.

[68] S. G. Chen, R. T. Yang, F. Kapteijn, and J. A. Moulijn. "A New Surface Oxygen Complex on Carbon: Toward a Unified Mechanism for Carbon Gasification Reactions". In: *Industrial & Engineering Chemistry Research* 32.11 (Nov. 1993), pp. 2835–2840. DOI: 10.1021/ie00023a054.

[69] K. Sendt and B. S. Haynes. "Density functional study of the chemisorption of O2 on the armchair surface of graphite". In: *Proceedings of the Combustion Institute* 30.2 (Jan. 2005), pp. 2141–2149. DOI: 10.1016/j.proci.2004.08.064.

[70] K. Sendt and B. S. Haynes. "Density functional study of the chemisorption of O2 on the zig-zag surface of graphite". In: *Combustion and Flame* 143.4 (Dec. 2005), pp. 629–643. DOI: 10.1016/j.combustflame.2005.08.026.

[71] K. Sendt and B. S. Haynes. "Density Functional Study of the Reaction of Carbon Surface Oxides: The Behavior of Ketones". In: *The Journal of Physical Chemistry A* 109.15 (Apr. 2005), pp. 3438–3447. DOI: 10.1021/jp045111p.

[72] K. Sendt and B. S. Haynes. "Modelling CO desorption from carbon chars using density functional theory". In: *5th Asia-Pacific Conference on Combustion, ASPACC 2005: Celebrating Prof. Bob Bilger's 70th Birthday*. January 2005. 2005, pp. 121–124.

[73] K. Sendt and B. S. Haynes. "Density Functional Study of the Chemisorption of O2 Across Two Rings of the Armchair Surface of Graphite". In: *The Journal of Physical Chemistry C* 111.14 (Apr. 2007), pp. 5465–5473. DOI: 10.1021/jp067363r.

[74] K. Sendt and B. S. Haynes. "Modelling Chemisorption of O2 on Carbon Chars Using Density Functional Theory". In: *Proceedings of the Australian Combustion Symposium*. 2007.

[75] K. Sendt and B. S. Haynes. "Density functional study of the reaction of O2 with a single site on the zigzag edge of graphene". In: *Proceedings of the Combustion Institute* 33.2 (Jan. 2011), pp. 1851–1858. DOI: 10.1016/j.proci.2010.06.021.

[76] R. Larciprete, S. Fabris, T. Sun, P. Lacovig, A. Baraldi, and S. Lizzit. "Dual Path Mechanism in the Thermal Reduction of Graphene Oxide". In: *Journal of the American Chemical Society* 133.43 (Nov. 2011), pp. 17315–17321. DOI: 10.1021/ja205168x.

[77] R. Larciprete, P. Lacovig, S. Gardonio, A. Baraldi, and S. Lizzit. "Atomic Oxygen on Graphite: Chemical Characterization and Thermal Reduction". In: *The Journal of Physical Chemistry C* 116.18 (May 2012), pp. 9900–9908. DOI: 10.1021/jp2098153.

[78] A. Montoya, T.-T. T. Truong, F. Mondragón, and T. N. Truong. "CO Desorption from Oxygen Species on Carbonaceous Surface: 1. Effects of the Local Structure of the Active Site and the Surface Coverage". In: *The Journal of Physical Chemistry A* 105.27 (July 2001), pp. 6757–6764. DOI: 10.1021/jp010572l.

[79] A. Montoya, F. Mondragón, and T. N. Truong. "First-Principles Kinetics of CO Desorption from Oxygen Species on Carbonaceous Surface". In: *The Journal of Physical Chemistry A* 106.16 (Apr. 2002), pp. 4236–4239. DOI: 10.1021/jp0144294.

[80] A. Montoya, F. Mondragón, and T. N. Truong. "CO2 adsorption on carbonaceous surfaces: a combined experimental and theoretical study". In: *Carbon* 41.1 (Jan. 2003), pp. 29–39. DOI: 10.1016/S0008-6223(02)00249-X.

[81] Ž. Šljivančanin, A. S. Milošević, Z. S. Popović, and F. R. Vukajlović. "Binding of atomic oxygen on graphene from small epoxy clusters to a fully oxidized surface". In: *Carbon* 54 (2013), pp. 482–488. DOI: 10.1016/j.carbon.2012.12.008.

[82] N. Liu, Z. Pan, L. Fu, C. Zhang, B. Dai, and Z. Liu. "The origin of wrinkles on transferred graphene". In: *Nano Research* 4.10 (2011), pp. 996–1004. DOI: 10.1007/s12274-011-0156-3.

[83] X. Shen, X. Lin, N. Yousefi, J. Jia, and J. K. Kim. "Wrinkling in graphene sheets and graphene oxide papers". In: *Carbon* 66 (2014), pp. 84–92. DOI: 10.1016/j.carbon.2013.08.046.

[84] Z. Pan, N. Liu, L. Fu, and Z. Liu. "Wrinkle engineering: A new approach to massive graphene nanoribbon arrays". In: *Journal of the American Chemical Society* 133.44 (2011), pp. 17578–17581. DOI: 10.1021/ja207517u.

[85] R. I. Singh and M. Frenklach. "A mechanistic study of the influence of graphene curvature on the rate of high-temperature oxidation by molecular oxygen". In: *Carbon* 101 (May 2016), pp. 203–212. DOI: 10.1016/j.carbon.2016.01.090.

[86] F. Oberhuber, S. Blien, F. Schupp, D. Weiss, and J. Eroms. "Anisotropic etching of graphene in inert and oxygen atmospheres". In: *physica status solidi (a)* 214.2 (Feb. 2017), p. 1600459. DOI: 10.1002/pssa.201600459.

[87]   X. Chu, L. D. Schmidt, S. G. Chen, and R. T. Yang. "Catalyzed Carbon Gasification Studied by Scanning Tunneling Microscopy and Atomic Force Microscopy". In: *Journal of Catalysis* 140.2 (Apr. 1993), pp. 543–556. DOI: `10.1006/jcat.1993.1104`.

[88]   G. Dobrik, L. Tapasztó, and L. P. Biró. "Selective etching of armchair edges in graphite". In: *Carbon* 56 (May 2013), pp. 332–338. DOI: `10.1016/j.carbon.2013.01.018`.

[89]   D. E. Rosner and H. D. Allendorf. "Nitrogen as an ablative reactant in dissociated air". In: *AIAA Journal* 8.1 (Jan. 1970), pp. 166–168. DOI: `10.2514/3.5628`.

[90]   V. J. Murray and T. K. Minton. "Gas-surface interactions of atomic nitrogen with vitreous carbon". In: *Carbon* 150 (Sept. 2019), pp. 85–92. DOI: `10.1016/j.carbon.2019.04.117`.

[91]   L. R. Radovic and B. Bockrath. "On the Chemical Nature of Graphene Edges: Origin of Stability and Potential for Magnetism in Carbon Materials". In: *Journal of the American Chemical Society* 127.16 (Apr. 2005), pp. 5917–5927. DOI: `10.1021/ja050124h`.

[92]   K. Erickson, R. Erni, Z. Lee, N. Alem, W. Gannett, and A. Zettl. "Determination of the Local Chemical Structure of Graphene Oxide and Reduced Graphene Oxide". In: *Advanced Materials* 22.40 (Oct. 2010), pp. 4467–4472. DOI: `10.1002/adma.201000732`.

[93]   F. J. Keil. "Multiscale Modelling in Computational Heterogeneous Catalysis". In: *Topics in Current Chemistry: Multiscale Molecular Methods in Applied Chemistry*. Vol. 307. 2011, pp. 69–107. DOI: `10.1007/128_2011_128`.

[94]   K. Chenoweth, A. C. Van Duin, and W. A. Goddard. "ReaxFF reactive force field for molecular dynamics simulations of hydrocarbon oxidation". In: *Journal of Physical Chemistry A* 112.5 (2008), pp. 1040–1053. DOI: `10.1021/jp709896w`.

[95]   H. B. Schlegel. "Geometry optimization". In: *Wiley Interdisciplinary Reviews: Computational Molecular Science* 1.5 (2011), pp. 790–809. DOI: `10.1002/wcms.34`.

[96]   C. J. Cramer. *Essentials of Computational Chemistry: Theories and Models*. Wiley, 2004.

[97]   R. A. van Santen. *Computational Methods in Catalysis and Materials Science*. Ed. by R. A. van Santen and P. Sautet. Wiley, Jan. 2009. DOI: `10.1002/9783527625482`.

[98]   J. K. Norskov, F. Studt, F. Abild-Pedersen, and T. Bligaard. *Fundamental Concepts in Heterogeneous Catalysis*. John Wiley & Sons, Inc., 2014.

[99]   A. F. Voter. "Introduction to the Kinetic Monte Carlo Method". In: *Radiation Effects in Solids*. Dordrecht: Springer Netherlands, 2007, pp. 1–23. DOI: `10.1007/978-1-4020-5295-8_1`.

[100] S. Glasstone, K. J. Laidler, and H. Eyring. *The Theory of Rate Processes: The Kinetics of Chemical Reactions, Viscosity, Diffusion and Electrochemical Phenomena*. McGraw-Hill, 1941.

[101] G. H. Vineyard. "Frequency factors and isotope effects in solid state rate processes". In: *Journal of Physics and Chemistry of Solids* 3.1-2 (Jan. 1957), pp. 121–127. DOI: 10.1016/0022-3697(57)90059-8.

[102] D. T. Gillespie. *Markov Processes: An Introduction for Physical Scientists*. Academic Press, 1992.

[103] D. T. Gillespie. "A general method for numerically simulating the stochastic time evolution of coupled chemical reactions". In: *Journal of Computational Physics* 22.4 (Dec. 1976), pp. 403–434. DOI: 10.1016/0021-9991(76)90041-3.

[104] D. T. Gillespie. "Exact Stochastic Simulation of Coupled Chemical Reactions". In: *The Journal of Physical Chemistry* 81.25 (Dec. 1977), pp. 2340–2361. DOI: 10.1021/j100540a008.

[105] D. T. Gillespie. "Approximate accelerated stochastic simulation of chemically reacting systems". In: *The Journal of Chemical Physics* 115.4 (July 2001), pp. 1716–1733. DOI: 10.1063/1.1378322.

[106] D. T. Gillespie. "Stochastic Simulation of Chemical Kinetics". In: *Annual Review of Physical Chemistry* 58.1 (May 2007), pp. 35–55. DOI: 10.1146/annurev.physchem.58.032806.104637.

[107] D. T. Gillespie, A. Hellander, and L. R. Petzold. "Perspective: Stochastic algorithms for chemical kinetics". In: *The Journal of Chemical Physics* 138.17 (May 2013), p. 170901. DOI: 10.1063/1.4801941.

[108] D. T. Gillespie. "A rigorous derivation of the chemical master equation". In: *Physica A: Statistical Mechanics and its Applications* 188.1-3 (Sept. 1992), pp. 404–425. DOI: 10.1016/0378-4371(92)90283-V.

[109] J. Nielsen, J. Hetherington, and M. Stamatakis. *Zacros Software Package Development: Pushing the Frontiers of Kinetic Monte Carlo Simulation in Catalysis*. Tech. rep. 2014, pp. 1–11.

[110] M. J. Hoffmann, S. Matera, and K. Reuter. "kmos: A lattice kinetic Monte Carlo framework". In: (Jan. 2014). DOI: 10.1016/j.cpc.2014.04.003.

[111] A. Chatterjee and D. G. Vlachos. "An overview of spatial microscopic and accelerated kinetic Monte Carlo methods". In: *Journal of Computer-Aided Materials Design* 14.2 (Mar. 2007), pp. 253–308. DOI: 10.1007/s10820-006-9042-9.

[112] A. P. J. Jansen. *An Introduction to Kinetic Monte Carlo Simulations of Surface Reactions*. Lecture No. Vol. 856. Lecture Notes in Physics. Berlin, Heidelberg: Springer Berlin Heidelberg, 2012. DOI: 10.1007/978-3-642-29488-4.

[113] M. Stamatakis and D. G. Vlachos. "A graph-theoretical kinetic Monte Carlo framework for on-lattice chemical kinetics". In: *The Journal of Chemical Physics* 134.21 (June 2011), p. 214115. DOI: 10.1063/1.3596751.

[114] J. Nielsen, M. D'Avezac, J. Hetherington, and M. Stamatakis. "Parallel kinetic Monte Carlo simulation framework incorporating accurate models of adsorbate lateral interactions". In: *The Journal of Chemical Physics* 139.22 (Dec. 2013), p. 224706. DOI: 10.1063/1.4840395.

[115] M. T. Darby, E. C. H. Sykes, A. Michaelides, and M. Stamatakis. "Carbon Monoxide Poisoning Resistance and Structural Stability of Single Atom Alloys". In: *Topics in Catalysis* 61.5-6 (2018), pp. 428–438. DOI: 10.1007/s11244-017-0882-1.

[116] M. D. Marcinkowski, M. T. Darby, J. Liu, J. M. Wimble, F. R. Lucci, S. Lee, A. Michaelides, M. Flytzani-Stephanopoulos, M. Stamatakis, and E. C. H. Sykes. "Pt/Cu single-atom alloys as coke-resistant catalysts for efficient C-H activation". In: *Nature Chemistry* 10.3 (2018), pp. 325–332. DOI: 10.1038/NCHEM.2915.

[117] S. Piccinin and M. Stamatakis. "Steady-State CO Oxidation on Pd(111): First-Principles Kinetic Monte Carlo Simulations and Microkinetic Analysis". In: *Topics in Catalysis* 60.1-2 (Feb. 2017), pp. 141–151. DOI: 10.1007/s11244-016-0725-5.

[118] M. Stamatakis and S. Piccinin. "Rationalizing the Relation between Adlayer Structure and Observed Kinetics in Catalysis". In: *ACS Catalysis* 6.3 (2016), pp. 2105–2111. DOI: 10.1021/acscatal.5b02876.

[119] N. Nikbin, N. Austin, D. G. Vlachos, M. Stamatakis, and G. Mpourmpakis. "Catalysis at the sub-nanoscale: Complex CO oxidation chemistry on a few Au atoms". In: *Catalysis Science and Technology* 5.1 (2015), pp. 134–141. DOI: 10.1039/c4cy01295j.

[120] S. Piccinin and M. Stamatakis. "CO oxidation on Pd(111): A first-principles-based kinetic monte carlo study". In: *ACS Catalysis* 4.7 (2014), pp. 2143–2152. DOI: 10.1021/cs500377j.

[121] M. Apostolopoulou, R. Day, R. Hull, M. Stamatakis, and A. Striolo. "A kinetic Monte Carlo approach to study fluid transport in pore networks". In: *Journal of Chemical Physics* 147.13 (2017). DOI: 10.1063/1.4985885.

[122] P. L. J. Walker, F. J. Rusinko, and L. G. Austin. "Gas Reactions of Carbon". In: *Advances in Catalysis*. Vol. 11. 1959, pp. 133–221. DOI: 10.1016/S0360-0564(08)60418-6.

[123] M. Frenklach and A. Mebel. "On the mechanism of soot formation". In: *Physical Chemistry Chemical Physics* 6.35 (2020). DOI: 10.1039/D0CP00116C.

[124] E. V. Anslyn and D. A. Dougherty. *Modern Physical Organic Chemistry*. University Science, 2005.

[125] V. J. Murray, E. J. Smoll, and T. K. Minton. "Dynamics of Graphite Oxidation at High Temperature". In: *The Journal of Physical Chemistry C* 122.12 (Mar. 2018), pp. 6602–6617. DOI: 10.1021/acs.jpcc.7b11772.

[126] M. Núñez, T. Robie, and D. G. Vlachos. "Acceleration and sensitivity analysis of lattice kinetic Monte Carlo simulations using parallel processing and rate constant rescaling". In: *The Journal of Chemical Physics* 147.16 (Oct. 2017), p. 164103. DOI: 10.1063/1.4998926.

[127] T. Danielson, J. E. Sutton, C. Hin, and A. Savara. "SQERTSS: Dynamic rank based throttling of transition probabilities in kinetic Monte Carlo simulations". In: *Computer Physics Communications* 219.9 (Oct. 2017), pp. 149–163. DOI: 10.1016/j.cpc.2017.05.016.

[128] E. C. Dybeck, C. P. Plaisance, and M. Neurock. "Generalized Temporal Acceleration Scheme for Kinetic Monte Carlo Simulations of Surface Catalytic Processes by Scaling the Rates of Fast Reactions". In: *Journal of Chemical Theory and Computation* 13.4 (2017), pp. 1525–1538. DOI: 10.1021/acs.jctc.6b00859.

[129] A. Chatterjee and A. F. Voter. "Accurate acceleration of kinetic Monte Carlo simulations through the modification of rate constants". In: *Journal of Chemical Physics* 132.19 (2010). DOI: 10.1063/1.3409606.

[130] Open Source. *Cantera example program for the calculation of chemical equilibrium (Last accessed: 2020-11-08)*. URL: https://cantera.org/tutorials/cxx-guide/equil-example.html.

[131] S. Schmitt and J. Graña-Otero. "Kinetic Monte-Carlo Study of Pitting Dynamics in High-Temperature Graphene Gasification". In: *11th US National Combustion Meeting*. 2019.

[132] F. Oberhuber. "Untersuchung kristallographisch definierter Graphen-Ränder". PhD thesis. Universität Regensburg, 2015.

Simon Schmitt

Education

- **University of Kentucky**, Lexington, Kentucky, January 2017 - Current

  Ph.D. Mechanical Engineering

- **Karlsruhe Institute of Technology**, Karlsruhe, Germany, October 2012 - April 2016

  B.Sc. Mechanical Engineering

Professional Experience

- **Porsche AG**, Weissach, Germany, March 2016 - August 2016

  Development Engineering Intern

Awards

- Winner of the Three Minute Thesis (3MT) at the UK Mechanical Engineering Graduate Student Congress (MEGSS) in 2018 and 2019

Publications

Journal Articles

- Schmitt, S., and Graña-Otero, J., "Kinetic Carbon Oxidation Mechanism and Atomic-Scale Simulation of Graphene Etching", Carbon, In preparation.

Conference Articles

- Graña-Otero, J., Edward, S., Schmitt, S., and Mahmoudi, S., "Surface Ablation Regime of a Model of Porous Material", AIAA Aviation Forum, AIAA Paper 2019-3127, Dallas, TX, June 2019.

- Graña-Otero, J., Mahmoudi, S., Sullivan, E., and Schmitt, S., "Kinetics of Oxidation of Carbon Materials", AIAA Aviation Forum, AIAA Paper 2019-3128, Dallas, TX, June 2019.

- Schmitt, S., Mahmoudi, S., and Graña-Otero, J., "Molecular-Scale Carbon Oxidation at Hypersonic Speeds", AIAA Aviation Forum, AIAA Paper 2019-3129, Dallas, TX, June 2019.

- Graña-Otero, J., and Schmitt, S., "A Continuum Model for Graphene Oxidation", 11th US National Combustion Meeting, Pasadena, CA, March 2019.

- Schmitt, S., and Graña-Otero, J., "Kinetic Monte Carlo Study of Pitting Dynamics in High-Temperature Graphene Gasification", 11th US National Combustion Meeting, Pasadena, CA, March 2019.

Conference Abstracts

- Graña-Otero, J., Schmitt, S., and Kumar, A., "Computational modeling of graphene oxidation", Spring Meeting of the American Chemical Society, Orlando, FL, March 2019.